Resonance, damping and spin currents in metallized YIG thin films

DISSERTATION

SUBMITTED IN PARTIAL FULFILLMENT
OF THE REQUIREMENTS FOR THE DEGREE OF

DOCTOR OF PHILOSOPHY

IN PHYSICS

by

Eric Hermanny

BRAZILIAN CENTER FOR RESEARCH IN PHYSICS (CBPF)

October 2021

"RESONANCE, DAMPING AND SPIN CURRENTS IN METALLIZED YIG THIN FILMS"

ERIC HERMANNY

Tese de Doutorado em Física apresentada no Centro Brasileiro de Pesquisas Físicas do Ministério da Ciência Tecnologia e Inovação. Fazendo parte da banca examinadora os seguintes professores:

Rubem Luís Sommer – Presidente/Orientador/CBPF

Roberto Bechara Muniz - UFF

Angela Burlamaqui Klautau– UFPA

João Paulo Sinnecker – CBPF

Ivan dos Santos Oliveira Junior – CBPF

Rio de Janeiro, 01 de outubro de 2021.

Abstract

Since its discovery, yttrium iron garnet (YIG) has been object of great interest because of its peculiarly low magnetic damping. Magnetic materials with reduced damping promote microwave power efficiency, longer magnon lifetime and longer spin-wave propagation. Owing to research on charge-to-spin current conversion, the control of magnetic damping in ferromagnetic thin films has recently been achieved by applying charge current on adjacent metal layer with strong spin-orbit coupling (SOC). This work starts with an exposition, in perspective, on the development of fundamental concepts concerning magnetization dynamics, with a special interest in ferromagnetic resonance (FMR) in thin films. Concepts from the field of spintronics, including spin pumping and some effects involved in spin-to-charge current interconversion, are also approached. The conceptual framework is built from an experimental point of view, to provide the adequate understanding of the background from where our investigation of YIG/spacer/m-FM (metallic ferromagnet) structures emerges. The description of our pursuit of a safe fabrication route that provides spintronic-compatible YIG thin films grounds the experimental results that follow. The core achievement of this study is the announcement and discussion of major damping reduction in metallized YIG thin films (YIG/Ag/Ni) without the need of applied charge current. We suggest that the origin of this unexpected effect is a strengthening of the FMR uniform mode in the YIG layer, due to frequency- and phase-locking that result from self-synchronization mediated by nonzero spin densities transiting the metallic layers.

Keywords

Ferromagnetic resonance; nanomaterials; YIG; thin films; spin pumping

Resumo

Desde o seu descobrimento, a granada de ítrio e ferro (YIG) tem sido objeto de grande interesse por ter um coeficiente extremamente reduzido de amortecimento magnético. Materiais magnéticos com baixo coeficiente de amortecimento permitem maior eficiência elétrica, maior persistência no tempo para mágnons e maior comprimento de propagação para ondas de spin. Graças à investigação sobre a conversão de correntes de carga em corrente de spin, recentemente conseguiu-se controlar o coeficiente de amortecimento em filmes finos magnéticos aplicando-se potencial elétrico a uma camada adjacente de metal com forte acoplamento spin-órbita (SOC). Este trabalho começa com uma exposição, em perspectiva, sobre o desenvolvimento de conceitos fundamentais envolvendo dinâmica da magnetização, com um interesse especial em ressonância ferromagnética (FMR) de filmes finos. Alguns conceitos do campo da spintrônica, incluindo bombeamento de spin e alguns efeitos relacionados à conversão entre correntes de carga e de spin, também são abordados. O esquema conceitual é construído desde um ponto de vista experimental, para prover a compreensão adequada do contexto de onde surge a nossa investigação sobre as estruturas YIG/espaçador/m-FM (onde m-FM é uma abreviação para "metal ferromagnético"). A descrição da nossa busca por estabelecer uma rota segura de fabricação que produza filmes finos de YIG apropriados para experimentos e dispositivos spintrônicos lastreia os conseguintes resultados experimentais. A conquista central deste estudo é a descoberta e discussão de uma importante redução do coeficiente de amortecimento de filmes finos de YIG através da adição de camadas de prata (Ag) e níquel (Ni), sem a necessidade de aplicar corrente. Sugerimos que a origem desse efeito inesperado é o fortalecimento do modo uniforme da FMR no filme de YIG, devido aos travamentos de frequência e de fase que resultam da auto-sincronização mediada por densidades não nulas de spins transitando as camadas.

Palavras chave

Ressonância ferromagnética; nanomateriais; YIG; filmes finos; bombeamento de spins

Acknowledgements

I would like to express sincere gratitude to my supervisor, Prof. Rubem Luis Sommer, for trusting me the mission of investigating applications of YIG in spintronics, and for giving me the freedom to choose the emphasis of the project, and support in the course of its development.

Most of the experimental activities involved in this study were performed at the Laboratory of Applied Magnetism, in CBPF. The author of this Dissertation does not claim the merit of assembling any of the experimental setups, having only eventually collaborated in some adjustments. Nor do we claim the authorship of any of the codes used in the instrumentation. Instead, we gratefully acknowledge the helpful collaboration of Diego E. González-Chávez. We also thank the director of the Laboratory, Prof. Rubem Luis Sommer, and all the students, researchers and technicians who have contributed to its scientific instrumentation.

For their help at the Cryogenics Facilities, we especially thank Prof. Magda Bittencourt and Crystal. We would also like to thank Mariana and Paulinha from the Advanced Materials Sample Preparation Laboratory; Hamza, Evelyn and Raquel from the Laboratory of Crystallography and X-Ray Characterization; Ricardo, Elvis and Prof. Alexandre Mello from the Laboratory of Surfaces; and Patricia Coimbra from the Technological Innovation Center of Rio de Janeiro (NITRio). Special thanks to Prof. Joe Gomes for assisting with the AFM characterization of our YIG samples, and to Bruno Gomes da Silva for training me in the operation of the sputtering systems and helping me out with data-processing codes. We extend our gratitude to our work group and everyone in CBPF, or elsewhere, who have supported this project.

In the memory of my father,

and to all researchers who bear
sincere respect for the progress of science.

Contents

Le hasard ne favorise que les esprits préparés.

Louis Pasteur

Introduction

The turn of this century witnessed the emergence of spin-orbitronics. Along with theoretical predictions, the development of new materials to achieve breakthroughs in experimental results has been of utmost importance. Much effort is dedicated today in understanding and controlling the effective magnetic damping in spintronic devices. Magnon-mediated transmission of signals is challenged by spin relaxation, which renders spin-wave propagation extremely short ranged. Ytrium iron garnet (YIG) is known to be the magnetic material that exhibits by far the lowest magnetic damping. While mastering techniques for the fabrication of YIG thin films is essential to obtain a damping coefficient in the order of 10^{-4}, electric current-driven spin injection from a neighboring nonmagnetic metal (NM) was proven to be efficient in artificially reducing the damping in magnetic layers [1] [2] [3] [4]. However, the threshold current for full compensation is hardly achievable. This limitation has hindered the accomplishment of coherent ferromagnetic-resonance microwave emission, on the path to the predicted realization of the so-called (spin-wave amplification by stimulated emission of radiation) SWASER devices [5] [6] [7] [8].

The finding that is the object of this Dissertation originated in our research on spin-to-charge current conversion in ferromagnetic metals, where a YIG thin film is driven to FMR in order to inject spins through a nonmagnetic spacer and into an adjacent ferromagnetic metallic layer. When checking the presence of spin-pumping, we came across an unexpected result for the damping enhancement of one of the samples, *i.e.*, YIG1Ag(10)Ni(20), which exhibited, not an enhancement of the damping, but a sharp reduction, instead. We thereafter confirmed the finding by reproducibility. Therefore, the motivation of the research shifted from the interest in studying the anomalous Hall effect from a spintronic perspective to the study of the origin and implications of the unexpected behavior, the observation of which is unprecedented for magnetic thin films.

In metal-coated YIG thin films at ferromagnetic resonance (FMR), spin pumping is expected to occur, which can be experimentally evidenced by damping enhancement [9], while spin-orbit coupling-originated spin-to-charge current conversion is evidenced by the detection of voltage in the metallic coating [10] [11] [12]. These procedures are well established and widely recognized. The reciprocal effect of spin pumping is the spin-transfer torque (STT), responsible for the effective-damping reduction that can be achieved when an in-plane charge current is applied on the neighboring metal layer. As the observed damping reduction took place without

the application of any charge current on the metal-coated sample, it constitutes an anomalous behavior. At first glance, it seemed to defy the principle of energy conservation within the magnetic system of the sample, so a physical viability for the phenomenon was investigated. To that end, any evidence that could be collected from the experiments was first analyzed, and then contrasted with phenomena reported in the literature on spintronics.

Literature shows that spin currents may have a strong influence in the coupling of resonating ferromagnetic multilayers [13] [14] [15] [16], and in the distribution of spin-wave resonance modes [17] [18]. We have reasons to believe that the observed damping reduction can be explained by this influence. Experimental data produced in this work showed a strengthening of the FMR uniform mode in the capped YIG layer, as compared to the bare YIG sample. This Dissertation attributes this strengthening to a self-synchronization of the magnetization precession in the YIG, due to a dynamic coupling mediated by spin currents transiting the metallic coating. As a result of this strengthening, the magnetic relaxation due to the coupling of the FMR uniform-mode magnons with lattice-vibration phonons is inhibited. In turn, compared data from electrical detection of spin currents in different samples indicated a backflow of spin current at Ag/Ni interfaces, which is attributed to a restricting spin conductance through this interface. The result of this backflow is an injection of magnetic moment back into the YIG layer, which compensates the outflow due to spin pumping. Together, these aspects of the magnetic system's dynamics explain the anomalous effective-damping reduction.

Although the physical background delineated by the analysis of the phenomenon must be still completed by further investigation, it already points to the direction of coherent oscillations. If on the one hand, this work presents YIG/Ag/Ni as a new material, with accomplished new magnetic features, on the other hand, because this structure supports self-synchronization of ferromagnetic resonance oscillations, it is a good stage for further experimentation that may lead to the coherent microwave emission driven by in-plane charge current, and to SWASER devices.

As an introduction to spintronic basic concepts, phenomenology and figures of merit, Chapter 1 (**Theoretical considerations**) of this Dissertation describes the interplay between spin-diffusion length, spin Hall angle, interfacial spin-mixing conductance and layer thicknesses. These, and eventually the presence of magnetic ordering in the metallic layer(s) neighboring the YIG layer, will determine the spin-current steady-state regime at ferromagnetic resonance. Spin-to-charge current conversion effects that can be present in the structures studied (*i.e.*, inverse spin Hall, anomalous spin Hall and inverse Rashba-Edelstein effects) are also described.

Chapter 2 describes the **Experimental methods** utilized along this Project. The establishment of a route for YIG thin-film fabrication with optimized magnetic properties has been a preliminary objective of this Project. The optimization of the magnetic character of YIG

is closely related to its crystal quality, which should extend to the film surface to maximize interfacial spin conductance into adjacent metal layers. The pursuit of this route is detailed in Section 3.1 (**Fabrication of YIG thin films**).

The reasoning that supports the proposed physical background of the observed anomalous behavior, which is the main object of this work, is unfolded in Section 3.2 (**Magnetic characterization of YIG/spacer/m-FM structures**), further grounding the reiterated verification of effective-damping reduction in YIG/Ag/Ni structures, without applied electric potential.

1. Theoretical Considerations

1.1 Magnetic resonance and ferromagnetic materials

1.1.1 Overview

Driving materials into magnetic resonance is an ingenious way to reveal hidden properties lying deeply within their entangled microscopic features and atomic structures. Nuclear magnetic resonance (NMR) targets atomic nuclei with nonzero total spin in all kinds of materials. The magnetic moments of these nuclei are small compared to the magnetic moment of an electron, due to their difference in mass. Thus, nuclear magnetic moments resonate at relatively low frequencies. Electron paramagnetic resonance (EPR) aims at unpaired localized electrons in paramagnetic materials. Ferromagnetic resonance (FMR), in turn, concerns the macroscopic structures called magnetic domains, or Weiss domains, of a ferromagnetic material. The features of resonance phenomena in ferromagnets are largely determined by the fact that in these substances we are dealing, not with weakly interacting magnetic moments of nuclei, or of ions and free radicals in paramagnetic bodies, but with a complex system of strongly interacting electrons. EPR and FMR operate in the microwave frequency range. FMR can be used not only for ferromagnetic materials but also for ferrimagnetic materials. [19] [20] [21]

Resonance occurs when a system of magnetic moments aligning under the influence of a uniform magnetic field is also submitted to a transverse field oscillating at Larmor frequency thus inducing the moments to sustained precession (Figure 1). From the quantum-physical viewpoint, the magnetic moments are Zeeman split by the uniform field, and the system resonates when it absorbs energy from the transverse oscillating field because its frequency matches the quantum leap between the energy levels. As the system is powered up, energy is transferred to the lattice through different relaxation channels and dissipated in the form of heat. The classical approach is helpful to study the behavior of magnetic moments in FMR, because the exchange-coupled electron spins that together are represented by the magnetization of each Weiss domain in the ferromagnet can be treated as one only magnetic moment, the so-called macrospin. This magnetic moment, whose intensity depends on the domain volume, is usually at least three orders of magnitude greater than the magnetic moment of an electron. The relation between magnetic moment, Larmor frequency and magnetizing field will be addressed in Sections 1.3 and 1.7 [19] [20].

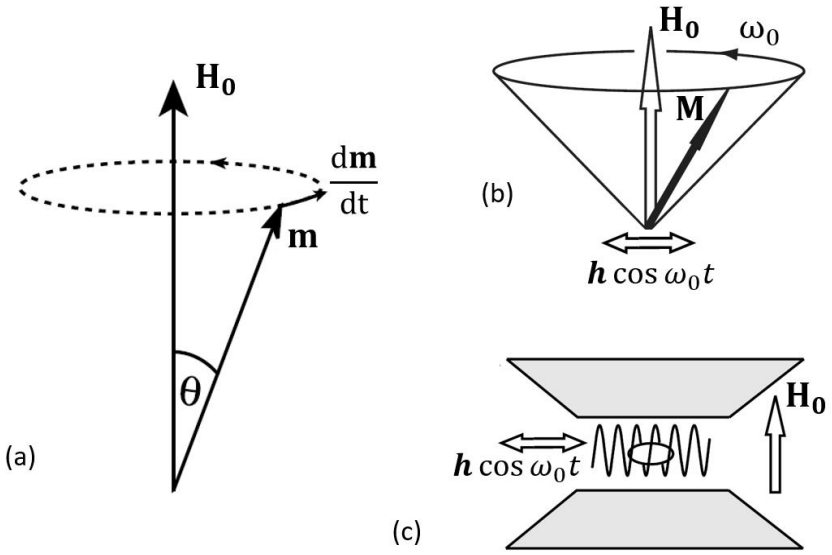

Figure 1. (a) ***Larmor precession****: When immersed in a constant magnetic field ($\vec{H}_0$), a magnetic moment ($\vec{m}$) will precess about the field's direction at Larmor frequency ω_0. The Greek letter θ indicates the precession angle. (b) and (c)* ***Resonance****: For sustained precession in condensed matter, besides the uniform magnetic field, a transverse field ($\vec{h}\cos\omega_0 t$) oscillating at Larmor frequency must also be applied. Diagrams were adapted from Ref. [20].*

Novel knowledge concerning the dynamics of magnetic systems has been obtained experimentally, by using ultrafast optical methods. The addition of microscopic spatial resolution enables new features, like the imaging of spatially nonuniform dynamics. Optical techniques enable not only improved time and spatial resolution but also vector measurements of the magnetization, which are essential to perform FMR-relaxation or torque-transfer studies [22]. Those techniques are not in the scope of this Dissertation, but some of them are worth mention [23], like magneto-optic Kerr effect magnetometry (MOKE) adapted to FMR measurements [22] [24]; Brillouin light scattering spectroscopy (BLS), which analyzes the frequency shifts of visible light scattered from spin waves [25]; x-ray detected magnetic resonance (XDMR), which uses x-ray magnetic circular dichroism to probe the resonant precession of local magnetization components in a strong microwave pump field [26]. Magnetic resonance force microscopy (MRFM), in turn, modulates the sample magnetization with standard FMR methods to generate a force signal that can detect localized atomic magnetic moments [27].

1.1.2 Ferromagnetic resonance

After their theoretical prediction in 1935 by L. D. Landau and E. M. Lifshitz, the clear observation of ferromagnetic resonance peaks was reported for the first time in 1946, independently, by J. H. E. Griffiths in Great Britain, and by E. K. Zavoiskii in the USSR [21] [28]. Griffith observed the peaks when he was trying to measure the effective magnetic

permeability of ferromagnetic metals at high frequencies. In his accidental and groundbreaking observation, resonance was driven by high-frequency electrical current across a ferromagnetic metal wire, in the presence of a dc external magnetic field [29]. Subsequently, FMR techniques were developed in which the magnetization of ferromagnetic (FM) materials was inductively excited into resonance by subjecting it to high-frequency magnetic field. Today FMR is one of the standard tools to examine the magnetization dynamics of ferromagnetic materials excited out of the thermodynamic *equilibrium* [30].

In the traditional FMR experiment, the sample is placed in a resonant cavity of a determined frequency, at the end of a waveguide. The waveguide delivers an oscillating magnetic field at the frequency of the cavity and the cavity resonates it into the sample. When the driving force is constant, the rates of change of the dynamical system will increase or decrease until the driving and relaxation forces are equal and a steady-state condition is attained [31]. The microwave power absorbed by the sample is detected while a transverse dc field from an electromagnet is applied with a gradual variation of strength, and if the *spectrum* thus produced shows a peak, a resonance field is determined (Figure 2). The resonance field is the condition for ferromagnetic resonance in that sample, at the frequency of the cavity. The downside of this technique is that it is limited to the characteristic frequencies of the cavity [23].

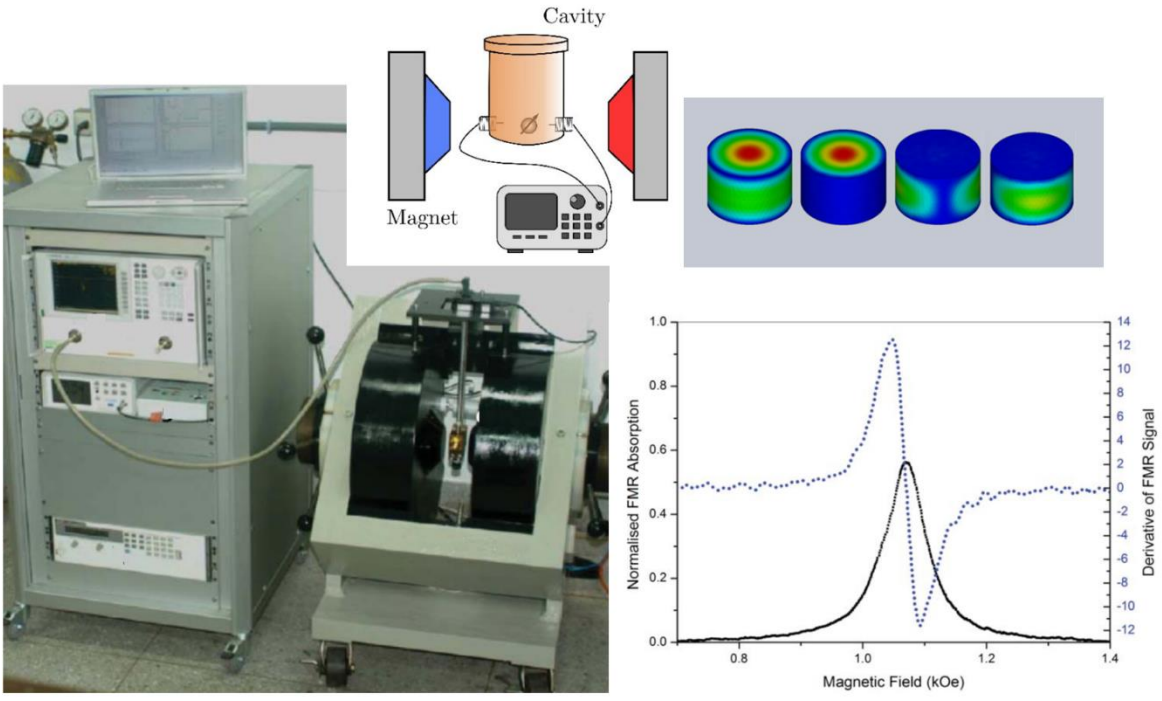

Figure 2: Example of a FMR setup, using a cylindrical microwave resonant cavity. In the picture on the left, a computer, a gaussmeter, and a spectrometer combined with rf generator. The sample is inside the cavity, placed in the center of an electromagnet. On the top, a simplified diagram of the setup. On the upper right corner, modes of the cylindrical cavity; and below, absorption (in black) and derivative (in blue) resonance lines at 9,8 GHz, for a 5nm thin-film sample of permalloy. (Adapted from Refs. [32] and [33])

This limitation has been overcome by the advent of broadband FMR techniques, like the vector network analyzer ferromagnetic resonance (VNA-FMR) and the pulsed inductive microwave magnetometer (PIMM). Both techniques use inductive excitation of the sample. For induction to occur, the sample must be placed in close proximity to a waveguide, so that the ferromagnetic material to be analyzed is reached by the oscillating magnetic field generated by the waveguide. In the VNA-FMR technique, the vector network analyzer generates a radio-frequency signal and simultaneously detects the power absorbed by the sample. The equipment enables frequency sweeps as well as field sweeps. In Section 2.1, more detailed attention is dedicated to VNA-FMR, as it is the main technique used in this work for sample characterization. The PIMM technique uses extremely short pulses (picosecond order) and large voltage amplitudes. The response is measured by an ultrahigh-resolution oscilloscope able to register the voltage generated by the magnetization of the sample after excitation, between pulses [23].

It must be noted that metallic materials only absorb microwave fields to the extent of their skin depth. Hence, thin films or fine powder samples must be used for field-induced FMR experiments. When the material is an insulator, such as ferrimagnetic oxides, skin depth is, of course, not a concern [20].

Special conditions (as detailed in Section 1.3), must be satisfied so that ferromagnetic resonance manifests as a uniform mode, where all the moments precess together, in phase, and with the same amplitude, and where the whole system behaves like a macrospin. This regime can be disturbed, for example, if the rf power is increased to the limit where the ferromagnetic resonance excitation breaks down into nonuniform modes, generating spin waves and magnons [34], or if the strength of the magnetizing field is decreased below saturation, causing the magnetization of the ferromagnet to break into magnetic domains [28] [31].

The FMR effect is also observed in magnetoimpedance measurements. In this case, an ac electric current must pass through the sample immersed in a dc magnetic field. When the frequency of the ac current matches the ferromagnetic resonance condition, its impedance exhibits important variation [23].

Theoretical considerations in this Dissertation assume that we are studying ferromagnetic materials below their Curie temperature (or Néel temperature, if the material is ferrimagnetic). Near the Curie point, results would be compromised because the material exhibits a combination of paramagnetic and ferromagnetic behaviors.

1.2 The damping of the magnetization precession

The mechanisms by which damping occurs include the coupling of the magnetization field to spin waves, eddy currents, lattice vibrations, strains on the crystal structure, and crystal defects such as voids, interstitial atoms and foreign atoms. When the external magnetic field is not strong enough to eliminate all domain walls, the domain structure may play a dominant role in the damping, and the local rate of relaxation may vary by large amounts from point to point within the ferromagnet [31].

At the turn of the century, two-magnon scattering and spin-pumping became object of much debate, given their relevance as spin damping mechanisms in thin-film structures. Two-magnon relaxation is originated in defects, mostly on surfaces and interfaces of a ferromagnetic layer. It differs from other relaxation channels recurrent in thin films in that its contribution to resonance linewidths has a nonlinear behavior in frequency. Spin pumping occurs when there is a transfer of angular momentum from the precessing magnetization to the conduction electrons of an adjacent metallic film. Angular momentum is thus transported out of the resonating ferromagnetic layer, across the interface and into the adjacent metallic layer. In this process, energy is taken from the ferromagnet's magnetization dynamics, and spins accumulate in the normal metal, near the interface. The magnetization acts as a "spin pump", and that is why the mechanism has been given its name [35]. The spins pumped into the metallic layer will eventually dissipate, and the phenomenology of their passage is object of Section 1.5.3.

Damping mechanisms are classified according either to their origin or to the immediate destination of the energy conducted by the mechanism. The damping mechanisms that originate in intrinsic properties of a FM material are referred to as **intrinsic**. It should be noted that in nanoscale structures, intrinsic mechanisms may manifest differently, as compared to the bulk material. Damping mechanisms originated in defects are called **extrinsic.** As defects tend to be more abundant in surfaces and interfaces than in the bulk material, extrinsic mechanisms tend to become more important in nanoscale structures. Spin pumping also contributes to damping and is classified as extrinsic. (More on spin pumping in Section 1.5.) Extrinsic damping can be controlled in material and device fabrication [36].

As for the second *criterium*, damping mechanisms are also classified as **direct**, when energy through the relaxation channel flows directly to the lattice (or to conduction electrons), and as **indirect**, when the relaxation occurs via excitation of many magnetic modes. In other words, there are two pathways for the degradation of the uniform mode; the energy can flow directly from the uniform mode into the lattice motions and electrons, or it can flow from that mode into higher order magnetic modes before it is absorbed by the lattice [37]. Figure 3 shows a scheme for these pathways.

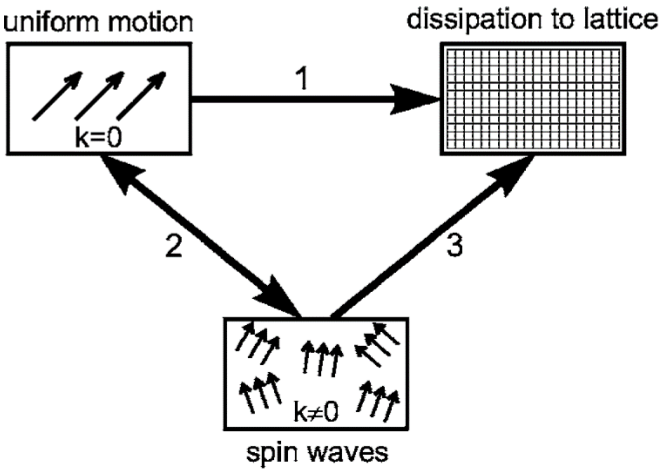

Figure 3: Paths for the degradation of uniform mode. Two paths of energy dissipation to the lattice are schematized in the diagram. Path 1 represents direct relaxation to the lattice, while indirect relaxation is characterized by two steps: decay into nonuniform modes (path 2), and dissipation to the lattice (path 3). From Ref. [30]

Direct channels are also referred to as Gilbert-type mechanisms because their contribution to the FMR linewidth increases linearly with resonance frequency [38]. This relation stems from the fact that a linear linewidth contribution makes the relaxation channel compatible with the damping described by the Landau-Lifshitz-Gilbert equation (object of Section 1.3). Table 1 shows the classification of damping channels, according to both these *criteria*.

Damping mechanism	Classification	
Eddy currents	intrinsic	direct
Magnon-phonon scattering	intrinsic	direct
Electron-magnon scattering	intrinsic	direct
3- and 4-magnon scattering	intrinsic	indirect
Two-magnon scattering	extrinsic	indirect
Spin-pumping	extrinsic	direct*

Table 1: Examples of magnetization damping channels and their respective classification.
**Spin pumping appears as a direct mechanism because it is a Gilbert-type mechanism.*

Regarding the scope of this Dissertation, eddy currents and electron-magnon scattering are not concerned, because YIG is a ferromagnetic insulator. And considering the thickness of the YIG films used, as will be made clear, our resonance experiments have been performed under the ordinary small-angle FMR regime, which rules out nonlinear phenomena associated with the dynamics of large-angle magnetization rotations, like three- and four-magnon scattering [39]. Nevertheless, special care must be taken to correctly evaluate the possibility that two-magnon

relaxation is playing any relevant role in the damping, because this would mean that nonlinear effects should be included in the model. Section 1.4 shows how to objectively perform that evaluation.

1.3 The equation of motion for the magnetization of a ferromagnet

1.3.1 A phenomenological approach

When it comes to theoretically describing the magnetization dynamics of ferromagnetic structures, virtually any piece of literature on the subject displays either of two combinations of letters to start with, namely LL and LLG. They designate two closely related phenomenological equations, which aspire to describe the system in macroscopic language, in terms of the magnetization per unit volume $\vec{M}(\vec{r},\vec{t})$ [40]. This Section (1.3) is intended to bring forward some of what lies behind the LL and LLG abbreviations.

There was one event in the history of Solid-State Physics whereby the understanding by the scientific community about the evolution in time of the magnetization in a ferromagnetic material spiraled. This was the publication, in 1935, of the article "On the theory of dispersion of magnetic permeability in ferromagnetic bodies", authored by Lev Davidovich Landau and his student Evgeny Mikhailovich Lifshitz. Landau was at that time 27 years old and the head of the Department of Theoretical Physics at the Kharkiv Institute of Physics and Technology, Ukraine, in the former Soviet Union. The article appeared in a time of great advances in the study of magnetism and presented an abundance of results that amounted to a new approach to the physics of ordered spin systems. It was a phenomenological approach, based on an equation that has come to be known as the Landau-Lifshitz equation. Their great insight was to introduce the concept of an effective magnetic field $\vec{H}_{eff}$, which depends on the state of all the spins and thus includes all kinds of different interactions that locally affect the magnetization throughout the material [41].

In the idealized case of an isolated sphere made of a perfect, isotropic ferromagnetic material submitted to an external uniform magnetic field $\vec{H}_0$ strong enough to saturate its magnetization, the problem of ferromagnetic resonance is trivial and a good starting point. In this case, the domain structure totally disappears and the magnetization vector in any part of the sphere, as well as the total magnetization vector $\vec{M}$, is parallel to the external field. The system can be compared to a magnetic top, $\vec{M}$ is interpreted as macrospin, and the problem can be looked upon as purely classical. The magnetic and mechanical moments are connected by the classical equation of motion:

$$\frac{\partial \vec{\boldsymbol{M}}}{\partial t} = -\gamma\left(\vec{\boldsymbol{M}} \times \vec{\boldsymbol{H}}\right), \tag{1}$$

where γ is the gyromagnetic ratio and $\vec{\boldsymbol{H}} = \vec{\boldsymbol{H}}_{\boldsymbol{0}} + \vec{\boldsymbol{H}}_{\sim}$ is the combination of the uniform field with the high-frequency transversal field. Resonance occurs when the frequency ω of this oscillating field coincides with the so-called Larmor frequency:

$$\omega_0 = \gamma H_0 \,. \tag{2}$$

Near this frequency, the system is excited: the magnetization precession is enhanced, and the magnetic susceptibility undergoes a sharp variation. Approximations can be made for the usual case in which $H_{\sim} \ll H_0$ and the dynamic susceptibility will be:

$$\chi = \frac{\chi_0}{1 - \left({}^{\omega}/_{\omega_0}\right)}\,, \tag{3}$$

where χ_0 is the susceptibility in the constant field $\vec{\boldsymbol{H}}_{\boldsymbol{0}}$. It should be noted that this model corresponds to an undamped driven harmonic oscillator and there is divergence when the resonance condition is met, at $\omega = \omega_0$. The absence of attenuation means that Equation 1 does not consider dissipative processes [21] [28].

In their article, L. D. Landau and E. M. Lifshitz introduced the idea that the various interactions in a real ferromagnet can be taken into consideration phenomenologically by assuming that the spins involved in the ferromagnetic ordering precess at a frequency ω_{res}, not in the external field $\vec{\boldsymbol{H}}_{\boldsymbol{0}}$, but in some **internal effective field**. On one hand, the action of this effective field $\vec{\boldsymbol{H}}_{\boldsymbol{eff}}\left(\vec{\boldsymbol{r}}, \vec{\boldsymbol{t}}\right)$ on the magnetization $\vec{\boldsymbol{M}}\left(\vec{\boldsymbol{r}}, \vec{\boldsymbol{t}}\right)$ of the ferromagnet is just like the action of the external magnetic field $\vec{\boldsymbol{H}}_{\boldsymbol{0}}$ on an isolated spin, and the difference between them causes the resonance frequency

$$\omega_{res} = \gamma H_{eff} \tag{4}$$

to shift relative to the frequency ω_0 of the Larmor precession. On the other hand, the effective field, which depends on the state of all the spins, naturally includes collective effects in this system (*e.g.*, crystalline and shape anisotropies, magnetostriction and demagnetization) in circumstances where the magnetization being excited is spatially nonuniform. This treatment makes it possible to rewrite Equation 1 in the form:

$$\frac{\partial \vec{M}}{\partial t} = -\gamma\left(\vec{M} \times \vec{H}_{eff}\right), \tag{5}$$

where $\vec{H}_{eff}$ includes not only external fields, like the ones required for FMR ($\vec{H}_0$ and $\vec{H}_{\sim}$), but also any internal interaction in the ferromagnetic sample that can be considered as a modification of the magnetic field. Equation 5 gives a good approximation of the resonance frequencies of the magnetization $\vec{M}(\vec{r}, \vec{t})$ in real samples of ferromagnetic materials with low damping [35] [41] [28].

The strongly interacting electrons of the ferromagnetic material are bound to each other by the so-called exchange interaction, which produces a large resultant magnetization and a large internal magnetic field at the same time. When the magnitude or orientation of the ferromagnet's magnetization is not uniform throughout the crystal, situations arise which may dramatically change the effective field. Magneto-crystalline anisotropy, for example, is intrinsic to the material, originating mainly in spin-orbit interaction connected to the symmetry of crystal lattice (also in dipolar interactions), and it causes the effective field to be dependent on the directions of the crystallographic axes and of surfaces bounding the ferromagnetic material. Through magnetostriction, eventual elastic stress on the material can affect the orientation of spontaneous magnetization in ferromagnetic crystals and, therefore, also the effective field. Another factor is known as shape anisotropy. Because the magnetization is large, the demagnetization field is large, and the shape of the sample can therefore anisotropically affect the effective field. Only in special cases, when the ferromagnetic material is bounded by second-degree surfaces (an ellipsoid, a sphere, an infinite circular cylinder *etc*.), may the demagnetizing field be uniform. Also worth of mention is the skin effect. For radiation in the frequency range of a few GHz, for example, the depth of field penetration in metals is only between 0.1 and 1 micron. Internal fields of metallic ferromagnets with linear dimensions greater than their skin depth may be impacted by skin effect [21] [34].

The relevance of each contribution to the effective field $\vec{H}_{eff}$ will depend on the properties of the materials, the characteristics of the sample and the experimental conditions. Contributions originated in magneto-crystalline anisotropy are most significant in the study of single-crystal ferromagnets, but in many cases the effective field of the anisotropy is small compared with the external magnetizing field. Internal elastic stresses that may remain from the manufacture or those created by experimental conditions usually have comparatively little effect on resonance conditions, but can be noticeable in thin disk-shaped samples, wires and films. Demagnetizing fields, in turn, have approximately the same order of magnitude in a ferromagnet as the external magnetizing field [28].

1.3.2 The damping term

One of the most important problems in the macroscopic theory of ferromagnetic resonance is finding an equation of motion for the magnetization which will lead to the correct shape of the resonance absorption line. In the absence of the transverse oscillating field $\vec{\boldsymbol{H}}_{\sim}$, Eq. 1 describes the undamped free precession of an idealized macrospin in the external field $\vec{\boldsymbol{H}}_{\boldsymbol{0}}$, and in its presence, as remarked above, the dynamic susceptibility goes to infinity at resonance condition [28]. Equation 5 approaches the description of real ferromagnetic samples by introducing the concept of the effective field $\vec{\boldsymbol{H}}_{\boldsymbol{eff}}$, but the processes that relax the precession of the magnetization are still not included, and all real systems have some finite damping [30].

Details of the mechanism for the each kind of relaxation process must be approached from a quantum mechanical point of view and are thus too complex to be considered explicitly in a general equation of the motion of the magnetization. Instead, a phenomenological term can be introduced that contains damping parameters that correspond to the rate of energy transfer and can be determined experimentally [31]. Many versions of the damping term have been proposed to describe the loss of energy of a ferromagnetic system and the question is still open today. The first proposal was authored by Landau and Lifshitz themselves, in the same 1935 article in which they introduced the concept of effective field. Their improved equation of motion has the form [28]:

$$\frac{\partial \vec{\boldsymbol{M}}}{\partial t} = -\gamma\left(\vec{\boldsymbol{M}} \times \vec{\boldsymbol{H}}_{\boldsymbol{eff}}\right) - \gamma \frac{\alpha_{LL}}{M_s}\left[\vec{\boldsymbol{M}} \times \left(\vec{\boldsymbol{M}} \times \vec{\boldsymbol{H}}_{eff}\right)\right], \tag{6}$$

where M_s is the saturation magnetization and the dimensionless parameter α_{LL} expresses the amount of damping and is a characteristic of the sample. The damping term is the second term on the right-hand side of the equation. It describes the relaxation of the magnetization $\vec{\boldsymbol{M}}$. Neither of the two terms cause any change in the length of the magnetization. Their effect is illustrated in Figure 4, where they are each represented by a torque on the magnetization. The torque along the direction of precession represents the first term. It reinforces the precession. The torque that is orthogonal to both the direction of precession and the effective field represents the second term. It strives to return the magnetization to its *equilibrium* direction, the direction of $\vec{\boldsymbol{H}}_{\boldsymbol{eff}}$. After the magnetized ferromagnetic system is driven away of *equilibrium*, the magnetization vector moves along a spiral and gradually approaches the *equilibrium* position [28].

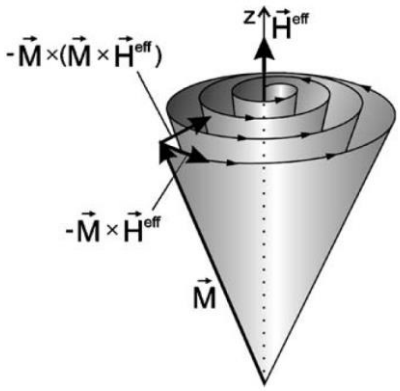

Figure 4: Relaxation of the precession of $\vec{M}$ according to the LL Equation (6). The minus sign means that the magnetic moment and angular momentum of the magnetization have opposite directions, like those of the electron. From Ref. [30]

In the FMR configuration, one important consequence of including the damping term on the equation of motion is that the dynamic susceptibility does not diverge anymore. It becomes a complex quantity, and its imaginary part characterizes the rf power absorbed by the magnetic system. There is also a shift in the resonance frequency. The shape and width of the resonance lines become intricately related to the damping term [21]. Equations 5 and 6 are both referred to as Landau-Lifshitz equation, or "LL equation" in literature.

In the 1955 Magnetism and Magnetic Materials Conference proceedings, T. L. Gilbert argued that the LL damping (α_{LL}) fails for large enough damping and proposed an expression that, in the small-angle regime, may be written as follows [31] [42]:

$$\frac{\partial \vec{\boldsymbol{M}}}{\partial t} = -\gamma\left(\vec{\boldsymbol{M}} \times \vec{\boldsymbol{H}}_{\boldsymbol{eff}}\right) + \frac{\alpha_G}{M_s}\left(\vec{\boldsymbol{M}} \times \frac{\partial \vec{\boldsymbol{M}}}{\partial t}\right), \tag{7}$$

where α_G is the dimensionless damping parameter of the Gilbert term. Equation 7 became known as the Landau-Lifshitz-Gilbert equation, or "LLG equation". In contrast to Eq. 6, the relaxation term in the LLG equation is proportional to the rate of change of the magnetization in time. In the ordinary case when $H_{\sim}$ is much weaker than H_0 , and for small damping parameters, the LL and LLG equations can be mathematically proved to be equivalent, and the shape of the absorption line in both cases, to be Lorentzian [28] [43] (which is also true for the classical damped, driven harmonic oscillator [30]).

A strong prediction follows from the LLG equation when it is applied to a FM film with in-plane anisotropy immersed in an in-plane uniform magnetic field, or with perpendicular anisotropy and perpendicular uniform magnetic field: The time-derivative Gilbert term produces a FMR linewidth that scales **linearly** with frequency [40] [42]. As described in Section 1.7, this linear behavior allows the Gilbert damping parameter α_G to be determined from FMR measurements [43]. All direct relaxation channels involved in the magnetization dynamics of the

sample contribute to the damping parameter α_G. When non-linear relaxation mechanisms are involved, extended models must be elaborated.

Bearing in mind that the effective magnetic field $\vec{\boldsymbol{H}}_{\boldsymbol{eff}}$ is a functional derivative of the magnetic energy ($\vec{\boldsymbol{H}}_{\boldsymbol{eff}}(\vec{\boldsymbol{r}}) = -\partial E/\partial \vec{\boldsymbol{M}}(\vec{\boldsymbol{r}})$), we can say that the second LL equation (6) and the LLG equation (7) are nonlinear integro-differential equations. In a few cases, an analytical solution can be encountered for them. Nowadays, powerful micromagnetic simulation codes based on the LLG equation have become a standard tool for studying the magnetization dynamics of complex magnetization distributions [43].

FMR measurements are usually carried out using small precession angles [44]. Because of the strong exchange interaction between spins in a FM material, it is usually not possible, as it is with nuclear spin systems (in NMR), to drive a ferromagnetic spin system so hard that the magnetization is pulled away from the effective field into right angles or reversed. If the power of the rf field is increased, instead of having the magnetization vector rotate away from its initial direction, the ferromagnetic resonance excitation breaks down into spin waves [34]. In extremely reduced-dimension structures like ultrathin films, this limitation can be overcome. Magnetization reversal of Weiss domains can be used, for example, in magnetic memory devices. This is one of the reasons why the interest has recently increased in understanding the magnetization dynamics in magnetic nanostructures under conditions where the deviations from equilibrium are large in amplitude. But it has not been yet possible to elaborate an applicable extension of linear-response theory into the large-amplitude regime [40].

In the experimental work for this Dissertation, metallized YIG thin films are driven into ferromagnetic resonance with an in-plane magnetizing field. YIG thin films are known to exhibit low damping and to exhibit easy in-plane magnetization. The thickness of these films is never less than 40 nm. These features indicate that the use of the linear-response approximation for the LLG equation of motion (Equation 7) should be appropriate. This remark will be especially relevant in the study of the frequency dependence of the FMR linewidth (Section 1.7).

At this point, another important remark concerns the oscillation modes of the magnetic system. When resonance condition is considered for the macrospin model, it is understood that the oscillation mode is uniform. The uniform mode of magnetic oscillations can be interpreted as a spin wave with zero wave vector, *i.e.*, with infinite wavelength, and in this case the resonance frequency is given by Equation 4. In real FMR experiments, as already mentioned, special conditions must be met to excite the sample in the uniform mode. The wavelength of the rf field must be large compared with the linear dimensions of the sample, or it would excite precession inhomogeneously throughout the extension of the ferromagnetic material. Although resonance in ferromagnetic materials is generally studied when they are in a state of magnetic saturation (the

so-called single domain), in the real scenario it does not necessarily mean completely homogeneous magnetization. Depending on their magnitude, the different interactions that create the internal effective field are also potential causes of inhomogeneous excitation. In other words, when the internal effective field varies locally, so will the magnetization, and the FMR excitation will be inhomogeneous. In turn, inhomogeneous resonance conditions will broaden the resonance linewidths and contribute to the emergence of nonuniform modes. In contrast with the uniform mode, for the nonuniform modes $k \neq 0$ and this means that actual spin waves transport magnetic energy across the material. This magnetic energy is quantized in the so-called magnons. Incidentally, another reason for the emergence of nonuniform modes are bulk, surface and interface defects [21].

1.3.3 Resonance frequency of a ferromagnetic film

Having treated the motion of the magnetization in a broad context, we now address a practical question that is going to be useful in determining the effective saturation magnetization (M_{eff}) of our samples (in Section 3.1.2), namely, the relation between the resonance frequency and the magnetic field applied to a ferromagnetic film (or dispersion curve).

This relation is established by a widely known equation called Kittel equation [34]. Although it implies a considerable simplification of the problem, it usually models with good approximation the dispersion curves of ferromagnetic thin films with low damping. It originates in the solution of Equation 5 (which does not include the damping term) for an applied static field (H_0). The only internal effect considered when defining the effective field is shape anisotropy. In its general form, the Kittel equation is valid for a cubic ferromagnetic insulator in the form of an ellipsoid, with demagnetization factors N_x, N_y and N_z:

$$\omega_{res} = \gamma \sqrt{H_0 + (N_y - N_z)M_{eff}} \sqrt{H_0 + (N_x - N_z)M_{eff}} \ . \tag{8}$$

This equation can be further simplified for the case in which the *x* and *y* dimensions of the ellipsoid are spread into infinity, turning it into a flat plate (or film). If the orientation of the applied field is in the *xy* plane, then $N_x = N_z = 0$ and $N_y = 4\pi$. We thus have

$$\omega_{res} = \gamma \sqrt{H_0 (H_0 + 4\pi M_{eff})} \ . \tag{9}$$

1.4 Two-magnon scattering versus the linear-response model

In FMR, indirect relaxation mechanisms involve decay of the uniform mode into nonuniform modes. As already mentioned, two-magnon relaxation is one of them. While three- and four-magnon scattering are only relevant in magnetic structures with ultra-reduced dimensions, like ultrathin films, where the precession angle is not limited by the exchange coupling, the occurrence of two-magnon scattering (TMS) may be present even in bulk materials. This difference arises from the fact that, unlike three- and four-magnon scattering, when the ferromagnetic resonance is operated in the ordinary small-angle regime, TMS may play a relevant role in the damping, bringing a nonlinear contribution to the linewidth. Due to the large influence of surface and interface defects in thin films, many of them exhibit this non-Gilbert type of damping. As the calculation of the linear-response damping is an important tool for the development of this Dissertation, it is important to determine whether two-magnon relaxation affects the Gilbert-damping-coefficient results for our samples or not. In fact, its presence might challenge the validity of the linear-response calculations [35].

Decay of the uniform mode happens when there is coupling with spin waves over a range of wave vectors which are degenerate with the zero-wave-vector mode. The coupling is assisted by inhomogeneities in the material that are of the order of these spin-wave wavelengths. The term "two-magnon scattering" comes from a theoretical formalism where a magnon from the uniform precession is destroyed and a spin-wave magnon at the same frequency is created. The process requires the presence of inhomogeneities, which in thin films are mostly caused by defects on surfaces and interfaces. It also requires that the magnetizing field is applied in the plane of the film, and that the film has an in-plane spontaneous magnetization [45].

The discovery of two-magnon scattering occurred in the early days of FMR studies of ferrites. The understanding of the origin of this extrinsic contribution to the linewidth allowed it to be eliminated through appropriate sample preparation, and this made the first ferrite devices possible [40]. In the case of thin films, special care must be dedicated in the manufacture, so that the structural and magnetic qualities of the films are extended to the quality of their surfaces, if two-magnon relaxation is to be avoided.

The description that follows is based on the model for two-magnon damping proposed by R. Arias and D. L. Mills in their 1999 article [46]. Although this model was originally proposed for ultrathin films, its validity has been proved to include thin films [38]. The FMR frequency dependence of the two-magnon contribution to the linewidth may be written [30] [40]:

$$\Delta H_{2mag}(\omega) = \boldsymbol{\Gamma} \sin^{-1} \sqrt{\frac{\left[\omega^2 + \left({\omega_S}^2/_2\right)^2\right]^{1/_2} - \frac{\omega_S}{2}}{\left[\omega^2 + \left({\omega_S}^2/_2\right)^2\right]^{1/_2} + \frac{\omega_S}{2}}}, \tag{10}$$

with $\omega_S = \gamma 4\pi M_{eff}$, where the effective magnetization $4\pi M_{eff}$ includes the anisotropy fields. $\boldsymbol{\Gamma}$ depends on the nature of the defects responsible for activating the two-magnon mechanism. Figure 5 shows a schematic diagram of ΔH_{2mag} along with the linear frequency dependence of the Gilbert contribution (ΔH_G). The two-magnon contribution shows a very steep nonlinear slope at low frequencies and a saturation at high frequencies. The diagram also shows the so-called inhomogeneous line broadening (ΔH_0), a linewidth contribution that originates in the local inhomogeneities of the magnetization and does not depend on frequency. (More on ΔH_0 in Section 1.7.)

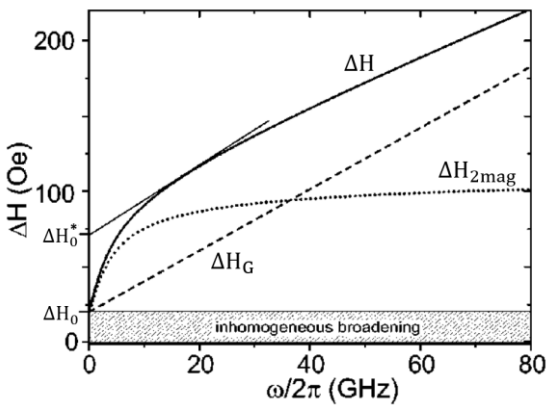

Figure 5: The graph shows three contributions to the frequency dependence of the FMR linewidth. The dashed line corresponds to the Gilbert-type damping, the horizontal line to the inhomogeneous line broadening and the dotted line to the two-magnon contribution, expressed in Equation 8. Typical FMR parameters were used. The solid line represents the total linewidth dependence. The tangent leading to an apparent zero-frequency linewidth ($\Delta H_0{}^*$) represents a possible misleading result due to data being restricted to a limited range of frequencies. From Ref. [35]

Linewidth data from FMR experiments over a large range of frequencies will give unambiguous evaluation whether only Gilbert-type damping (α_G) is present or two-magnon relaxation gives a relevant contribution. The scheme in Figure 5 indicates that, for FMR data over a range that is limited to the high frequencies where ΔH_{2mag} is saturated, two-magnon contribution might remain unnoticed. The tangent line shows that experimental data in a short range of frequencies might not reveal the nonlinear character of a two-magnon slope, indicating a false ΔH_0. But linear-response FMR linewidth data in the range of frequencies where the two-magnon contribution is expected to be most pronouncedly nonlinear would indicate that the two-magnon scattering, if present, is not relevant, compared with the linear contribution [35].

1.5 Spin-pumping and spin currents

Between 2001 and 2006, the experimental observation of spin pumping [47] [9] [48] and the direct [49] [50] and inverse [10] spin Hall effects furthered the emergence of spin-orbitronics, a trend in spintronic research where pure spin currents and torques originated in spin-orbit interactions became the object of intense investigation. One important outcome was transmission of electrical signals by spin waves travelling in a magnetic insulator [51] [52]. Another one was full compensation of the damping in a ferromagnet, using charge-to-spin current conversion in adjacent nonmagnetic metallic layers [53] [54] [55]. The former employs the direct and inverse spin Hall effects for charge-to-spin current interconversion at the terminals of a spin-wave transmitting material, so that the transmission of spin waves is electrically excited at one end and electrically detected at the other. The latter employs the spin Hall and Rashba-Edelstein effects to nonlocally affect the magnetization dynamics of a ferromagnet, which has also been used for domain-wall motion [56] and magnetization reversal [57]. The interplay between magnetization and spin currents is fundamental in spin-orbitronic studies. We now focus on the FMR-driven spin-pumping experiment and the concepts that surround it.

1.5.1 Pure spin currents

Spin-polarized currents are widely used in first-generation spintronic devices, like spin valves, and are at the core of the giant-magnetoresistance effect. They consist of an electric current where a relevant part of the conduction electrons' spins is oriented in a particular direction. In contrast to spin-polarized currents, a pure spin current may have the attribute of transporting spin angular momentum in the absence of charge flow. In practice, this happens in either of two forms: diffusive motion of conduction electrons in a nonzero spin density, and spin-wave propagation. A third way for the occurrence of pure spin currents is when spin-orbit effects actuate on a charge current causing electrons with opposite spin to move in opposite directions, transverse to the charge current. In this case, there is charge current involved, but the resultant spin current is transversal to it. Although in this case, and in the case of diffusive motion of conduction electrons in a nonzero spin density, the transport of spins is made by charge carriers, this does not imply a net transport of charge. The charge transport evens itself out. In the collective motion of electrons, there are the spin and charge degrees of freedom. Pure spin currents can thus be defined as the transport of angular momentum without an accompanying charge current [58]. Devices based on pure spin currents may reduce the presence of Oersted fields and Joule heating effects, thus representing a promise of high efficiency and low-energy cost [59]. The down side of pure spin currents is that they dissipate very quickly. Unlike charge currents, spin currents are not conservative, but subject to decay and dephasing [60].

Accumulation of spins is said when a relevant part of the conduction electrons' spins present in a certain region are oriented in a particular direction. Spin currents can be seen as spin accumulation is in motion. Because of the principle of minimal energy, accumulated spins tend to diffuse or flip, evening out spin orientations. Therefore, spin accumulation is always in motion, and is usually referred to as *nonequilibrium* spin accumulation. Another way of referring to spin accumulation, and maybe more precise, is *nonzero spin densities*.

Now, in the case of the propagation of spin waves, this kind of spin current is quite different. The energy of spin waves is quantized in magnons. Magnons have angular momentum, and when the wave vector of the spin wave is not zero ($\vec{\boldsymbol{k}} \neq 0$), there is transport of angular momentum, hence spin current. Spin-wave propagation is a potential means for the transmission of signals and processing of information, and there is today intense research for the development of this beyond-CMOS technology. In our study, we are mostly concerned with the spin current originated in the diffusion of nonzero spin densities. This will become clearer in the next Sections.

Detection of spin currents can be performed via optical techniques that reveal the nonequilibrium accumulation of spins, like Kerr rotation microscopy. Electrical detection of spin current is possible when it flows in a material with strong spin-orbit interaction, in which case the detection is said to be indirect, because what is actually detected is the electric potential caused by spin-to-charge current conversion. Spin-orbit interaction is also called *spin-orbit coupling*, our next topic.

1.5.2 Spin-orbit coupling

The interaction between the spin and orbital angular momenta of an electron, or the spin-orbit coupling (SOC) is causal in numerous magnetic phenomena in condensed matter, such as magnetocrystalline anisotropy, anisotropic magnetoresistance, antisymmetric exchange, Dresselhaus effect, Rashba-Edelstein effect (REE), anomalous Hall effect (AHE) and spin Hall effect (SHE). For this study, we are primally interested in the conversion of spin current into charge current that results from the reciprocal of the spin Hall effect, called the inverse spin Hall effect (ISHE). Eventual accompanying effects will also be considered. The fact that they only occur in materials with strong SOC prompts us to introduce this concept.

One way to understand the SOC is to adopt the Bohr model of the electron revolving around the nucleus, then letting the reference frame be that of the electron, and seeing the positively charged nucleus that now revolves around the electron as an electric current loop. This current naturally creates a magnetic field $\vec{\boldsymbol{B}}$ traversing the loop, and the spin of the electron will tend to align with it. The SOC would then consist of the energy shift corresponding to this alignment,

$E_{SO} = \lambda\, \vec{\boldsymbol{l}}.\vec{\boldsymbol{s}}$, where λ is the spin-orbit coupling energy, and $\vec{\boldsymbol{l}}$, $\vec{\boldsymbol{s}}$ are dimensionless operators corresponding to the orbital and spin angular momenta, respectively.

Figure 6: Spin-orbit interaction from the point of view of the electron. (From Ref. [20])

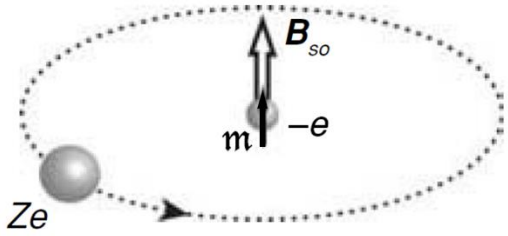

Although this classical model is useful to understand the spin-orbit interaction, and offers a fairly good quantitative approximation of its energy in the case of the electron orbiting in an atom (it gives the actual value modified by a factor 2), the SOC can only be fully explained by the relativistic quantum-mechanical theory of the electron (developed by Paul Dirac), where one of the terms of the Hamiltonian, namely, $\mathcal{H}_{SO} \propto (dV/dr)\, \vec{\boldsymbol{l}}.\vec{\boldsymbol{s}}$, accounts for the SOC [20]. It can be inferred from this term that the strength of the SOC depends on the configuration of the electric potential where the electron is inserted. Electric potential configurations that provide strong SOC are found in certain surfaces, crystal lattices and atomic orbitals. Impurities in a lattice may also configure strong-SOC electric potentials. In particular, the SHE occurs in metals (and metal alloys) whose elements are characterized by a strong $\vec{\boldsymbol{s}}$ - $\vec{\boldsymbol{l}}$ coupling due to atomic orbital configuration [61].

1.5.3 Spin Hall and other spin-to-charge current interconversion effects

Spin Hall effect

In 2004, with the help of Kerr rotation microscopy, opposite spin polarizations on either side along a semiconductor wire bearing electric current was observed [49]. In the effect, which had already been predicted and named *spin Hall effect* [62] [63], a charge current generates transverse spin currents polarized perpendicular to the plane defined by the directions of the charge and spin currents (Figure 7a and Figure 7b). If compared to the Hall effect (Figure 7c), which only involves the charge degree of freedom of the electron and is a direct consequence of the Lorentz force actuating on charge carriers moving in a magnetic field, one remarkable difference is that there is no need of an applied magnetic field for the spin Hall effect to occur. Another difference is, of course, that spin currents and the spin degree of freedom are involved. The spin Hall effect (SHE) is a relativistic spin-orbit coupling phenomenon whereby a charge

current flowing in a conducting material (magnetically ordered or not) generates a transversal spin current. Some nonmagnetic transition metals, like Ta, W, Ir and Pt, have been found to exhibit large SHE, and used to create new experiments and devices. Spin-current driven magnetization reversal of adjacent FMs using SHE has introduced an entirely new concept for writing information and boosted the interest in spin-orbitronic research [60]. The spin Hall effect can be caused by extrinsic mechanisms known as *skew scattering* and *side-jump scattering* (Figure 7d), which originate in the collision of charge carriers with imperfections in the lattice (like defects or foreign atoms). Or it may originate in certain configurations of the electric potential of the lattice, where nonlocal electrons transit, in this case receiving the attribute of *intrinsic* SHE. (Cf. Section 1.5.2.)

The charge-to-spin current conversion caused by SHE is given by

$$\vec{J}_s = \theta_{SH} \frac{\hbar}{(-2e)} \vec{J}_c \times \hat{\sigma}\,, \tag{11}$$

where θ_{SH} is the spin Hall angle, characteristic of the material, e is the electron charge, and $\hat{\sigma}$ is the spin-polarization unit vector of the spin current [60]. The minus sign in the parentheses cancels out because the value of the electron charge (e) is negative. The spin Hall angle (θ_{SH}) is a dimensionless parameter that expresses how efficient the material is in converting charge current into spin current. Depending on the material, θ_{SH} can be positive or negative. By convention, it was established that the spin Hall angle of platinum is positive. The sign of θ_{SH} for all other materials were henceforth attributed by comparison.

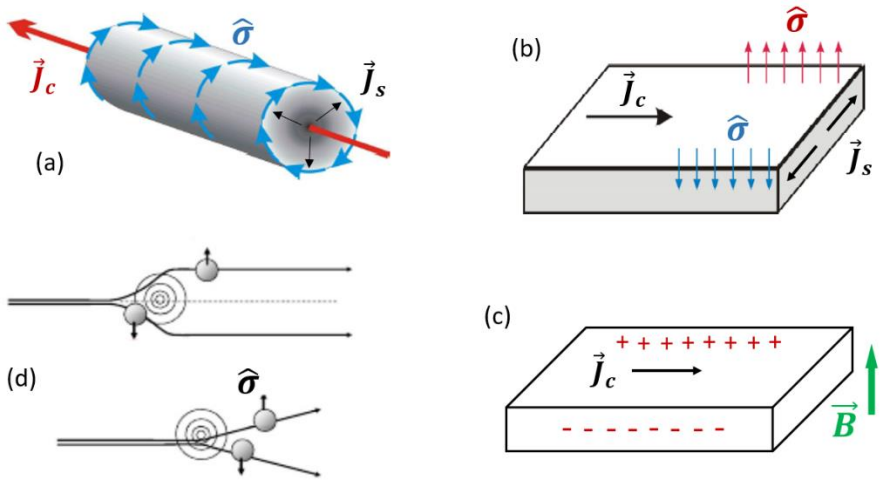

*Figure 7: **Hall and spin Hall effects**. (a) Nonequilibrium spin accumulation on the surface of a cylinder, caused by SHE; (b) Nonequilibrium spin accumulation on the edges of a flat plate, caused by SHE. (c) Electric potential on the edges of a flat plate, caused by Hall effect. (c) Conduction electrons with opposite spin orientation colliding with a defect may side jump (above) and skew scatter (below) under the influence of SOC.*

There exists a process reciprocal to SHE, whereby a spin current generates a transverse charge current, perpendicular to the plane defined by the spin current flow and its polarization. It is governed by the same mechanisms as SHE and called the inverse spin Hall effect (ISHE). The direct and inverse spin Hall effects enable conductors with strong SOC to be respectively utilized for the generation and detection of spin currents [64]. The spin-pumping experiment described in Section 1.5.4 shows an application of this effect in the electrical detection of spin currents.

Rashba-Edelstein effect

The material structure of some interfaces and surfaces presents spatial inversion asymmetry, which in the presence of SOC converts charge currents into transverse spin currents, according to a geometry analogous to SHE. This is the Rashba-Edelstein effect [11] [65] and those are called Rashba surfaces and interfaces. While SHE is a bulk-material effect, REE affects the 2D electron gas of the Rashba surfaces and interfaces. Heavy elements characterized by strong SOC, (e.g., Bi, Pb and W) can give large Rashba coupling. The interface of Bi with nonmagnetic materials, like Ag, Cu or Si, has been used for highly efficient charge-to-spin current conversion.

REE also has its reciprocal effect, the inverse Rashba-Edesltein effect (IREE). Rashba interfaces are used in spintronic devices to control the magnetization of adjacent ferromagnets [66] [56] [67], or to generate and detect spin currents. Figure 8 shows an experiment reported in Ref. [11], where a Bi/Ag interface converts spin current created by spin-pumping on a NiFe/Ag interface into charge current and electric potential via IREE. The use of SHE and ISHE in devices involve interfaces and surfaces, so these effects are often accompanied by REE and IREE, respectively [60] [68] [69]. The relevance of these accompanying effects will depend on characteristics of the devices' interfaces and surfaces, concerning broken inversion asymmetry and SOC. The Rashba-Edelstein effect is sometimes called inverse spin-galvanic effect [60] [70], while in this work we adopt the former nomenclature.

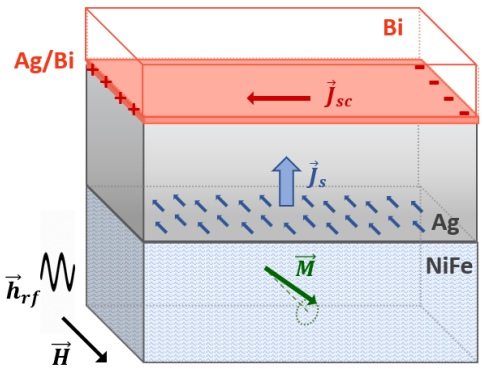

Figure 8: Example of device using IREE for electrical detection of spin current. (Adapted from Ref. [11])

Anomalous spin Hall effect

Metallic ferromagnets can also be used for electrical detection of spin currents. Spin-to-charge current conversion has been investigated in metallic ferromagnets under the assumption that it is only due to ISHE. Between 2013 and 2014, several groups investigated the spin-to-charge current inter-conversion in permaloy [59] [71] [72] [73] [74]. Their results raised the point that a spin current will always accompany the charge current caused by the AHE and that this spin current will vary with the angle between the magnetization and the charge current [75]. Even more recently (2017), Das *et al.* [12] called this spin current the *anomalous spin Hall effect* (ASHE), demonstrated the presence of both the SHE and the ASHE in Py and measured how the ratio of their efficiencies varies with the angle between the applied magnetizing field that actuates on the spin-injector material (YIG, in this case) and the magnetization of the m-FM that is playing the role of a spin sink. (This angle can be controlled by pinning the m-FM layer or by shape anisotropy, for example.) The angle is zero when the magnetization of the spin injector and the m-FM spin sink are aligned, and this is when the contribution of ASHE to the spin-to-charge current conversion is maximized. In our YIG/spacer/m-FM structures (Section 1.5.5), this alignment will always be the case, because both YIG and m-FM will align with the magnetizing field. So, we have to assume that ISHE and ASHE are companion effects when we measure the voltage induced by spin-to-current conversion in our samples.

1.5.4 The spin-pumping prototype

Spin pumping is much more than a damping mechanism (cf. Section 1.2). Its contribution to the damping is just one aspect of this interfacial phenomenon, which involves the precessing magnetization of a ferromagnet, on one side of the interface, and conduction electrons of a nonmagnetic material, on the other (Figure 9). The precessing magnetization injects magnetic moment across the interface, actuating in a way that resembles a peristaltic pump. The magnetic moment thus transmitted is absorbed by conduction electrons on the other side, and this generates a time-dependent spin current that is pumped into the NM, and is given by

$$J_{s,pump}\hat{\boldsymbol{\sigma}}(t) = \frac{\hbar\omega}{4\pi} A_r \hat{\boldsymbol{m}} \times \frac{d\hat{\boldsymbol{m}}}{dt}\,, \tag{12}$$

where $\hat{\boldsymbol{m}}(t)$ is the unit vector of the magnetization, $\hat{\boldsymbol{\sigma}}$ is the unit vector of the spin-current polarization, $J_{s,pump}$ is the magnitude of the pumped spin current, and A_r is a proportionality constant that depends on the sample [60]. As the magnetization precesses, the spin current generated on the other side of the interface is time dependent, but when averaged over time it has a nonzero component, which is given by

$$\bar{J}_{s,pump} = \frac{\hbar\omega}{4\pi} A_r \sin^2\phi \ , \tag{13}$$

where ω is the angular velocity of the precession at microwave frequency, and ϕ is the precession angle of the magnetization. This current is sometimes called *dc spin current*.

At spin-pumping interfaces, the ferromagnetic material whose magnetization transmits angular momentum is called *spin injector* and the material that absorbs it is called *spin sink*. Assuming that the NM in Figure 9 is a perfect spin sink, i.e., that it completely dissipates the spins accumulated via spin pumping, A_r will only depend on the ability of the interface to transmit spins. But if, for example, the volume of the NM in the sample is not enough for it to dissipate the spins as they are injected by the FM, then the spin accumulation in the NM will "overflow", and spin current will traverse the interface back to the FM material. This is called the *spin-current backflow*, and it is represented in Figure 9 as $\vec{J}_{s,back}$.

The details of the mechanism whereby the magnetic moment of the magnetization precession is transmitted to conduction electrons of the NM are out of the scope of this thesis, but it is worth mentioning that this mechanism is the Onsager reciprocal of the so-called spin transfer torque (STT), which explains how spin polarized currents actuate on the magnetization dynamics of ferromagnetic layers in first-generation spintronic devices.

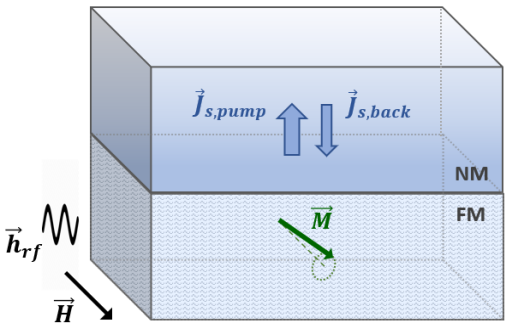

Figure 9: Diagram representing a FM/NM interface, where the FM is driven into resonance, with dc magnetic field applied parallel to the interface. It shows a spin current pumped into the NM side of the interface, and a backflow current traversing the interface in the opposite direction.

The most elementary structure where a spin-pumping experiment (Figure 10) can be performed consists of a thin-film bilayer, where a ferromagnetic material excited into FMR injects spins across the interface and into a nonmagnetic metal with strong SOC. The resultant nonequilibrium spin accumulation near the interface diffuses into the metallic layer. Assuming that the injection of spins is homogeneous over the extension of the interface, their diffusion corresponds to a spin current perpendicular to the plane of the interface. If the metal of the nonmagnetic layer did not have a strong SOC, the spin current would simply dissipate and we

would not be able to electrically detect it. (In this model, we are assuming that there is no relevant contribution of IREE in spin-to-charge current conversion.) Strong SOC guarantees that the spin current will be converted to charge current via ISHE, enabling electrical detection. Figure 10 indicates the orientation and polarity of the electric potential created by this conversion, assuming that the spin Hall angle of the NM is positive ($\theta_{SH} > 0$). Note that the orientation of the conduction-electron spins accumulated at the interface is antiparallel to the applied magnetic field, because of their negative electric charge.

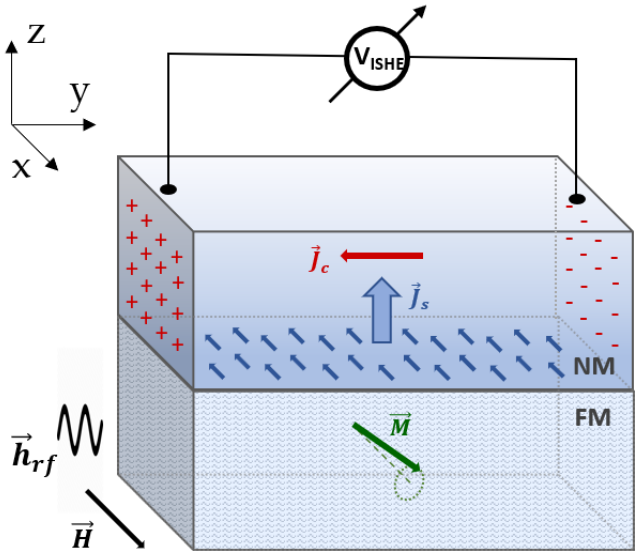

Figure 10: Spin-pumping experiment prototype. The magnetization precession of the FM layer driven into FMR pumps magnetic moment across the interface with the NM layer. Conduction-electron spins with orientation antiparallel to the magnetization of the FM accumulate near the interface and diffuse into the NM layer. The spin current ($\vec{J}_s$) is converted into charge current ($\vec{J}_c$) via ISHE, creating an electric potential (V_{ISHE}) transverse to the magnetization ($\vec{M}$).

The spin current represented in Figure 10 by $\vec{J}_s$ is the addition of the pumped spin current and the spin-current backflow. Its time-averaged value can be expressed as [60] [76]:

$$J_s = \frac{\hbar\omega}{4\pi} Re(g_{\uparrow\downarrow}) P \lambda_{sd} \tanh\left(\frac{t_{NM}}{2\lambda_{sd}}\right) \sin^2\phi \ , \qquad (14)$$

where $Re(g_{\uparrow\downarrow})$ is the real part of the interfacial spin mixing conductance, a complex parameter that originates in the scattering-matrix theory, and which is characteristic of the interface [60]. The term $\lambda_{\mathrm{sd}} \tanh(t_{\mathrm{NM}}/2\lambda_{\mathrm{sd}})$, where λ_{sd} is the spin-diffusion length of the NM metal, accounts for the backflow of spin current due to finite layer thickness [76]. (Cf. Equation 13.) In Equation 14, we are also introducing a factor P, which arises from the ellipticity of the magnetization precession [76]:

$$P = \frac{2\omega\left[\gamma 4\pi M_s + \sqrt{(\gamma 4\pi M_s)^2 + 4\omega^2}\right]}{(\gamma 4\pi M_s)^2 + 4\omega^2}, \tag{15}$$

where γ is the gyromagnetic ratio and M_s is the saturation magnetization of the FM.

Considering that for materials with low damping the cone angle is small (ϕ ~ 1º or less), and that for most interfaces the real part of $g_{\uparrow\downarrow}$ is much larger than the imaginary part, Equation 14 can be reduced to

$$J_s = \frac{\hbar\omega}{4\pi} g_{\uparrow\downarrow} \left(\frac{\gamma h_{rf}}{2\alpha\omega}\right)^2 P\lambda_{sd} \tanh\left(\frac{t_{NM}}{2\lambda_{sd}}\right). \tag{16}$$

The spin mixing conductance expresses the number of spin channels per unit area of the interface, and corresponds to the ability of the interface to transmit spins. It can be theoretically calculated from the electronic band structures at the FM/NM interface, but it can also be empirically determined through the expression

$$g_{\uparrow\downarrow} = \frac{4\pi M_s t_{FM}}{g\mu_B}\left(\alpha_{FM/NM} - \alpha_{FM}\right), \tag{17}$$

where t_{FM} is the thickness of the FM layer, g is the Landé factor and μ_B is the Bohr magneton, while α_{FM} and $\alpha_{FM/NM}$ are the Gilbert damping constants of the FM layer and the FM/NM bilayer, respectively [76]. In parentheses, we have the damping enhancement of the FMR resonance in the FM layer, due to the escape of angular momentum into the spin sink. It can be obtained by FMR characterization of the FM film, whereby α_{FM} is determined, and of the FM/NM bilayer, whereby $\alpha_{FM/NM}$ is determined. Section 1.7 describes in detail the calculation of the Gilbert damping parameter from FMR linewidths. Figure 11 shows an example of damping enhancement (which in this case results 3.6×10^{-3}).

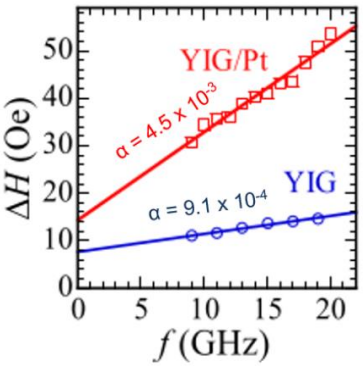

Figure 11: Frequency dependence of the FMR linewidth. In this example, the FM layer is YIG (20 nm) and the NM layer is platinum (5 nm). The linear fit to the experimental data gives a Gilbert damping parameter of 9.1 x 10^{-4} for the bare YIG film. For the YIG/Pt bilayer, the damping parameter results 4.5 x 10^{-3}. (From Ref. [77])

The equation that describes the conversion of spin current into charge current via ISHE (cf. Equation 11) is

$$\vec{\boldsymbol{J}}_{\boldsymbol{c}} = \theta_{SH}\frac{(-2e)}{\hbar}\vec{\boldsymbol{J}}_{\boldsymbol{s}} \times \hat{\boldsymbol{\sigma}}\,. \tag{18}$$

The electric potential that builds across the metallic layer, perpendicular to the applied magnetic field, as indicated in Figure 10, is given by [76]:

$$V_{ISHE} = \frac{2e}{\hbar}\frac{1}{\sigma_{NM}t_{NM} + \sigma_{FM}t_{FM}}\theta_{SH}L\,J_s\,, \tag{19}$$

where σ and t are the electrical conductivity and thickness, respectively, of the NM or FM layer, according to the subscripted letters, L is the sample length (along the *y*-axis in Figure 10).

Assuming that spins are pumped from an FM insulator (σ_{FM} = 0), and substituting J_s (Equation 16) in Equation 19, we have:

$$V_{ISHE} = \frac{e}{\sigma_{NM}t_{NM}}\left(\frac{\gamma h_{rf}}{4\pi\alpha f}\right)^2 \theta_{SH}g_{\uparrow\downarrow}fLP\lambda_{sd}\tanh\left(\frac{t_{NM}}{2\lambda_{sd}}\right). \tag{20}$$

Here, we remind that the term $\lambda_{\mathrm{sd}}\tanh(t_{\mathrm{NM}}/2\lambda_{\mathrm{sd}})$ accounts for the suppression of spin current due to finite layer thickness [76]. In other words, when the NM layer is not thick enough to let the spin current fully evolve and dissipate along its path, spin-current backflow occurs and the total spin to charge current conversion in the NM layer is reduced. It is possible, therefore, to obtain λ_{sd} by fitting V_{ISHE} measurements to $\lambda_{\mathrm{sd}}\tanh(t_{\mathrm{NM}}/2\lambda_{\mathrm{sd}})$, as shown in Figure 12.

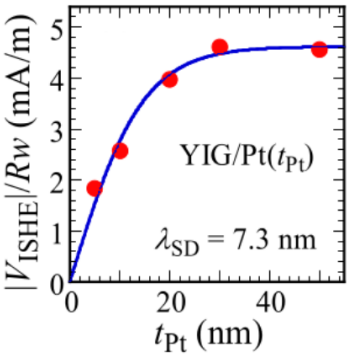

Figure 12: ISHE-induced charge current (V_{ISHE}/R), normalized by sample width (w), for a series of YIG(20nm)/Pt bilayers. The blue line is the fit, from which the spin-diffusion length of Pt, λ_{SD} = 7.3 nm, is obtained. (From Ref. [78].)

The simplified spin-pumping model presented above provides some basic relations between figures of merit, while simultaneously giving the feel of the physics behind the spin-pumping "machine". Stemming from its experimental nature, this model also provides an

experimental protocol to determine, among the figures of merit, the spin mixing conductance ($g_{\uparrow\downarrow}$), which is a characteristic of the FM/NM interface, as well as the spin-diffusion length (λ_{sd}) and the spin hall angle (θ_{SH}), which are characteristics of the NM material. It is important to mention that the determination of these parameters for a specific material or interface strongly depend on experimental conditions and that their values have been calculated with an irregular level of agreement among different research groups. While we consider it important to get acquainted with these figures of merit for the correct understanding of this study, it is not our intention (nor is it necessary, in the scope of this study) to calculate the above-mentioned parameters for the materials and interfaces used in this project.

Having discussed these concepts, we introduce in the next Section the trilayer structure that is the main theme of this thesis. Instead of V_{ISHE}, we are going to call the measured voltage V_{sc} to highlight the fact that other effects, like IREE and ASHE, may contribute to the electric potential via spin-to-charge current conversion.

1.5.5 The YIG/spacer/m-FM structure

As compared to the FM/NM spin-pumping prototype, in the YIG/spacer/m-FM structure YIG becomes the FM spin injector, and a metallic ferromagnet (m-FM) replaces the NM in the role of spin sink. Contact between the two FMs is avoided with the inclusion of a spacer. The YIG/m-FM junction has been used in the investigation of the ASHE [12] [79], and the YIG/spacer/m-FM trilayer for the determination of the spin Hall angle of m-FMs [80]. In our study of this structure, the YIG layer is driven into ferromagnetic resonance, generating spin current (Figure 13). Our initial assumption is that this spin current traverses the spacer and is absorbed by the m-FM layer. The YIG layer is the spin injector (or active FM) and the m-FM is the spin sink (or passive FM). The difference in the resonance conditions for one FM and for the other lets us assume that, when the active FM is driven into FMR, the passive FM will stay relaxed (at least comparatively).

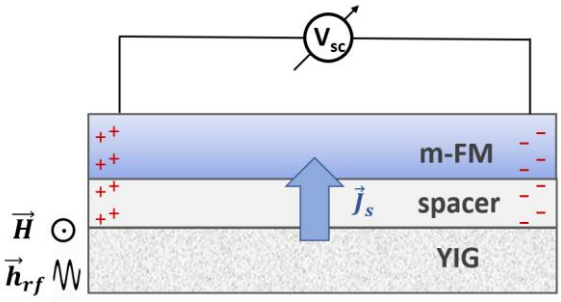

Figure 13: Diagram of the YIG/spacer/m-FM structure. The spin current $\vec{j}_s$ is injected into the spacer layer when the YIG layer is driven into FMR. The in-plane magnetizing field points outwards from the plane of the page.

The spacer is supposed to prevent static magnetic coupling between the FM layers [71] and to allow spin currents to flow between them with minimum dissipation. In this work, Ag and Cu are used as spacers. They are nonmagnetic metals, so they can provide magnetic isolation by spacing the FM layers, thus magnetically uncoupling them. And they have large spin-diffusion length (in the order of 10^2 nm) [81] [82], which is necessary for the conduction of spin currents with minimal dissipation. The m-FMs studied as spin-sink layer in our samples are Ni and $Co_{20}Fe_{60}B_{20}$.

By comparing Figure 8 and Figure 10, it becomes clear that, when both ISHE and IREE contribute to the spin-to-charge current conversion in a sample, they participate in building the electrical potential across the same edges, i.e., the edges that lie transversal to the magnetizing field. And as mentioned in Section 1.5.3, ASHE will also participate when the spin sink is a m-FM. The measured voltage V_{sc} (Figure 13) is a signature of spin currents transiting the trilayer, and is a consequence of spin-to-charge current conversion, regardless of how much each of those three effects contributes to it.

1.6 Yttrium iron garnet (YIG)

All species of garnets have similar physical properties and crystalline structure, but differ in chemical composition. In nature, they are found in every color, but reddish shades are most common. In its origin, the English word *garnet* was borrowed from the French word *grenat* and meant “dark red”. Their etymological root is the latin word *granatus*, which means “containing many grains”. It is believed that the vivid red color of pomegranate seeds suggests an etymological bridge between the fruit and the gemstones Figure 14.

Figure 14, left: A garnet raw crystal from Jeffrey Mine, in Canada. Above: An open pomegranate fruit (© Anton Croos, Art of Photography).

Garnets’ general formula is $\boldsymbol{X}_3\boldsymbol{Y}_2(SiO_4)$. The ***X*** site is usually occupied by divalent cations (e.g., Ca, Mg, Fe or Mn) and the ***Y*** site by trivalent cations (e.g., Al, Fe or Cr). In synthetic garnets, silicon can be replaced by another element (e.g., Fe, Al or Ga) and the ***X*** site is usually occupied

by a rare-earth element (e.g., Yttrium, Gadolinium or Lutetium). Garnets do not have any cleavage planes, so when they fracture under stress, sharp, irregular pieces are formed. Yttrium is a transition metal and its place in the periodic table is on the 3rd column. The similarities between yttrium to the lanthanides are so strong that the element has been grouped with them as a rare-earth element. Besides, it is commonly found in nature among rare-earth minerals.

YIG was first synthesized in 1956, by Bertaut and Forrat, and had its crystalline structure elucidated by Geller and Gilleo in 1957 [83]. Bulk YIG crystal was extensively used in FMR studies in the mid-twentieth century to understand high-frequency magnetization dynamics [84]. Among the properties that turned researchers' attention to YIG are: electrical insulation, high chemical stability, low dielectric losses, good magnetic saturation magnetization (1750 G) [85] and high Néel temperature (559 K). But its most impacting feature is a damping parameter of approximately 3×10^{-5} (bulk) [86], which is the smallest among all known materials at room temperature.

The structure of magnetic oxides enables the accommodation of similar cations at different sites, producing a wide variation in properties. The magnetic properties of YIG originate in the interaction between Fe ions in specific crystallographic sites, similar to those of magnetite (Fe_3O_4) and maghemite (γ-Fe_2O_3), which belong to the spinel group. Like magnetite and maghemite, YIG ($Y_3Fe_5O_{12}$) has iron ions in tetrahedral and octahedral sites. Ions from these sites couple magnetically through the so-called superexchange interaction, which results in antiparallel alignment of spins [87]. However, they do not cancel out. Because the magnetic moments of iron ions occupying tetrahedral and octahedral sites are not equal, this coupling results in a net magnetic moment, which is the origin of the ferrimagnetic characteristic of these materials. Most of the macroscopic properties of ferrimagnetism are similar to ferromagnetism, although they originate in a different magnetic ordering [88] [89] [90].

In the YIG structure, the yttrium ion, which occupies a dodecahedral site, also takes part in the coupling of unpaired spins, contributing to the ferrimagnetic ordering [83] [91]. Figure 15 (right) shows a diagram of the YIG structure, where 160 atoms are arranged in irregular and slightly twisted tetrahedra, octahedra and dodecahedra, inside a pseudocubic unit cell presenting bcc symmetry. All sites are coordinated by oxygen ions (Figure 15, left). Each unit cell has 16 Fe^{+3} ions in tetrahedral sites, 24 Fe^{+3} ions in octahedral sites and 24 Y^{+3} ions in dodecahedral sites, coordinated by 96 O^{-2} ions. Because the magnetic ordering of YIG is directly related to its crystal structure, the desired magnetic qualities, like low damping and high saturation magnetization, depend on the achievement of thorough crystallization of a pure YIG phase. Crystalline YIG is transparent for wavelengths over 600 nm, and the YIG crystal has a slightly brownish, translucent aspect.

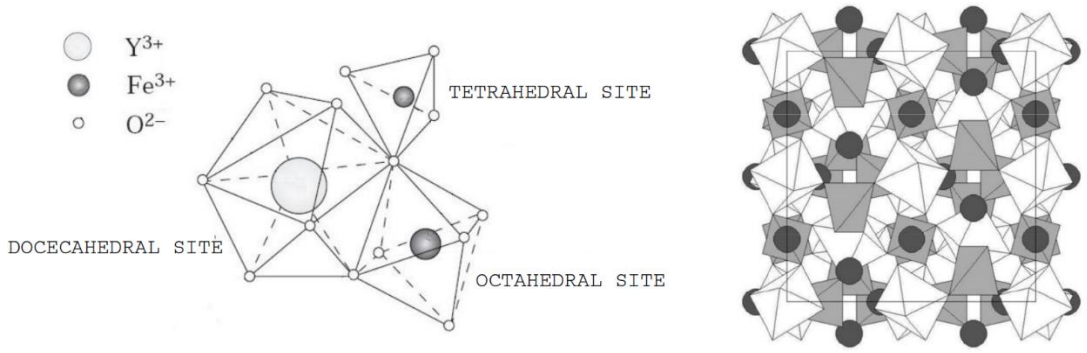

Figure 15: Crystal structure of YIG. On the left, a representation of the sites occupied by Y^{+3} and Fe^{+3} ions, coordinated by O^{-2} ions. On the right, a diagram of the spatial distribution of the tetrahedral and octahedral sites in a YIG unit cell, where the yttrium ions are represented by circles. Adapted from [91].

YIG has been applied in telecommunication and magneto-optic engineering. A YIG-based microwave industry has created a large number of microwave devices, like delay lines, oscillators and filters. Several traditional methods, like coprecipitation, microwave synthesis and sol-gel, may be used to fabricate YIG powder [89].

In the years of 2010 and 2011, YIG in the form of thin films started a new paradigm in the field of spintronics. Liquid phase epitaxy (LPE) was the first technique used to deposit YIG films and is still considered the best technique for the growth of micron-thick YIG films. Pulsed laser deposition (PLD) and magnetron sputtering are the most applicable techniques for the deposition of submicron-thick YIG films [86]. Fabrication of YIG thin films involves high temperatures (usually post-annealing) to attain crystallization. Substrates are chosen according to the application to which the films are destined.

To obtain monocrystalline YIG thin films, substrates of monocrystalline gadolinium gallium garnet (GGG) with <111> orientation must be used. YIG and GGG have the same crystalline structure and almost identic lattice parameters (12.376 and 12.383 Å, respectively). Their lattice mismatch is approximately 0.06%. Same crystalline structure combined with small lattice mismatch promotes epitaxial growth. The use of other substrates, like Si, oxidized Si and MgO, which we refer to as nonconventional substrates, are intended for the integration of YIG-based devices with electronic and optical circuits, but they only support the growth of polycrystalline YIG, which does not exhibit optimized magnetic qualities. The FMR linewidth of polycrystalline YIG, for example, is one order of magnitude broader than that of monocrystalline YIG. The lattice parameters of MgO and Si are equal to 4.212 and 5.431 Å, respectively. They are very different from YIG's. However, one could expect that MgO might support epitaxial growth of YIG, because the lattice mismatch of three MgO unit cells and one YIG unit cell is only 2%. In practice this is not verified, probably because a YIG crystal is characterized by the intricate

garnet structure, while MgO conforms the regular face-centered cubic crystal structure [92] [93] [94].

Surface quality depends on the implementation of a controlled O_2 atmosphere during the annealing to prevent stoichiometry imbalance due to loss of oxygen. Surface quality impacts the magnetization dynamics of magnetic samples based in YIG thin films in a three-fold way: it is directly related to the inhomogeneous broadening of resonance lines (Section 1.7), it may determine the relevance of two-magnon scattering in relaxation (Section 1.4), and when a metallic layer is added, it influences the spin mixing conductance of the interface created (Section 1.5.4).

The magnetic anisotropy in monocrystalline YIG thin films is predominantly determined by shape anisotropy. Out of plane magnetization demands more intense magnetizing fields, while in-plane magnetization is easier and isotropic. All measurements for the magnetic characterization of samples in this work were performed with an in-plane magnetizing field.

YIG as a spin injector

Spin-pumping experiments have often been made using a metallic FM as spin injector, but the electrical detection of spin currents generated this way is sometimes found to be compromised [64]. This is attributed to two main reasons. Firstly, the metallic FM layer contributes to electrical conduction, reducing the electrical signal, which, ideally, should run exclusively in the NM layer. Secondly, the metallic FM layer itself may contribute to the detected voltage with self-induced spin and charge currents interconversion resulting from SOC-type effects [73]. The use of an insulator FM (instead of a metallic FM) as spin injector in spin pumping experiments avoids both these hindrances. As we know, YIG is an insulator. Besides, its low damping increases the power efficiency of spin pumping. YIG is today widely used as spin injector in spin-pumping experiments.

1.7 FMR absorption linewidth dependence on frequency (Calculation of the Gilbert damping from experimental FMR data)

From the concepts presented in Section 1.3, it can be said that, in the small-angle regime, the FMR absorption line of a monocrystalline ferromagnetic thin film is expected to produce a peak in Lorentzian shape when the uniform field is swept near the resonance condition. The data from such FMR measurement can be approximated by a Lorentzian function using a fitting program. The Lorentzian absorption, outlined in Figure 16 (left), can be expressed as

$$P_{abs}(H) = P_{max}\frac{{\Delta H_{HWHM}}^2}{(H - H_{res})^2 + {\Delta H_{HWHM}}^2}\,, \tag{21}$$

where ΔH_{HWHM} denotes the linewidth, in the half-width-at-half-maximum (HWHM) convention. Alternately, the "full-width-at-half-maximum" format may be found in the literature. It corresponds to $\Delta H_{FWHM} = 2\Delta H_{HWHM}$, as indicated in Figure 16 (left).

Because of its improved accuracy, the experimental method (described in Section 2.1) usually adopted to obtain data from the FMR absorption behavior uses modulation of the magnetizing field $\vec{\boldsymbol{H}}_{\mathbf{0}}$ to directly measure the derivative of the absorbed power. The characteristic shape of this derivative is depicted in Figure 16 (right). A third way of defining the linewidth, frequently found in literature, emerges from this configuration. It is called the peak-to-peak linewidth, and corresponds to

$$\Delta H_{pp} = \frac{2}{\sqrt{3}}\Delta H_{HWHM}\,. \tag{22}$$

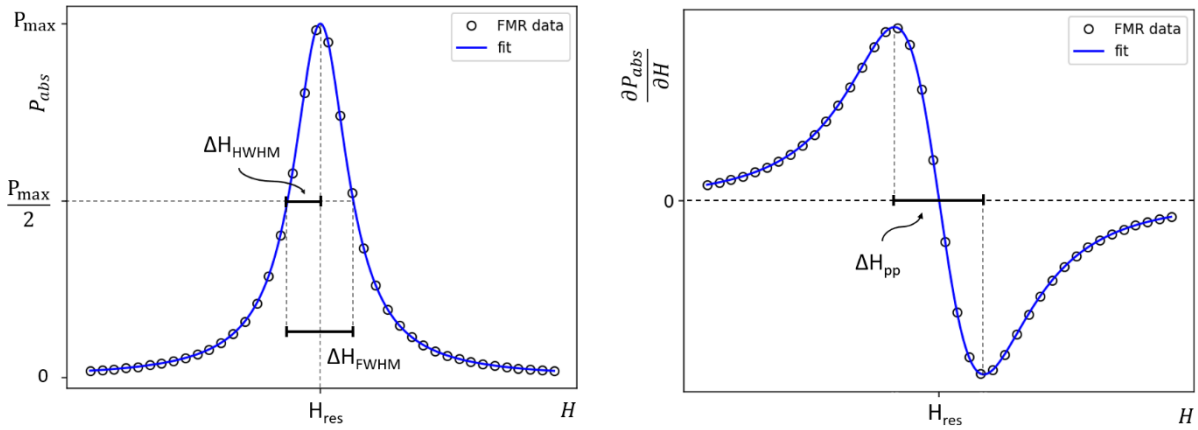

Figure 16: Schematic representations of typical field-swept FMR data and their respective Lorentzian fit. On the left, an absorbed-power spectrum is represented along with the indication of the HWHM and the FWHM linewidths. On the right, a power-derivative spectrum, along with the indication of the peak-to-peak linewidth.

By performing several sweeps, each in a different frequency, it is thus possible to build a plot of the linewidth dependence, in a determined frequency range. If the plot shows linear behavior, this is evidence that only direct relaxation mechanisms contribute to the linewidth. A linear fit to the points of this plot will give the Gilbert-damping parameter (α_G). Figure 17 (left) shows the linewidth frequency dependence of a sample that exhibits linear response. From the LLG equation (applied to the parallel or perpendicular magnetization of thin films in FMR), it is possible to obtain the linear dependence [38]:

$$\Delta H_{HWHM} = \frac{\alpha_G}{\gamma}\omega_{res}\,. \tag{23}$$

In many magnetic systems, while a linear behavior is observed, the linewidth fails to extrapolate to zero with vanishing frequency. Instead, the extrapolation of the linear fit yields a rather substantive zero-frequency linewidth (Figure 17, right) [42] [46]. This occurs because there is no spatial resolution in ordinary FMR and the length scales relevant to the measurements are macroscopic, so inhomogeneities in the magnetization or in anisotropy fields will appear as a frequency-independent contribution to the linewidth [35]. This contribution is known as "inhomogeneous line broadening" and denoted as ΔH_0. Equation 23 then becomes:

$$\Delta H_{HWHM} = \Delta H_0 + \frac{\alpha_G}{\gamma}\omega_{res}\,, \tag{24}$$

which is used to calculate α_G and ΔH_0 from the linear fit of the experimental data. Notice that the linewidth format used in Equations 23 and 24 is HWHM. This convention is adopted throughout this Dissertation.

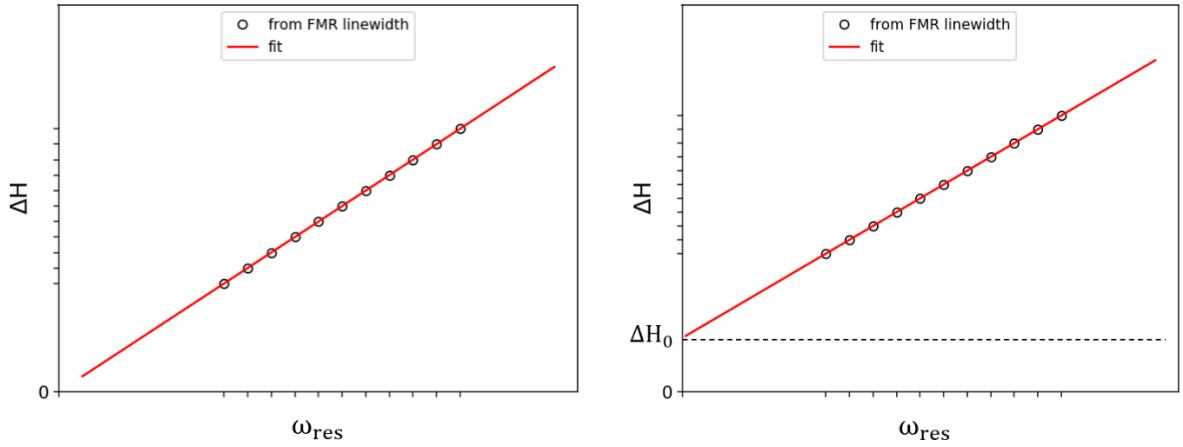

Figure 17: Representation of FMR linewidth dependence on frequency for two hypothetical samples. Both exhibit linear response. On the right, extrapolation to zero frequency of the linear fit demonstrates inhomogeneous line broadening ΔH_0.

At this point, a comment on the gyromagnetic ratio (γ) is required. It is always good to remember from basic theory of magnetism that γ is defined as the proportionality constant between a magnetic dipole moment $\vec{\boldsymbol{m}}$ and the angular momentum of the associated current loop. This definition is equally valid for a particle, a macrospin or magnetization. Still from basic theory, the result of the action of a magnetic field $\vec{\boldsymbol{H}}$ on a magnetic moment $\vec{\boldsymbol{m}}$ is a torque $\vec{\boldsymbol{m}} \times \vec{\boldsymbol{H}}$. It is therefore through the gyromagnetic ratio that the motions of the magnetic and mechanical

moments are connected in Equation 1. Now, when a macrospin or magnetization in a ferromagnetic material is concerned, we are basically dealing with electron-spin magnetism, so the γ seen in Equations 23 and 24 could be made equal to the gyromagnetic ratio of the electron ($\gamma_e = 1.76\, rad/s\, T$). Sometimes, however, the actual γ of a ferromagnet may differ noticeably from γ_e. This deviation is caused by additional orbital magnetism being mixed with the basic spin magnetism in ferromagnets through spin-orbit interaction [21].

Equation 2 seems to indicate an experimental FMR method to determine the actual γ of a ferromagnetic material, but caution should be taken. In real samples, instead of the applied $\vec{\boldsymbol{H}}_0$ field, the magnetization "sees" the effective $\vec{\boldsymbol{H}}_{eff}$ field (as stated in Equation 4), which we may not know beforehand [21]. Nevertheless, this should not be a concern when establishing a value to the gyromagnetic ratio of YIG. Since in crystals the effect of the lattice configuration on the orbital magnetic moments is usually to quench them almost completely, the spin-orbit interaction can only slightly alter the spin moment of the lattice [21]. Therefore, γ_e is a good approximation for γ_{YIG}.

Equation 21 gives a symmetrical line shape, but in the actual Lorentzian fitting method, it is important to consider asymmetry, because the coupling between the magnetic sample and the waveguide (or cavity) can partly mix the real and imaginary parts of the susceptibility. The line-shape fit for the FMR absorption data should then have the form:

$$\frac{\Delta H_{HWHM}}{(H - H_{res})^2 + {\Delta H_{HWHM}}^2}\cos\epsilon + \frac{H - H_{res}}{(H - H_{res})^2 + {\Delta H_{HWHM}}^2}\sin\epsilon\ , \tag{25}$$

and for the FMR absorption derivative data:

$$\frac{2(H - H_{res})\Delta H_{HWHM}}{\left[(H - H_{res})^2 + {\Delta H_{HWHM}}^2\right]^2}\cos\epsilon + \frac{{\Delta H_{HWHM}}^2 - (H - H_{res})^2}{\left[(H - H_{res})^2 + {\Delta H_{HWHM}}^2\right]^2}\sin\epsilon\ , \tag{26}$$

where ϵ expresses the mixing between dispersive and absorptive components of the measurement, due to the superposition of secondary modes. The first term of Equation 12 is the symmetrical term. It corresponds to the imaginary part of the susceptibility and thus to the absorbed power of the main mode. For small ϵ, the asymmetry is small. The smaller the asymmetry, the smaller the error associated with the calculated linewidth (ΔH_{HWHM}) and resonance field (H_{res}). When the asymmetry is large, the sample should be repositioned on the waveguide (or in the cavity) and the measurement repeated [95].

It could also be the case that the FMR *spectrum* of a sample exhibits a Gaussian shape instead of Lorentzian, or a blend of the two. A Gaussian-shaped FMR absorption line is usually the indication of polycrystalline-structured material. Different crystalline phases may have different easy-axis orientation and slightly different saturation magnetization. When there are only a few different crystalline phases in a sample, the *spectrum* shows distinct Lorentzian peaks with positions slightly shifted with respect to each other [96].

2. Experimental methods

The core results of this study rest mainly on the measurements of the linewidths and damping performed with field-modulated VNA-FMR. The characterization of the magnetization dynamics of the samples via (both common and field-modulated) VNA-FMR measurements has offered many challenges and demanded special dedication. Accordingly, this method is described in the present Chapter in more detail, as compared to the other experimental methods.

2.1 Vector network analyzer ferromagnetic resonance (VNA-FMR)

The implementation of a broadband technique that can probe the FMR behavior of a sample over a wide range of frequencies was made possible due to the introduction of two key elements: the vector network analyzer (VNA) and the broadband waveguide.

For decades, the most common application of VNAs has been in communications engineering, where it is employed to determine the microwave properties of circuits or to verify the performance of components, like amplifiers, filters, antennas, cables and mixers. Recently, VNA features were proven to be useful for the investigation of magnetization dynamics, since they occur in the microwave range [97].

Before the introduction of the VNA in the FMR experiment, a rf generator, a lock-in amplifier and a rectifier diode would, in combination, be able to give the absorption response of the ferromagnetic sample. The absorption signal of thin films is low because of its reduced volume. This combined with the great amount of noise produced by rf signals in laboratory-dimension circuits would result in low signal-to-noise ratio (SNR), beyond the limit of detection. Thus, a signal processing technique designed to extract low amplitude signals is required. This calls for signal modulation combined with lock-in detection. However, amplitude modulation performed by the rf generator itself results in poor SNR gain. A good alternative is to modulate the dc magnetic field, instead, which can be implemented by auxiliary coils that will add a low-frequency ac field in the same orientation as the dc field. When field modulation is used, the measured FMR signal will be proportional to the field derivative of the absorbed power (Figure 16, right). For this alternative, modulation frequency in the range of 80 Hz – 200 Hz is sufficient to significantly improve the SNR [97] [98] [99] [100].

The VNA has an internal rf source that generates a sinusoidal signal (used as reference). The signal is reflected from the device under test (DUT) and returns to the VNA, where it is detected. The reflected signal arrives at the analyzer through the same port through which the incident signal is sent to the DUT. In case of a 2-port experiment, besides the reflected signal, a

transmitted signal is also detected coming from the output of the DUT, arriving at the analyzer through the second port. The microwave signals must be converted into intermediate frequencies in the range of a few KHz before they are analyzed. To improve the SNR, filtering and amplification are also needed in the process. By comparing phase and amplitude of the reflected, transmitted and reference signals, the VNA can measure the scattering parameters of the DUT and thus calculate the physical parameters of interest in the device [23] [97] [101].

The great advantage of the introduction of the VNA in the FMR experiment is that it can sweep a broad range of microwave frequencies, revealing new features in the dynamic properties of the ferromagnetic sample. By performing this sweep several times, each time using a slightly different intensity H for the dc field applied on the sample, the field is also going to be swept over a specified range, generating a three-dimensional plot of the absorption. For practical reasons, this 3-D plot is usually color-coded into a 2D colormap (Figure 18, left). The dispersion curve characteristic of this measurement is an expression of the resonance condition for the sample, *i.e.*, it indicates for what combinations of frequency (f) and field intensity (H) resonance occurs. One of the advantages of this technique is the determination of the saturation magnetization without the need to know the volume of the sample, by using the Kittel formula (Equation 9) to fit the dispersion curve. The diagram on the right side of Figure 18 describes the VNA-FMR setup assembled in the Laboratory of Applied Magnetism for the characterization of our samples. The VNA model used was a Rohde & Schwarz® ZVA24, which can operate frequencies from 10 MHz to 24 GHz, has a sensitivity of 85 dB, and an output power of up to 18 dBm (63 mW). A Lakeshore® power supply was used to energize the electromagnets and a gaussmeter to control the magnetizing field (Figure 18, right).

As shown in Figure 18 (left), frequency- or field-swept resonance lines can be extracted from the colormap, but when it comes to the accurate determination of linewidths, the SNR may prove too low. Fortunately, derivative-field measurement can also be implemented in the VNA-FMR experiment, enabling more accurate linewidth measurements. For that effect, auxiliary Helmholtz coils powered by an auxiliary Kepko® power supply are added in the setup, as shown in Figure 18, on the right. The absorption line is then obtained by performing a field-swept measurement at a constant frequency. Like in the traditional FMR experiment mentioned above, the derivative-field measurement reduces the noise caused by high-frequency signals and the SNR is thus improved. Alternatively, the field can be made constant, and the resonance line will be built by sweeping the frequency. The noise optimization due to the derivative-field method is also perceived in this frequency-swept mode [98].

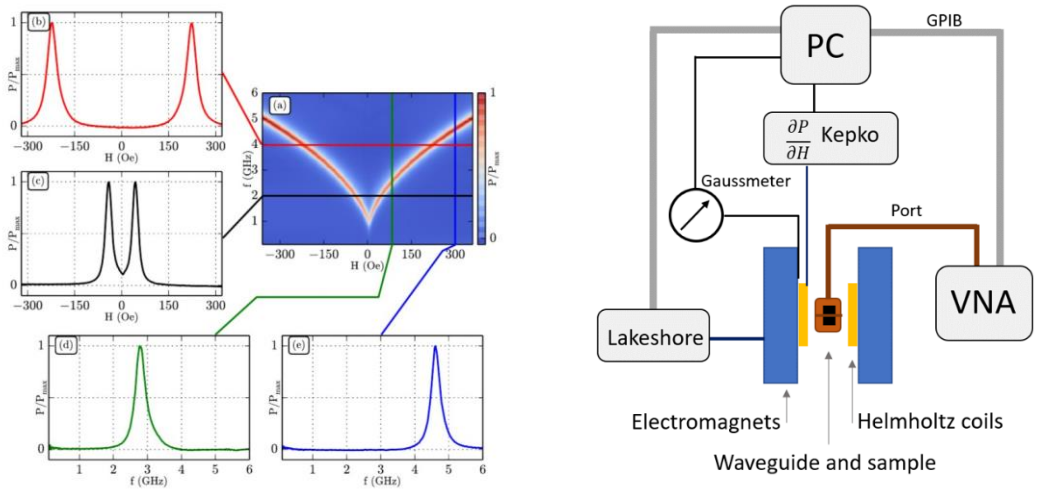

Figure 18: On the right, a diagram of the VNA-FMR setup, with field modulation and one-port waveguide circuit. On the left, an example of the 2D color-coded map of the rf power absorbed by the sample, exhibiting the resonance dispersion curve. As indicated, the colormap contains information on the resonance lines that characterize the sample. The diagram on the left was reproduced from [23].

The intensity of the ac magnetic field used for field modulation must not be greater than the HWHM linewidth of the measured resonance line, or there will be deformation of the resonance line and inaccuracy in the measurement of the linewidth, which will appear to be broader than it truly is. This is called *overmodulation*, and it is critical at lower frequencies, where the linewidth is narrower. Preliminary FMR linewidth measurements should be made at the lowest frequency with varying values for the ac current feeding the modulating coils, and the suitable value of the ac current (for measurements at this and higher frequencies) will be the biggest value before the observation of the apparent broadening of the linewidth [102].

Broadband frequency FMR would not be possible without broadband waveguides. They are used to guide the high-frequency signals to the investigated sample. Due to properties of the electromagnetic waves, they must be carefully designed [97]. In the present work, microstrip waveguides fabricated in the Laboratory of Applied Magnetism (CBPF) were employed.

2.2 Thin-film fabrication

2.2.1 Magnetron sputtering

The deposition of YIG thin films, as well as the subsequent deposition of metallic coating (Ag, Cu, Ni, CoFeB, CoFe and Py) for the fabrication of the structures involved in this project, was made via magnetron sputtering in the Laboratory of Surfaces and Nanostructures (LABSURF), at CBPF.

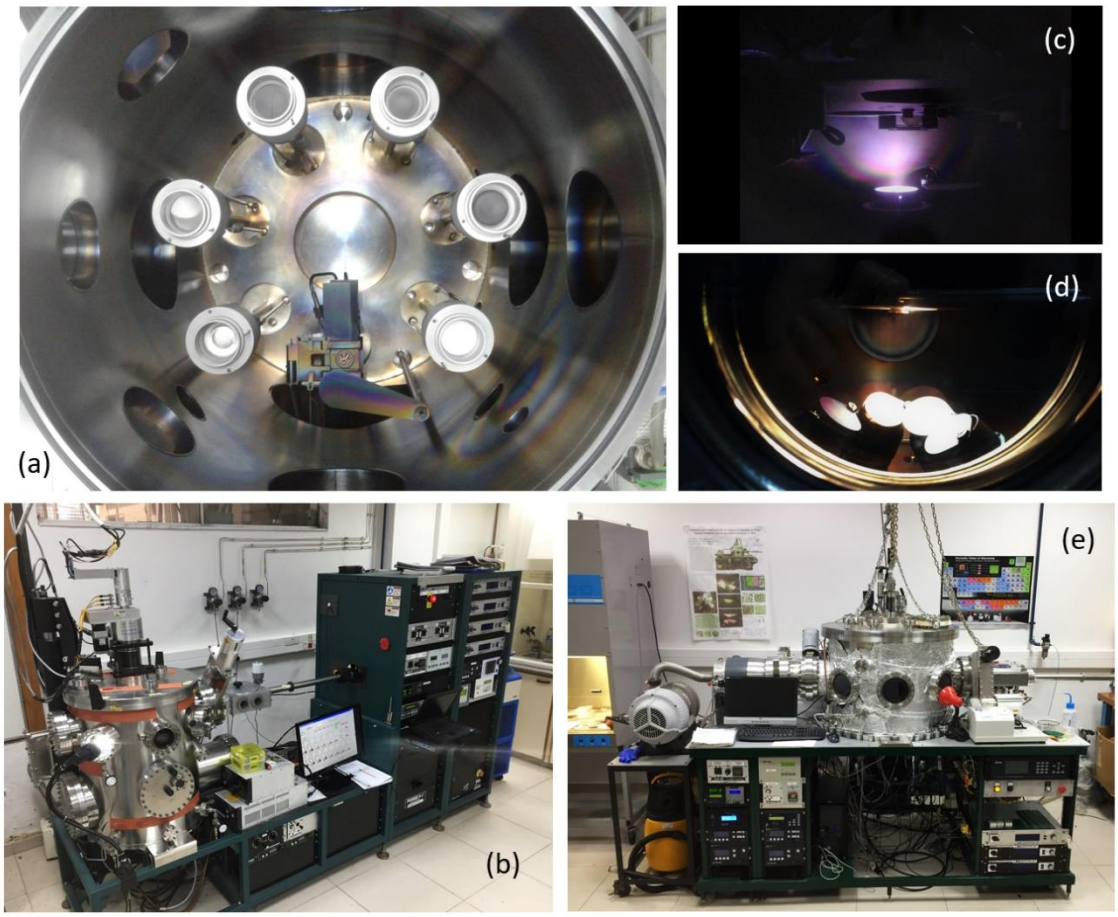

Figure 19: Magnetron sputtering facilities in the Laboratory of Surfaces and Nanostructures, at CBPF. Main chamber, with targets installed in the six guns (a), of the on-axis sputtering system (b); photograph from a window of the main chamber, lit up by plasma (c), during a deposition procedure; photograph from a window of the main chamber (d) of the off-axis sputtering system (e).

LABSURF has two independent magnetron sputtering systems (Figure 19). One is fabricated by Aja International Inc. and has an on-axis configuration, with six installed guns. The other system is home integrated and has an off-axis configuration, with five installed guns (Figure 20). Both systems can have their guns activated by dc or rf power supplies, enabling films to be deposited from conducting and insulating targets. Plasma is ignited and maintained in an atmosphere of argon, with controlled flow. Work pressure can be controlled either nominally or by pre-calibration. In the former case, the controller system will read the pressure sensor in the main chamber and operate the valve of the turbo vacuum pump so that the input work pressure is maintained. In the latter case, for a given argon flow, the operator manually pre-calibrates the valve-aperture value for which the gas in the chamber stabilizes at the desired work pressure.

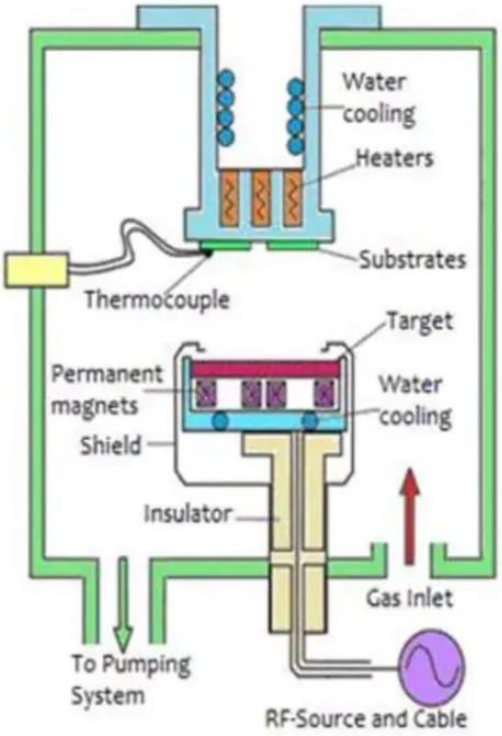

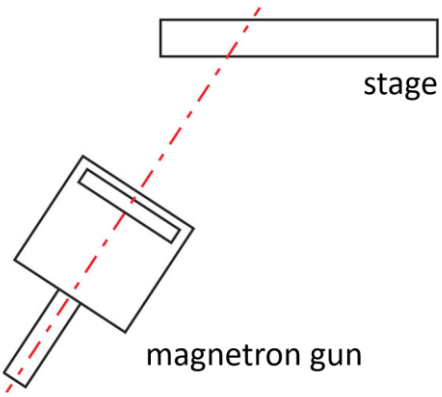

Figure 20: Left: Scheme of an on-axis magnetron sputtering system. Below: In the off-axis configuration, instead of facing the substrate holder directly, there is an angle whereby the beam of particles reaches the deposition stage.

2.2.2 Substrate preparation

Before placing the substrates on the sample holder for sputtering deposition, it is necessary to cut them into the adequate the sizes. Some substrates, like Si (100) can be cleaved along their natural crystallographic lines. Others, like GGG (111) require the use of mechanical cutters. In this study, Si (100), MgO (100) and GGG (111) substrates were used for the deposition of YIG. Careful procedures were adopted for substrate preparation. GGG substrates were protected with a photoresist coating to prevent damage to the substrate surface in the cutting operation. For thorough cleansing, the substrate pieces were submitted to successive baths in acetone (ultrasonic bath), isopropyl alcohol and distilled water. After drying by evaporation in a protected chamber, they were placed in the sputtering chamber for deposition.

2.2.3 Post-annealing

The room-temperature deposition of amorphous YIG films must be followed by post-annealing to achieve crystallization and the desired magnetic properties. To obtain YIG films with surface quality that meets the requirements for spin-pumping experiments, a controlled oxygen atmosphere is used during furnace annealing [92]. We used a Thermo Scientific Lindberg Blue ®

tube furnace and a home-assembled circuit for the controlled atmosphere (Figure 21), which included an oxygen cylinder with 4.0 purity, a flow meter and a high-temperature pyrex tube. The samples were submitted to a single-stage annealing process, as shown in Figure 22. Setpoints 1 and 2 (SP1 And SP2) correspond to the plateau temperature. The annealing plateau time is indicated by the time period 2 (TM2). TM1 and TM3 are adjusted according to the desired ramp-up and ramp-down rates, respectively.

Figure 21: Tube-furnace annealing with controlled atmosphere. The picture on the left shows the flow meter used to measure and control the oxygen flow rate. Above, the front view of the furnace, with the hood lifted to show where the pyrex tube is placed. Below, a set of YIG thin-film samples, before annealing. On the right, the furnace in operation, at 800º C.

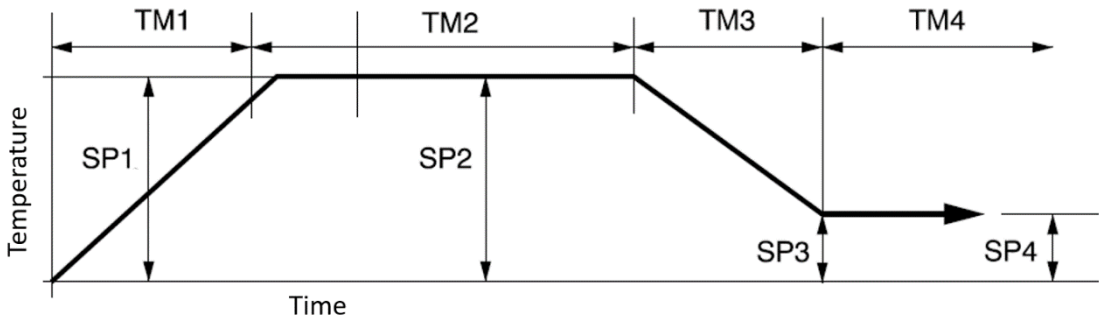

Figure 22: Annealing process represented in a Temperature x Time diagram.
This diagram was reproduced from the Thermo Fisher Scientific Box Furnace Manual.

2.3 X-ray characterization techniques: reflectivity and diffraction

The equipment used for X-ray characterization was the X-Pert Pro, manufactured by Panalytical GmbH, housed at the Laboratory of Crystallography and X-Ray Diffraction, at CBPF. It uses CuKα radiation, with λ = 1.54056 Å. The reflectivity mode (XRR) was used to obtain the thickness of thin films, for sputtering deposition rate calibration. The diffraction mode (XRD) was used to measure diffraction patterns and identify crystallographic phases of post-annealed YIG samples.

2.4 Alternating gradient field magnetometer (AGFM)

This technique is used to obtain the hysteresis curve (M x H) of magnetic samples of reduced dimensions, like 3×3 mm thin-film samples. The equipment was home-assembled at the Laboratory of Applied Magnetism, at CBPF. It has high resolution in magnetic field (0.05 Oe) and operates between -600 and +600 Oe. The dc-field coils provide nearly 20 Oe/A and are powered by a KEPCO bipolar power supply. Excitation of the gradient-field coils and measurement of the response voltage are performed by an SR830 Lock-in amplifier. The sensitivity of the system is on the order of 10^{-7} emu, enabling the measurement of films only a few nanometers thick. Low coercive fields on the order of 1 Oe (which is the case of YIG films) can be measured in this system. Measurements are performed at room temperature.

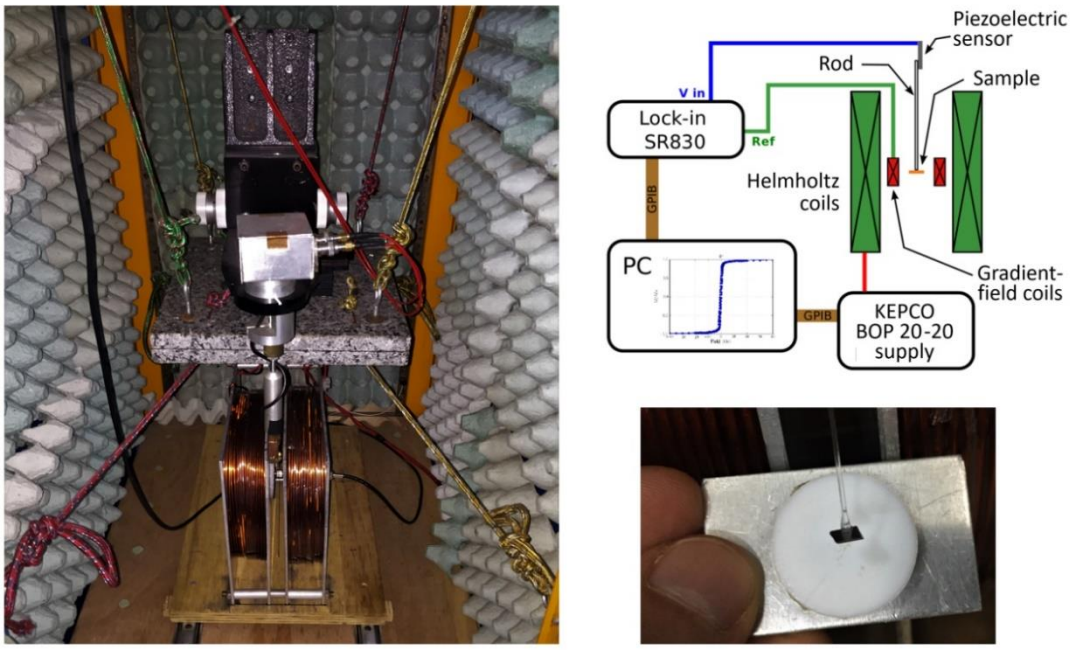

Figure 23: On the left, a picture of the home-assembled AGFM, inside the cabinet where it is protected from acoustic vibrations. Above, a diagram of the AGFM set-up [23]. Below, the picture shows a thin-film sample attached to the tip of the rod.

The physical principle behind this technique is that when a magnetic dipole moment is immersed in a nonuniform magnetic field, there will be a force acting on the magnetic moment. This force is proportional to the magnetic field gradient and to the magnetic moment itself. Figure 23 describes the AGFM. The drawback of this technique is that it does not measure the absolute value of the magnetization. The vertical axis of the $M \times H$ curve is scaled in arbitrary units and the value of the saturation magnetization (M_S) remains unknown.

2.5 Vibrating sample magnetometer (VSM)

This is another technique to measure the $M \times H$ curve, like AGFM, except that it gives the absolute value of the magnetization of the sample. The Quantum Design PPMS® DynaCool™ equipment (Figure 24) installed in the Laboratory of Applied Magnetism has a Vibrating Sample Magnetometry (VSM) mode. The physical principle behind this technique is that the vibrating motion of a magnetic dipole moment creates an oscillating magnetic field. The VSM has pickup coils that sense the magnetic field oscillation created by the sample's magnetization when it is vibrated. The system operates between magnetic fields ($\vec{H}$) of ± 300 Oe, supplied by Helmholtz coils with a resolution of approximately 0.05 Oe. The sensitivity of the VSM is of the order of 10^{-5} emu. Noise levels of less than 6×10^{-7} emu at 300 K are achieved using a lock-in measurement technique to isolate the sample signal from external mechanical and electronic noise. Once the hysteresis is measured, it is necessary to know the volume of magnetic material in the sample to calculate its saturation magnetization H_s.

Figure 24: DynaCool™ equipment, by Quantum Design Inc. The cabinet provides a temperature-controlled, low-vibration environment for accurate sample measurements. The magnetic field and other measurement parameters can be controlled from external programs. The schemes on the right were adapted from the Quantum Design® website, and show the upper and lower pickup coils, the vibration axis, and the external magnetic field $\vec{H}$, which is generated by currents in a superconductor (not depicted).

2.6 Atomic force microscopy (AFM)

Surface characterization of the fabricated YIG thin films was performed at CBPF, using a Bruker® Multimode 8 Atomic Force Microscope (**Error! Reference source not found.**), which provides nanometer surface topographic imaging. This is an essential part of the characterization of YIG films, because surface quality strongly influences the spin conductivity across the interface between the YIG layer and the adjacent metallic layer.

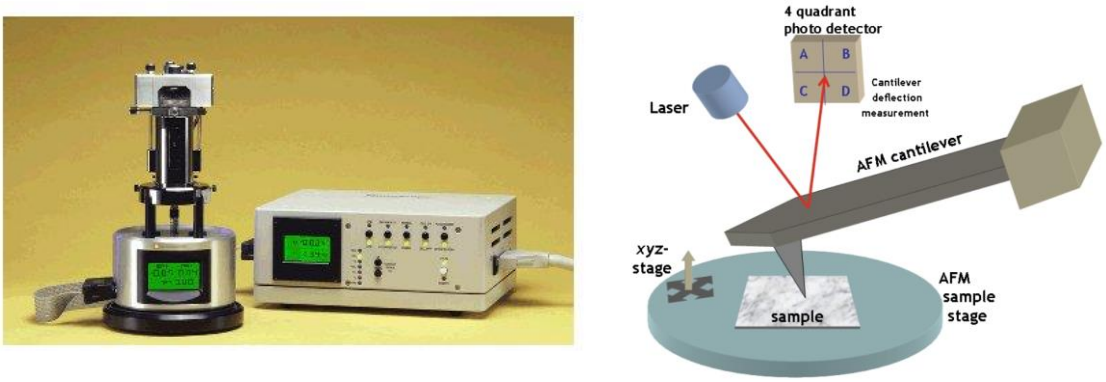

Figure 25: Bruker's Multimode 8 Atomic Force Microscope ™, which performs measurements in contact and tapping imaging modes. On the right, a diagram of the measurement mechanism. The deflection of a microfabricated cantilever is measured by reflecting a laser beam off the backside of the cantilever, while it is scanning over the surface of the sample (The Opensource Handbook of Nanoscience and Nanotechnology).

In contact mode, the cantilever is pressed into the sample until it deflects to a specified set point. While this is the most traditional imaging mode and allows acquisition of mechanical information (*i.e.*, force-distance curves), the constant contact with the sample can be destructive for some materials. Tapping mode minimizes sample damage by contacting the sample only periodically, while providing additional chemical information about the surface. The tip is oscillated near its resonance frequency, and then brought near the surface. As the tip approaches the surface, the amplitude/oscillation is dampened by enhanced sample-tip interactions. An amplitude setpoint is specified, and the sample moved up and down to maintain a constant amplitude.

The roughness of YIG thin-film surfaces can be calculated from AFM topographic imaging. There are different conventions to measure roughness. Profile roughness parameters are those based on the roughness profile over a representative line, chosen on the surface area. The most common roughness profile parameters are the arithmetical mean deviation and the root mean square of the assessed profile, respectively denoted by R_a and R_q (or rms roughness). Area roughness parameters (*e.g.*, S_a and S_q) give more significant values but they are not so common. The parameter adopted in this study is R_a.

2.7 Inverse spin Hall voltage

The experimental setup to measure the ISHE voltage consisted in placing on the metallic surface of the sample two contact probes connected to a nanovoltmeter, while driving the YIG layer to FMR. The obtained voltage (V_{sc}) was then divided by the electric resistance offered by the sample between the two probes to obtain the charge current (I_{sc}) converted from spin current. For correct measurement (Figure 26), this experiment must observe the spin-Hall geometry [10], given by the following expression [58], which is the exact reproduction of Equation 18. This equation describes the conversion of spin current ($\vec{J}_s$) into charge current ($\vec{J}_c$) via spin-orbit coupling:

$$\vec{J}_c = \theta_{SH} \frac{(-2e)}{\hbar} \vec{J}_s \times \hat{\sigma} \,. \tag{27}$$

where θ_{SH} is the spin Hall angle, characteristic of the material, and $\hat{\sigma}$ is the spin-polarization unit vector of the spin current. Like in Equation 11, the minus sign in the parentheses cancels out because the value of the electron charge (e) is negative.

We have chosen the notation V_{sc} to designate the voltage originated in spin-to-charge current conversion, because other effects, like IREE and ASHE, which observe the same geometry, can contribute to this conversion along with ISHE (as discussed in Section 1.5.3).

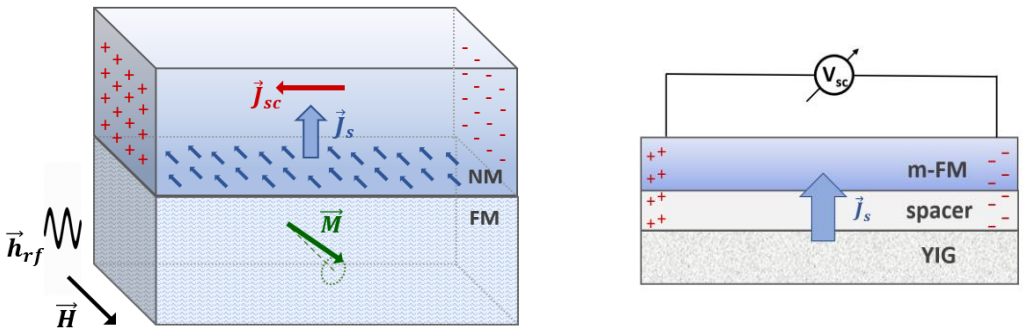

Figure 26: The diagram on the left represents the dynamics of spin pumping and ISHE in a FM/NM structure, where the NM has strong SOC and a positive spin Hall angle ($\theta_{SH} > 0$). The small arrows represent the polarization $\hat{\sigma}$ of the spins accumulated at the interface. The spin-Hall geometry reflects the relation described in Equation 27. On the right, detection of the spin-to-charge current conversion in a trilayer structure where YIG, the spin injector, is separated from the spin sink by a metallic spacer.

3. Results and discussion

3.1 Fabrication of YIG thin films

The first mission in this project was to establish a safe route for the fabrication of YIG thin films with crystallographic and magnetic qualities that meet the requirements for experimental spintronic investigations. All depositions were made via magnetron sputtering, using 2-inch YIG targets, and followed by post-annealing. Target-to-substrate distance was maintained at 7.7 cm for the on-axis configuration. Substrate rotation was set to 80 rpm for the off-axis deposition, with an incident angle of approximately 40º and a target-to-substrate distance of approximately 12 cm. In a preliminary stage, we used nonconventional substrates: MgO (100), Si (100) and Si/SiO_2 (100). Subsequently, GGG (111) substrates were used. First, deposition and post-annealing parameters were calibrated with crystallographic- and magnetic-quality evaluations obtained from XRD patterns, AGFM hysteresis curves, VNA-FMR colormaps and $\Delta H \times f$ linear fits of YIG thin-films post-annealed in air. After this calibration, controlled oxygen atmosphere was introduced in the annealing procedure, and surface quality was evaluated via AFM characterization.

3.1.1 On nonconventional substrates

Although Si (100), Si/SiO_2 (100) and MgO (100) substrates have not been proved to support the fabrication of YIG thin films with the magnetic properties required for spin pumping experiments, they offer the possibility of device integration with electronic and optical components. We fabricated a total of 63 YIG samples using these nonconventional substrates, via on- and off-axis magnetron sputtering. Base pressure was on the order of 10^{-7} to 10^{-6} Torr. RF power was set to 75 W for the on-axis and to 150 W for the off-axis system. The argon flow was set to 15 sccm and the work pressure was varied in the range of 5 to 40 mTorr.

First, we used the off-axis system to fabricate samples with the same work pressure (10 mTorr), and annealed them for different periods of time. The plateau was set to 750º C, with 2º C/min ramp up and 1º C/min ramp down. The XRD patterns of the YIG films deposited on MgO and Si/SiO_2 substrates show that the as-deposited films on both substrates grow into polycrystalline YIG, with no prevalent crystal orientation (Figure 27). The results show little difference for plateau varying from 1 to 8 hours, indicating fast crystallization process. It is possible to observe in the XRD patterns of the samples deposited on MgO (Figure 27, left) a small

peak to de right of the (420) peak, which becomes more pronounced with annealing duration, indicating a growing parasitic $FeYO_3$ phase [103]. For the samples deposited on Si/SiO_2, AGFM magnetization curves revealed virtually unchanged coercivity (between 24 and 25 Oe) for the different annealing durations, while the coercivity of the samples deposited on MgO presented highest coercivity (27 Oe) when annealed for 2 hours and lowest (22 Oe) when annealed for 8 hours (Figure 28).

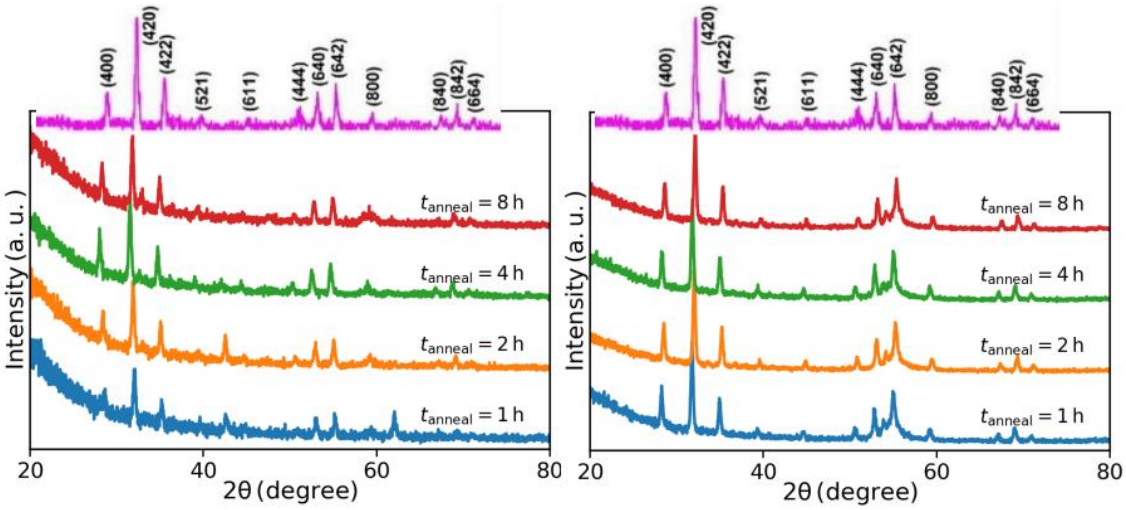

Figure 27: XRD analysis of 75-nm thick YIG films deposited on MgO (left) and Si/SiO2 substrates (right). The samples were deposited using off-axis configuration, argon flow of 15 sccm and work pressure of 10 mTorr. The annealing duration of the plateau (750^{o} C) varied from 1 to 8 hours, as indicated. The diffraction pattern (of polycrystalline bulk YIG) in magenta serves as a reference. It is indexed with the orientation of each peak and is a reproduction from Ref. [104].

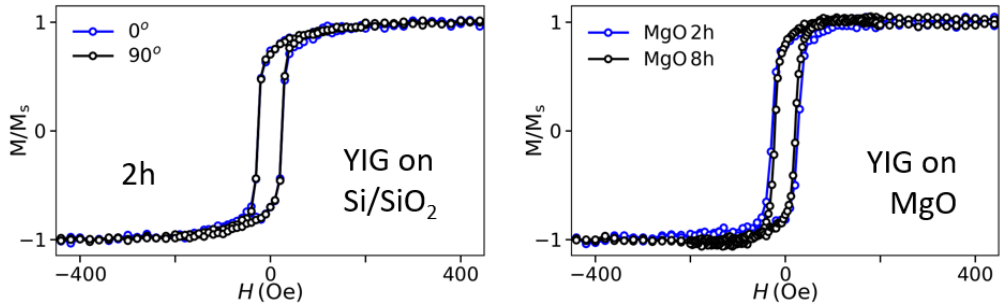

Figure 28: Normalized AGFM magnetization curves. On the left, YIG on Si/SiO2 post-annealed for 2 hours. On the right, the graph compares two samples of YIG on MgO with different post-annealing durations.

More samples were then fabricated on Si, Si/SiO2 and MgO substrates, both with the on- and off-axis sputtering configurations. This time, the work pressure was different in each deposition, and all samples were post-annealed with a 4-hour plateau. For all YIG films deposited on MgO or Si/SiO_2, the colormaps showed weak signal response and thick dispersion lines (see examples in Figure 29), indicating deficient crystallization. However, a remarkable result (Figure 30) was obtained for a film deposited on MgO (off-axis, 15 sccm, 20 mTorr), which exhibited a

coercive field of 18 Oe. (Cf. Ref. [105], where a coercive field of 20 Oe is reported for a YIG thin film deposited on MgO substrate.) The graphs in Figure 28 (left) and Figure 30 confirm, by comparing two magnetization curves measured with perpendicular in-plane orientations, that the expected in-plane anisotropy of YIG thin films is isotropic in the plane of the film.

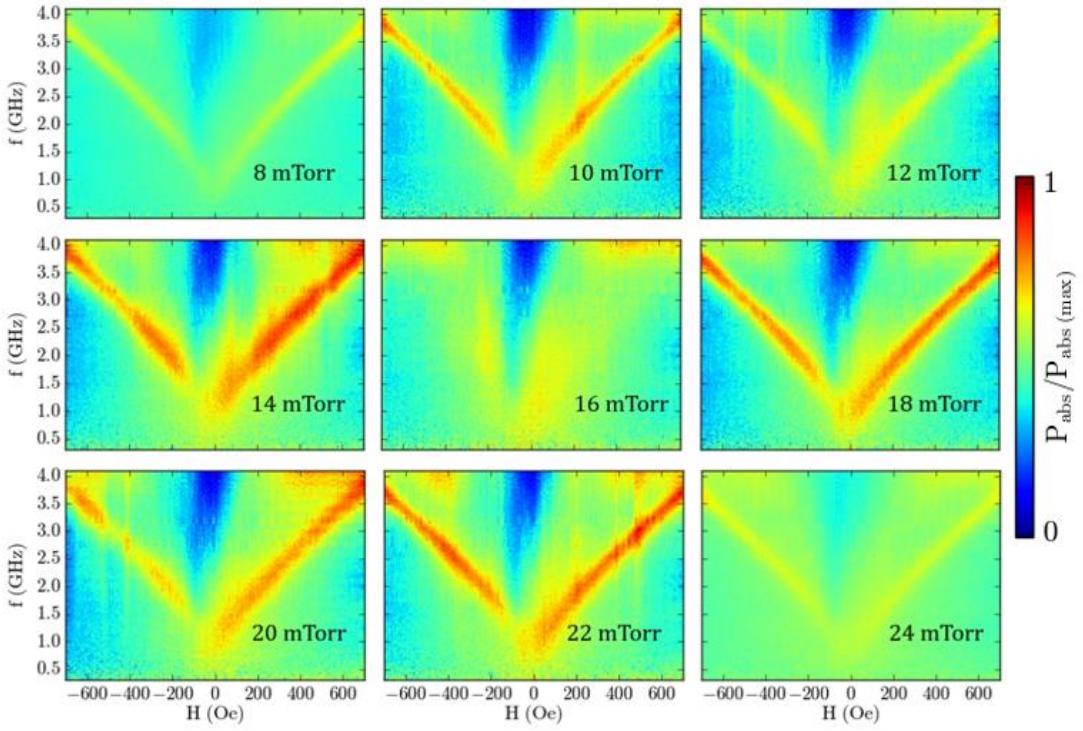

Figure 29: VNA-FMR colormaps of YIG samples deposited on MgO (100) substrates, with on-axis configuration and varying work pressures, and post-annealed at 800^0 C for 4 hours.

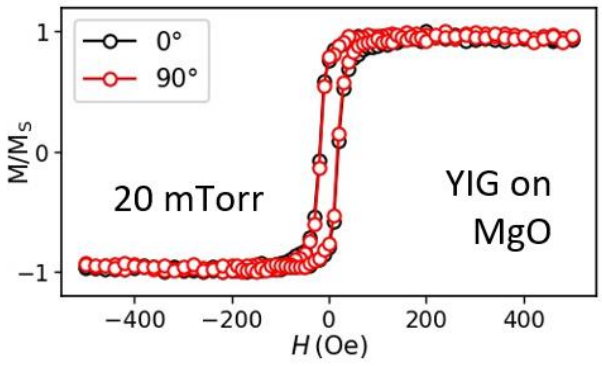

Figure 30: Normalized AGFM magnetization curve of the YIG thin film deposited (off axis) on MgO with 20 mTorr work pressure. The coercive field is 18 Oe.

From the above-mentioned set of thin-film samples deposited with varying work pressures, the ones deposited on Si substrates without the thermally oxidized layer exhibited results similar to the ones deposited on Si/SiO_2 and MgO, except for one, which exhibited a much better VNA-

FMR pattern, with a well-defined dispersion curve (Figure 31). The deposition of this sample was performed at the lowest work pressure (5 mTorr) that would still maintain a stable YIG plasma in the off-axis sputtering system, with argon flow of 15 sccm. The quality of the signal exhibited by the AGFM hysteresis measurement for this sample and the low coercivity of 13 Oe confirm the high magnetic quality of the YIG film, as compared to the other samples on nonconventional substrates.

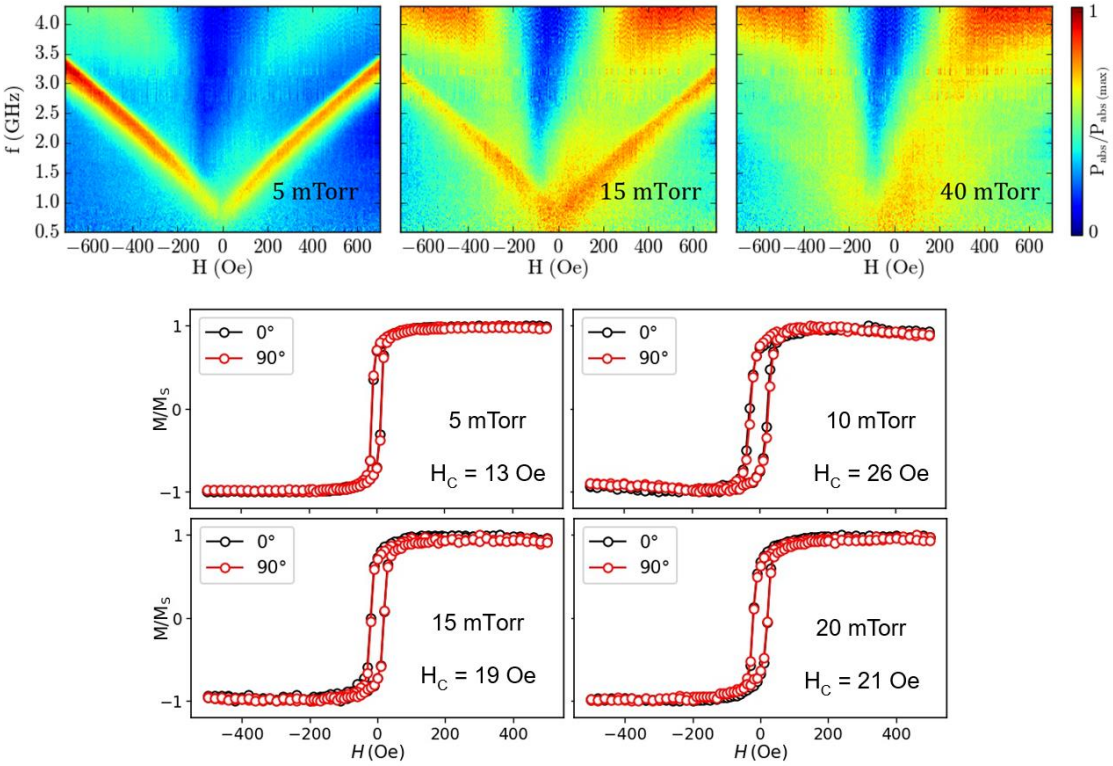

Figure 31: VNA-FMR colormaps and AGFM hysteresis curves of YIG samples deposited on Si (100) substrates, with off-axis configuration and varying work pressures, and post-annealed at 750º C for 2 hours.

3.1.2 On GGG (111) substrates

Prior to deposition, the GGG (111) substrates, with original dimensions 10×10×0.5 mm, were protected with a photoresist coating and mechanically cut into 3×3 mm pieces. Samples were fabricated via on- and off-axis magnetron sputtering (with rf power of 75 W and 150 W, respectively), with different work pressures. The argon flow was maintained at 15 sccm, except when otherwise stated. All the samples were post-annealed for 4 hours at 800º C. The off-axis configuration presented irregular results. The colormaps in Figure 32 show contrasting results for the linewidths (which can be evaluated from the width of the dispersion curves) and for the sharpness of the signal. It can be inferred from these results that the crystallization of these YIG thin films was extremely sensitive to the deposition parameters. These results indicated that the off-axis configuration did not promote the achievement of monocrystalline YIG thin films.

The instability in the colomap results disappeared with adoption of the on-axis deposition. Using work pressures in the range of 8 to 24 mTorr, all films exhibited sharp signal and sharp dispersion curves on the VNA-FMR colormaps (Figure 33). This indicates that, in contrast to the nonconventional ones, the use of GGG (111) substrates made possible the fabrication of YIG thin films with an aligned crystallographic orientation, and a reduced number of crystallographic phases. So now we investigate these samples in more detail.

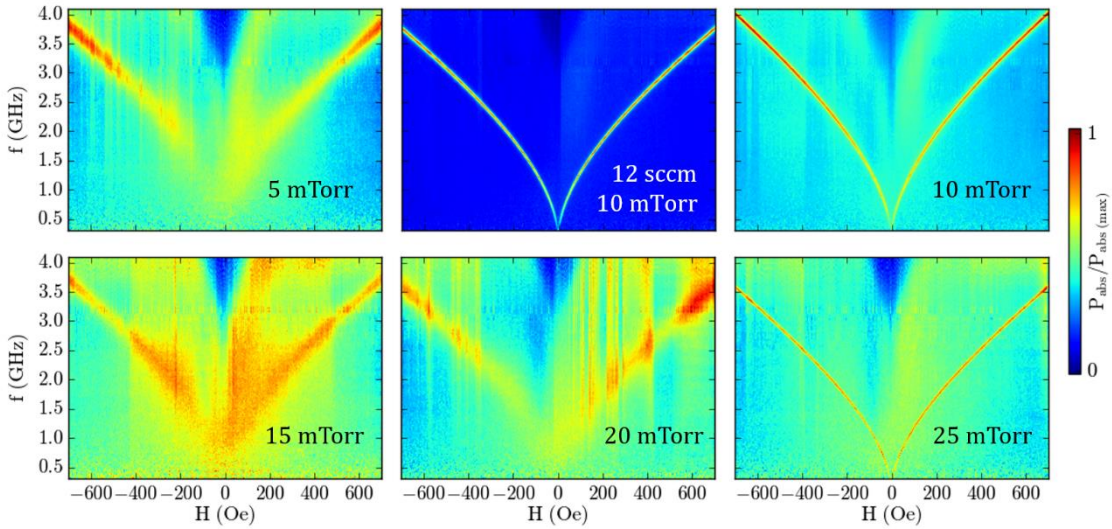

Figure 32: Comparing VNA-FMR colormaps of YIG samples deposited on GGG (111) substrates, with off-axis configuration and varying work pressures. Argon flow was adjusted to 15 sccm for all depositions, except the one indicated. All samples were post-annealed at 800^{o} C for 4 hours.

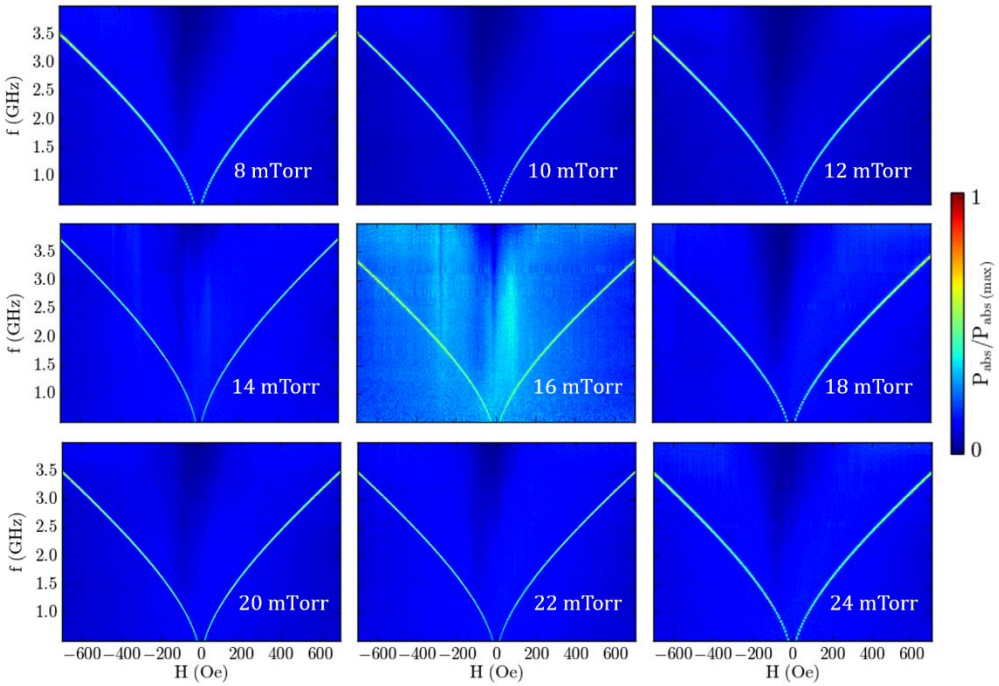

Figure 33: VNA-FMR colormaps of YIG thin films deposited with different work pressures. All films were deposited on GGG (111) substrates via on-axis magnetron sputtering, with argon flow adjusted to 15 sccm, and post-annealed at 800^{o} C for 4 hours.

So far, the VNA-FMR measurements have been performed with the waveguide placed inside a long spiraled magnetic coil and connected to the VNA in a two-port circuit. The magnetic coil could only generate a limited intensity of magnetic field (700 Oe, as reflected on all the colormaps presented so far). At this point of our experimental research, the magnetic coil was replaced by a more robust electromagnet to broaden the range of applied-field intensities. Auxiliary Helmholtz coils connected to a lock-in amplifier were included in the setup to enable the field-modulated measurement of resonance lines (Figure 34, right) and the use of a one-port circuit with a microstrip waveguide was adopted. This new setup is depicted on the diagram on the right side of Figure 18. The broadening of the range of applied-field intensities (up to 3,000 Oe) permitted the measurement of YIG resonances at higher frequencies, further exploring (up to 10 GHz) the broadband frequency range of the VNA (Figure 34, left).

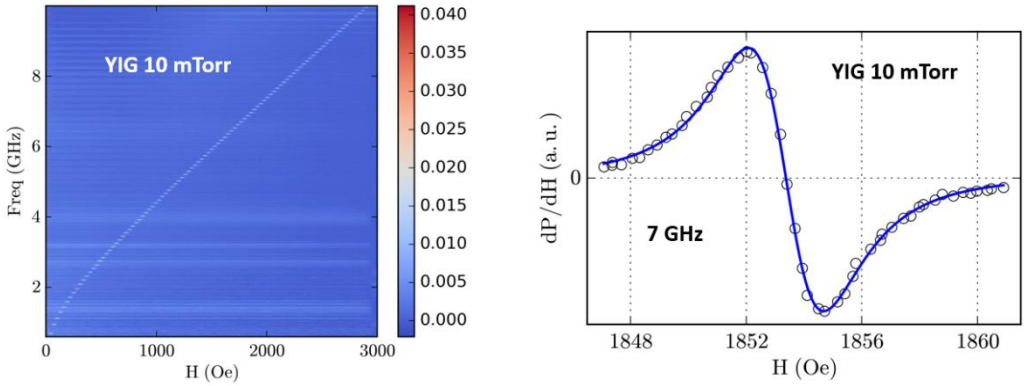

Figure 34: On the left, an example of a color-coded VNA-FMR broadband measurement. In this case, the measured sample is the YIG thin film deposited on GGG with working pressure of 10 mTorr. (Cf. Figure 33.) On the right, an example of field-modulated resonance-line measurement. The measurement was performed with the same sample and a fixed frequency of 7 GHz. The Lorentzian fit (blue line) to the experimental data (black circles) indicated a HWHM linewidth equal to 2.3 Oe.

With the assigned sample placed on the broadband waveguide, repeated field-modulated measurements of the resonance line followed by Lorentz fitting allowed us to plot the linewidth dependence on a broad range of frequencies. The linear fit to this plot, combined with Equation 24, as detailed in Section 1.7, gave the damping (α) and the homogeneous line broadening (ΔH_0) of the sample. Figure 35 shows the linewidth dependence on frequency for eight of the nine YIG thin films of Figure 33. The Kittel formula (Equation 9) was used to fit the dispersion curve (Figure 36) of each sample and calculate its effective saturation magnetization ($4\pi M_{eff}$). These results are summarized in Table 2. We don't recognize in any of the three magnetic parameters (α, ΔH_0 or $4\pi M_{eff}$) a work-pressure dependence strong enough to be recognizable in our data. The variations observed reflect variations in the conditions of substrate preparation, sputtering deposition and annealing that cannot be controlled with the instrumentation available.

Nonetheless, these results show that we can fabricate YIG thin films with magnetic quality comparable to results reported by other groups in the literature for YIG thin films used in spin-pumping experiments [96] [80].

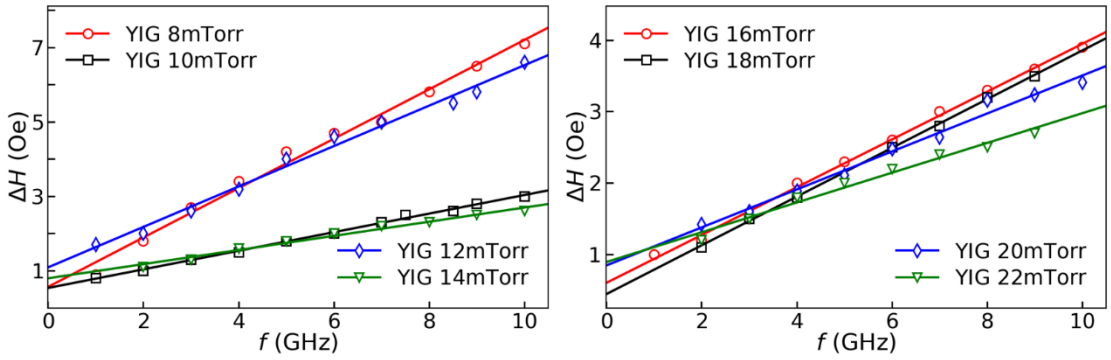

Figure 35: Linewidth dependence on frequency of YIG thin films deposited with different work pressures. (Cf. Figure 33.) The linear fits for the eight samples were plotted in two separate graphs to improve clarity.

Figure 36: Example of saturation magnetization calculated from the VNA-FMR dispersion curve, where the dashed red line is a fitting curve modelled by the Kittel formula.

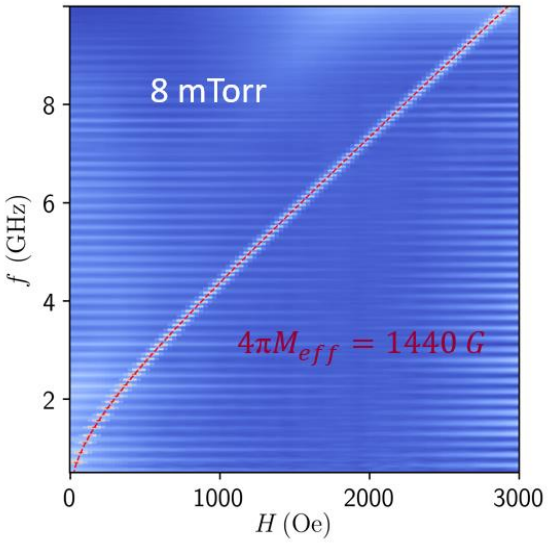

Work pressure	α (10^{-4})	ΔH_0 (Oe)	$4\pi M_{eff}$ (10^3 Gauss)
8 mTorr	18.6	0.56 ± 0.14	1.44
10 mTorr	7.0 ± 0.6	0.53 ± 0.03	1.46
12 mTorr	15.4 ± 0.4	1.06 ± 0.09	1.40
14 mTorr	5.3 ± 0.2	0.79 ± 0.06	1.78
16 mTorr	9.4 ± 0.2	0.60 ± 0.04	1.22
18 mTorr	9.6 ± 0.1	0.44 ± 0.03	1.37
20 mTorr	7.4 ± 0.3	0.84 ± 0.08	1.45
22 mTorr	5.8 ± 0.3	0.89 ± 0.07	1.45

Table 2: Magnetic parameters for the YIG thin films deposited on GGG (111) with on-axis configuration; damping (α), inhomogeneous line broadening (ΔH_0), and saturation magnetization ($4\pi M_{eff}$, where three significant figures are displayed, and error is implicit). Cf. Figure 33.

It is important to mention here the possible contribution of two-magnon scattering to the linewidth. Because this contribution is nonlinear in the wide spectrum, the damping measurements of our samples could be distorted in an unobserved way if two-magnon scattering participated with relevance in the magnetic relaxation. (See Section 1.4.) But the curve that would describe the frequency dependence of the two-magnon contribution to the linewidth, as calculated for our samples from the model offered by Ref. [30], exhibits clear nonlinearity in the frequency range used in our study of the damping (Figure 37). Considering that our samples showed linear behavior, this suggests that an eventual participation of two-magnon scattering is not relevant in our measurements, which we henceforth assume.

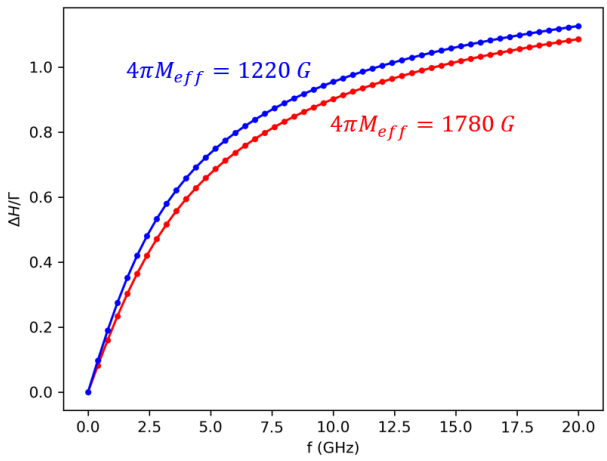

Figure 37: The diagram depicts the sin^{-1} term of Equation 10, using the lowest and the highest effective saturation magnetizations found for the samples described in Table 2.

The XRD analysis in Figure 38 (left) confirms the relation between the magnetic and crystalline qualities of a YIG sample. While amorphous YIG thin films deposited on nonconventional substrates became polycrystalline upon annealing, presenting multitudinous

crystallographic YIG phases with widely distributed orientations (Figure 27), the sample described in Figure 38 (left), deposited on a GGG (111) substrate, exhibits only one YIG phase, with <111> crystallographic orientation. The large thickness difference between the YIG film (55 nm) and the GGG substrate (500 nm), results in magnified GGG peaks on the XRD pattern. Because both thin film and substrate have the same crystal structure and the same crystallographic orientation, the YIG peaks are difficult to distinguish from the GGG peaks in the XRD spectrum. In the wide-scan XRD pattern, they are indistinguishable. Figure 38 (left) shows the XRD pattern amplified in the horizontal axis and focused on the GGG (444) peak. The small difference in lattice constants of YIG (12.376Å) and GGG (12.383Å) causes a slight shift in the localization of their (444) peaks, thus evidencing the presence of the YIG (111) phase [106]. The split peaks in the GGG (444) pattern are attributed to $K\alpha_1$ and $K\alpha_2$ lines of the incident X-ray [107]. The VSM analysis (Figure 38, right) shows a coercive field of approximately 0.4 Oe. (Ref. [81] reports coercivity of 0.35 for a 20-nm thick YIG thin film.) The saturation magnetization ($4\pi M_{eff}$), inferred from this analysis and the YIG volume in the sample, is approximately 1460 G.

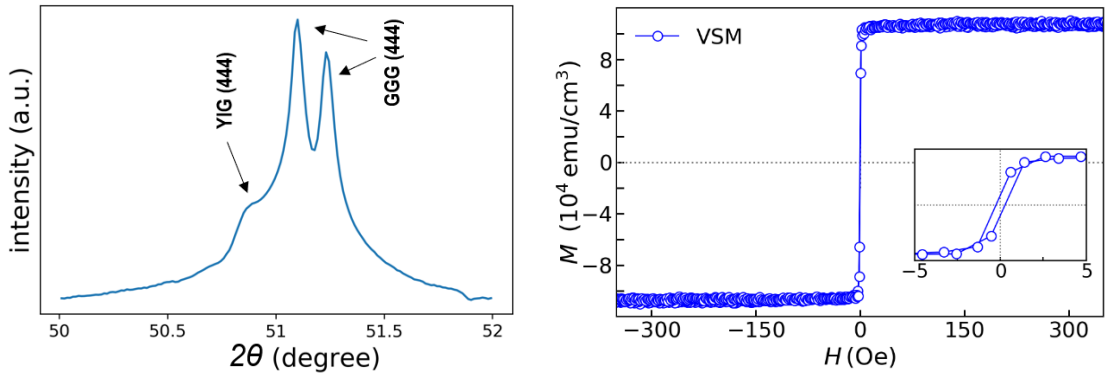

Figure 38: XRD analysis (left) and VSM hysteresis (right) of a 55-nm thick YIG thin film deposited on GGG (111) with on-axis configuration, 15 sccm argon flow, 12 mTorr work pressure, and post-annealed at 800⁰ C for 4 hours.

In the next section, we will show that adverse fabrication conditions can lead to stoichiometry imbalance and parasitic phases, even when GGG (111) substrates are used.

3.1.3 Surface characterization of YIG thin films

The surface of a thin film interacts with the atmosphere, and when this thin film is submitted to annealing, this interaction is potentialized, becoming especially relevant for the quality of the surface. In the case of an oxide with such a complex crystalline structure like YIG, annealing parameters, like plateau temperature and duration, affect not only the overall thin-film quality but also surface characteristics. The environment (either air or a controlled atmosphere, where a

specific gas is employed in a determined pressure) in which the annealing is performed may play a fundamental role. If we are going to use YIG thin films for spin pumping experiments, we must make sure that the crystal and magnetic qualities successfully achieved for the film are not degenerated on the surface and that its roughness is on the order of 0.1 nm.

We tried two post-annealing processes with controlled atmosphere of O_2 (see Section 2.2.3) using different O_2 flow, namely, 70 ml/min and 100 ml/min, on as-deposited YIG thin films for which work pressure of 12 mTorr was used. This is the beginning of a series of fabrication batches, so we are going to call these films YIG1 and YIG2, respectively. Most of the samples belonging to these batches were further processed to obtain metallized YIG thin films, as described in Section 3.1.4. Figure 39 shows the AFM analyses for YIG1 and YIG2, which exhibit an excellent result for the 70 ml/min O_2 flow, as expected from the study reported in Ref. [108]. The R_a values for YIG1 and YIG2 thin-film surfaces are 0.1 and 3 nm, respectively. On the surface of YIG2 the occurrence of pin-holes can be noted. The excellent quality of the YIG1 sample is confirmed by its Gilbert damping coefficient, approximately 7.2×10^{-4}. (See section 3.2.1.)

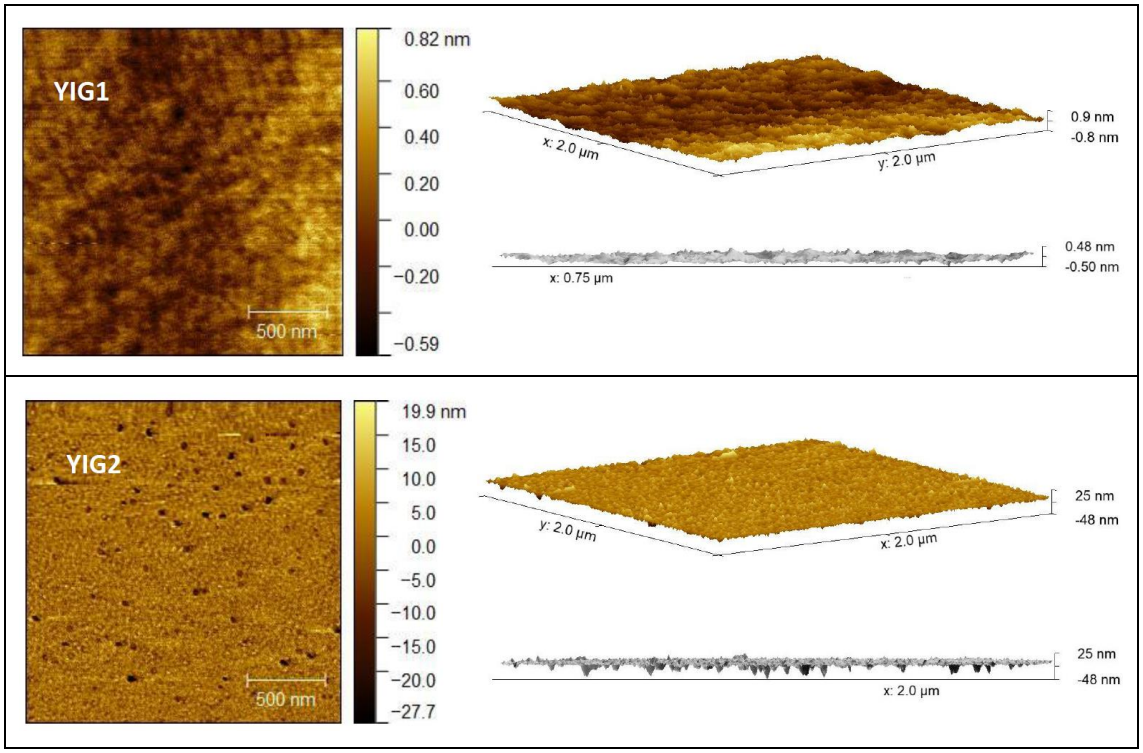

Figure 39: AFM surface characterization of 50-nm thick YIG thin films deposited on GGG with 75-W rf power / 12-mTorr work pressure / 15-sccm argon flow, and post-annealed at 800° C for 4 hours in controlled atmosphere of O_2. Oxygen flow was 70 ml/min for YIG1, and 100 ml/min for YIG2.

Fabrication adversity

During this study, we endured adverse fabrication conditions that challenged the reproducibility of the good results already achieved. VNA-FMR measurements for YIG thin films fabricated on the same route as YIG1 showed insufficient power absorption signal, an indication that the YIG crystallization was flawed. For the next fabrication procedures, we redoubled the attention on substrate preparation. As the sputtering ensemble had been partially disassembled for a cleansing procedure, we tried different deposition parameters. Different annealing parameters were also tried. We eventually discovered that the YIG targets that we were using had both been deteriorated, and we replaced them for a new one. While investigating the cause of the failed attempts in reproducing the results obtained for YIG1, we gained some insight on the combined effect of work pressure and argon flow on the surface characteristics of post-annealed YIG thin films, which we communicate here.

We are going to call YIG R1, YIG R2, and so on, the samples that are part of these efforts to reproduce the results obtained for YIG1. The first two samples of this set were fabricated with the exact deposition and post-annealing parameters as YIG1, with time intervals of two months in between. YIG R3 was also fabricated with the same parameters, except that no vacuum optimization was made after placing the substrate in the main chamber, before deposition. (This was done deliberately, to check possible contamination in the main chamber.) The water used for substrate cleansing before the deposition of YIG R4 was distilled in another laboratory to check possible contamination in the water. The VNA-FMR measurements continued to indicate deficient or defective YIG crystallization. The AFM analyses for these four samples are in Figure 40. The surfaces exhibit islands with different areas and heights. The shapes of the islands are peculiarly distinct, indicating the crystallization of phases different from YIG. Many of the islands have the shape of a regular triangle. (This is most evident in the YIG R3 sample.) Parasitic phases reported to form in defective crystallization of YIG (usually due to stoichiometric imbalance) include iron oxide (Fe_2O_3), yttrium oxide (Y_2O_3) and $FeYO_3$ [103] [109]. The triangular islands can be explained by the presence of the $FeYO_3$ phase, which has a perovskite crystalline structure. As shown in Figure 41, this structure is characterized by a regular octahedron inserted in a cubic unit cell, which supports the formation of pyramidal islands with triangular base. Therefore, there is evidence of the presence of parasitic phases and stoichiometric imbalance.

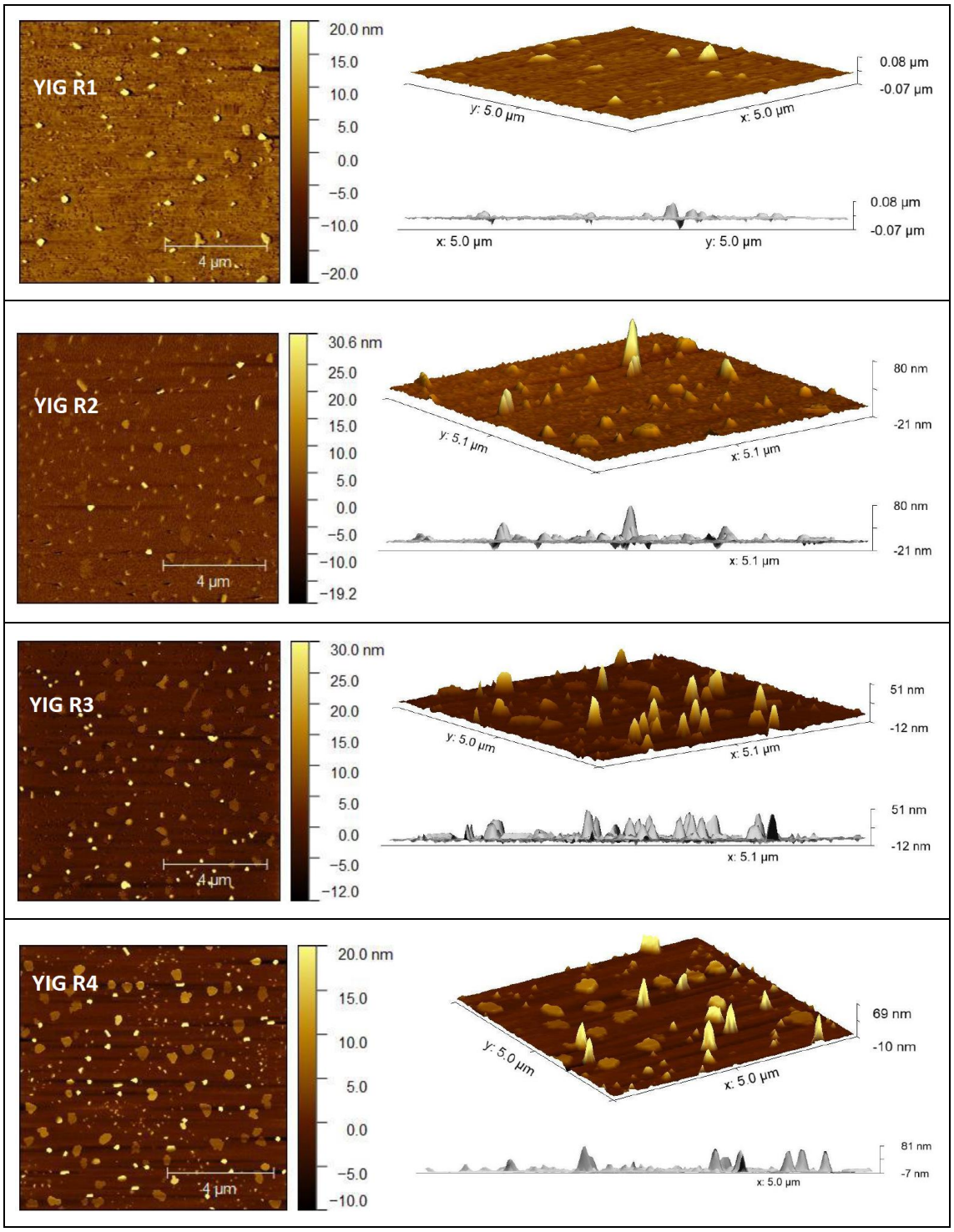

Figure 40: AFM surface analyses for the investigation of fabrication adversities. The four YIG thin films were fabricated with the same deposition and post-annealing parameters as YIG1, after using different substrate preparation procedures.

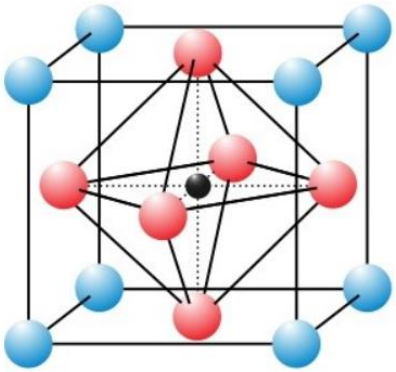

Figure 41: Diagram of the perovskite crystal structure. Picture shared under Creative Commons.

For the next series of samples, deposition parameters were varied. Work pressure of 8 mTorr was used (instead of 12 mTorr) for YIG R5; argon flow of 8 sccm (instead of 15 sccm) was used for YIG R6, while YIG R7 was deposited with 8-sccm argon flow and 18-mTorr work pressure. As shown in Figure 42, a reduction in argon flow combined with an increase in work pressure resulted in a drastic reduction in the incidence of islands. On areas free of islands, the surface of sample YIG R7 exhibited R_a roughness of 0.1 nm.

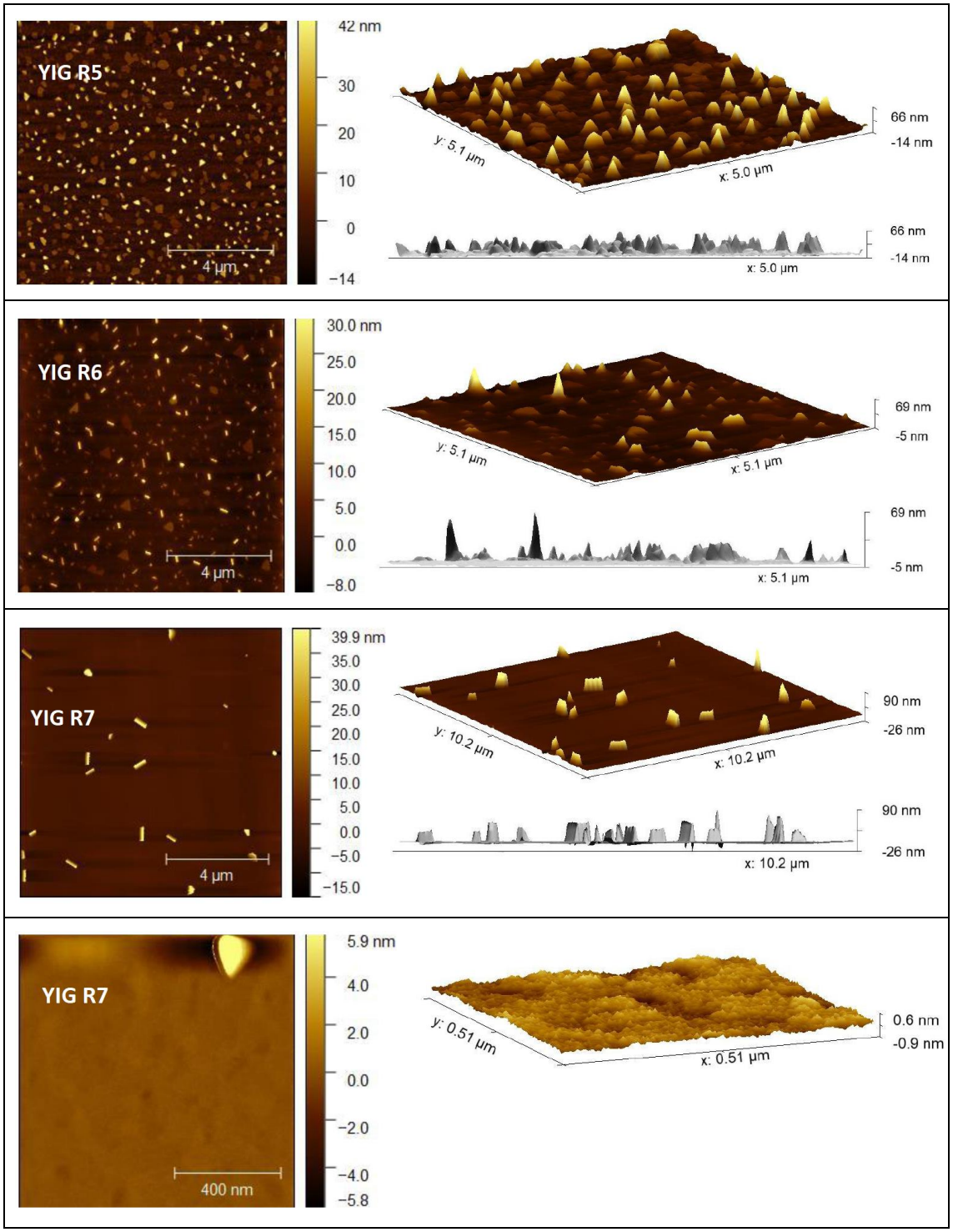

Figure 42: AFM surface analyses for the investigation of fabrication adversities. The three YIG thin films were deposited with different deposition parameters and same substrate preparation and post-annealing processes.

By further reducing the argon flow (5 sccm) and increasing the work pressure (25 mTorr), the occurrence of islands ceased and we obtained 0.4 nm for the R_a surface roughness of sample YIG R8 (Figure 43). The AFM analysis of the as-deposited YIG thin film exhibits a smooth surface with roughness 0.2 nm (Figure 43). Island and pin-hole formation on YIG thin films have been reported in literature [107] [110] [111], but they are usually associated with post-annealing. Our results show that deposition parameters can have a strong influence in the formation of islands during post-annealing.

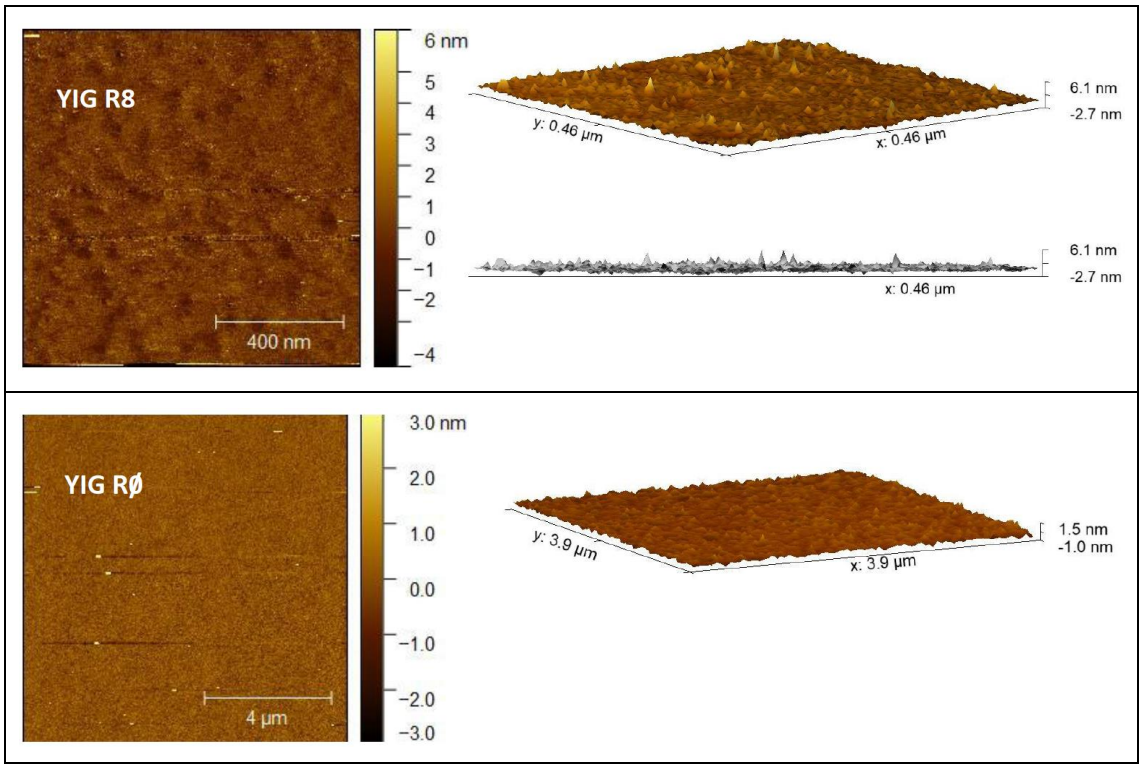

Figure 43: AFM surface analyses for the investigation of fabrication adversities. The deposition parameters used for YIG R8 promoted the achievement of an island-free surface. YIG RØ is the as-deposited surface of the YIG R5 film.

3.1.4 Batch fabrication of YIG thin films and metallic coating

With photoresist protection, GGG (111) substrates were cut into 3×3 and 3×6 mm pieces, intended for VNA-FMR and spin-to-charge current-conversion measurements (V_{sc}), respectively. Deposition parameters were: 75 W rf-power, 12 mTorr work pressure, 15 sccm argon flow and 7.7-cm target-to-substrate distance. The base pressure was 1.5 x 10^{-7} Torr. The deposition time was calculated to give 55-nm-thick YIG films. The annealing was performed in a controlled O_2 atmosphere with a 4-hour plateau of 800ºC, 5ºC/min ramp up and 2ºC/min ramp down. After the

heat-induced recrystallization, the films were returned to the sputtering chamber for metallic coating. Silver (Ag), copper (Cu), niquel (Ni) and cobalt-iron-boron alloy ($Co_{20}Fe_{60}B_{20}$) were used for single- or double-layer coating. The deposition of metals was performed with on-axis configuration, with a 10-cm target-to-substrate distance, 50-sccm argon flow and 50-mTorr work pressure for Ag, 150 mTorr for Cu and Ni, and 100 mTorr for CoFeB.

The name of each sample, *e.g.* YIG3Ag(7)Ni(18), describes its layer structure. The number between parenthesis corresponds to the thickness of the layer in nanometers, and the number after "YIG" indicates to which fabrication batch that sample belongs. Whereas the fabrication route was maintained for all batches, there are environmental variants that are impossible to control and may slightly affect the resulting crystal and magnetic qualities of the YIG thin films. Batch classification is thus necessary to avoid compromising the comparative analyses of this study.

The Gilbert damping coefficient of the YIG thin films used in this study was 7.2×10^{-4}, 8.4×10^{-4}, 9.5×10^{-4}, 10.0×10^{-4}, or 6.7×10^{-4}, according to the batch to which they belong. These values are compatible with values reported by other groups in the literature describing the use of YIG in spintronics [80] [96].

3.2 Magnetic characterization of YIG/spacer/m-FM structures

Recalling the title of the Dissertation, the aim of the present work is to investigate resonance, damping and spin currents in these structures. Although the focus of this project was at first the spin-to-charge current conversion in the m-FM layer, one result in the characterization of the YIG/spacer/m-FM structures drew the attention to a wider picture, where the general regime of nonzero spin densities in the whole trilayer affects the damping of the precessing magnetization in an unexpected way. The unexpected behavior was a reduction, instead of enhancement, of the effective damping of the YIG1/Ag(10)Ni(20) trilayer, as compared to the damping of the bare YIG thin film. In other words, we were at first interested in the behavior of spin currents generated by the resonating FM when they reach a relaxed ferromagnetic metal on the other side of a spacer layer. After the observation of the unexpected behavior, we started to investigate other effects of spin currents transiting the trilayer on the magnetization dynamics of the resonating FM, besides the widely recognized evasion of magnetic moment that causes damping enhancement. The possibility of magnetic interaction between the resonating ferromagnet (active FM, or spin injector) and the static ferromagnet (passive FM, or spin sink) mediated by the spin currents that transit the trilayer was also considered.

3.2.1 Anomalous damping reduction

When checking the presence of spin pumping in metal-coated samples stemming from batches YIG1 and YIG2, a sharp damping reduction, instead of enhancement, was verified for one of the samples, YIG1Ag(10)Ni(20), also accompanied by a narrowing of the FMR linewidths along the entire frequency range (Figure 44a, Table 3). The signal amplitude of the absorption derivative increased for this metallized sample, as compared with the bare YIG film, while the Lorentzian line fitting was remarkably able to better approach the measured data. The other samples, where either Ni or CoFeB was the spin-sink material and either Ag or Cu was the spacer, presented damping enhancement as expected (Figure 44a and b, Table 3).

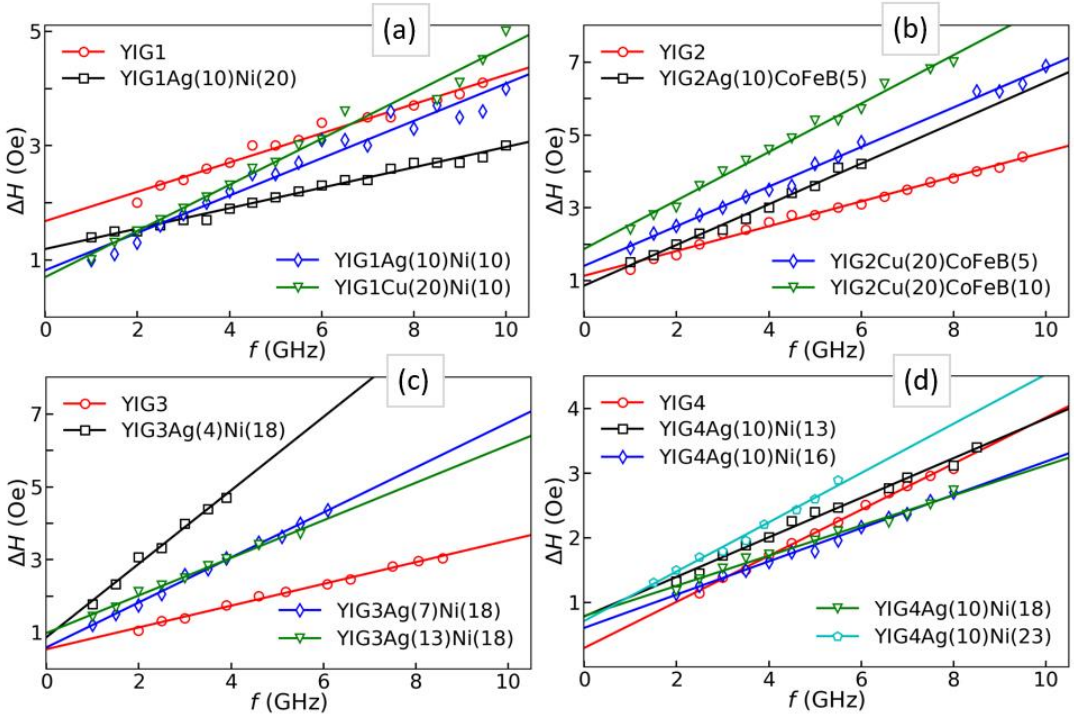

*Figure 44: **Linear fits**. Frequency dependence of the FMR linewidth, for samples belonging to batches YIG1, YIG2, YIG3 and YIG4.*

	α (10^{-4})	$\Delta\alpha$ (10^{-4})	%
YIG1	7.2 ± 0.3	-	-
YIG1Ni(10)	14.6 ± 0.5	7.4 ± 0.8	105 ±15
YIG1Ag(10)Ni(20)	5.0 ± 0.1	-2.2 ± 0.4	-30 ± 4
YIG1Ag(10)Ni(10)	9.2 ± 0.5	2.0 ± 0.8	28 ± 12
YIG1Cu(20)Ni(10)	11.3 ± 0.4	4.1 ± 0.7	57 ± 12

	α (10^{-4})	$\Delta\alpha$ (10^{-4})	%
YIG2	9.5 ± 0.2	-	-
YIG2CoFeB(5)	66.0 ± 5.7	56.5 ± 5.9	595 ± 75
YIG2Ag(10)CoFeB(5)	15.2 ± 0.9	5.7 ± 1.1	60 ± 13
YIG2Cu(20)CoFeB(5)	15.2 ± 0.3	5.7 ± 0.5	62 ± 8
YIG2Cu(20)CoFeB(10)	18.6 ± 0.5	9.1 ± 0.7	100 ± 10

YIG3	8.4 ± 0.2	-	-
YIG3Ag(4)Ni(18)	28.2 ± 1.3	19.8 ± 1.5	235 ±25
YIG3Ag(7)Ni(18)	17.3 ± 0.4	8.9 ± 0.6	110 ±10
YIG3Ag(13)Ni(18)	14.4 ± 0.5	6.0 ± 0.7	72 ± 10

YIG4	10.0 ± 0.2	-	-
YIG4Ag(10)Ni(13)	8.6 ± 0.3	-1.4 ± 0.5	-14 ± 5
YIG4Ag(10)Ni(16)	7.2 ± 0.2	-2.8 ± 0.4	-28 ± 3
YIG4Ag(10)Ni(18)	6.5 ± 0.3	-3.5 ± 0.5	-34 ± 4
YIG4Ag(10)Ni(23)	10.7 ± 0.4	0.7 ±0.6	7 ± 6

YIG5	8.4 ± 0.2	-	-

YIG5Cu(10)Ni(18)	13.2 ± 0.6	4.8 ± 0.8	57 ± 11

Table 3: Damping (α) of the samples belonging to batches YIG1, YIG2, YIG3, YIG4 and YIG5. The damping variation ($\Delta\alpha$) and correspondent percentage change express the enhancement (or reduction) of the damping of metallized samples with respect to the bare YIG sample.

Narrowing of the linewidth indicates that there has been a decrease in the whole relaxation of the magnetization dynamics, *i.e.*, a reduction in the ensemble of all kinds of relaxation processes, either linear or nonlinear, either local or nonlocal. The reduction in the Gilbert damping coefficient observed for the YIG1Ag(10)Ni(20) sample confirms that the reduction in linewidth is due to a decrease in the relaxation processes that characterize the magnetic system under focus, and not simply due to a decrease in ΔH_0 .

Pronounced damping enhancement (Table 3) and large ΔH_0 (above 4 Oe) of the samples lacking a NM spacer were also noted. According to reports on similar FM/FM structures, these are the result of exchange coupling between the layers due to proximity [80], and of inhomogeneous distribution of the exchange coupling throughout the interface [112], respectively. The use of NM spacers is precisely intended to eliminate static coupling between the FM layers, and because Ag and Cu have long spin-diffusion length and weak SOC, they permit spin transport between the FM layers, with minimal dissipation [82] [80]. Now let us observe the extrapolation of the linear fit of the other samples (Figure 44). The quality of our YIG thin films reflects on the small values for inhomogeneous line broadening (ΔH_0 < 2 Oe). The presence of finite ΔH_0 in our samples is probably caused by imperfections originated when the substrates were mechanically cut into the desired size.

Verification samples were fabricated (batches YIG3, YIG4 and YIG5) to consolidate the finding via reproducibility and to check the range of Ag and Ni layer thicknesses for which damping reduction is obtained. The results (Figure 44c and d, Table 3) confirm significant damping reduction for samples with Ag layer thickness of 10 nm, and Ni layer thicknesses of 13, 16 and 18 nm. The sharpest reduction (3.5×10^{-4}) was obtained for the YIG4Ag(10)Ni(18) sample,

corresponding to a reduction of at least 30%. With respect to this sample, the only difference of sample YIG5Cu(10)Ni(18) is that Ag is substituted by Cu in the spacer layer, and damping enhancement of 4.8×10^{-4} was observed in this case (Table 3), which proves that the silver element plays an essential role in the spacer layer for the achievement of damping reduction.

3.2.2 Energy balance

Given the complexity of the processes potentially involved, we choose to approach the discussion about the observed damping reduction in YIG/Ag/Ni structures in terms of the energy conservation principle. Figure 45 shows a diagram of the energy balance in the FMR uniform mode.

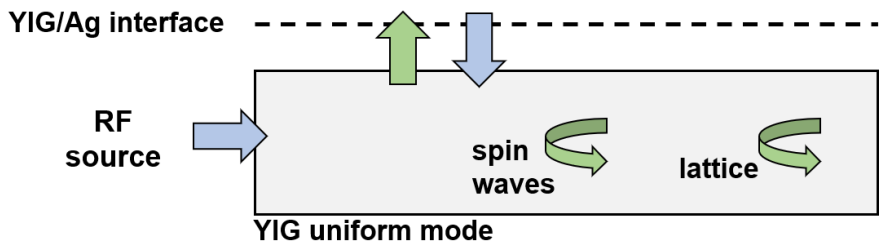

*Figure 45: **Energy balance**. Energy balance of the FMR uniform mode in the YIG layer of a YIG/Ag/Ni sample. The arrows indicate the possible channels for energy entering (blue) or leaving (green) the uniform mode.*

The rf power absorbed by the sample is measured by the FMR technique and corresponds to the power absorbed by the uniform mode. The absorption line obtained by varying the dc magnetic field near the resonance condition gives substantial information about the relaxation mechanisms whereby energy abandons the uniform mode [21]. Energy enters the uniform mode of the YIG layer coming either from the rf source, through interaction with the rf field, or from the YIG/Ag interface, via spin-transfer torque (STT). On the other hand, the uniform mode can lose energy either to the YIG lattice, by coupling with lattice vibrations (magnon-phonon interactions) [113], to other resonance modes ($k \neq 0$), by coupling with spin-wave modes (magnon-magnon interactions) [114], or through the YIG/Ag interface, by transmitting angular momentum via spin pumping [48]. It should be noted that, while direct interactions of the uniform mode with the lattice contribute linearly with frequency to the linewidth, the ones mediated by spin waves are nonlinear [38].

From the point of view of the energy balance of the FMR uniform mode in the YIG layer at dynamic equilibrium, viabilities for damping reduction can be investigated by the following considerations:

1. Spin injection from the Ni layer, through the Ag spacer and into the YIG layer is possible when overlapping of the YIG and Ni dispersion curves permits concurrent resonance. Their dispersion curves do overlap at low frequencies, but they separate as the frequency raises, which means that spin injection from the Ni layer would be in contradiction with the linear behavior observed for the FMR linewidths;
2. Extra energy input from the Ag layer into the YIG layer via STT could be expected if in-plane electric potential were applied, accumulating spins on the YIG/Ag interface through charge-to-spin current conversion in the metallic layers, but there is no applied voltage;
3. If for any reason the ability of the YIG to absorb rf power were modified by the added metallic layers, this would affect the intensity of the absorption peak, but would not reduce the damping;
4. The above considerations imply that the observed damping reduction must be the result of the inhibition of local relaxation processes within the YIG layer. Furthermore, as only Gilbert-type damping is observed, nonlinear relaxation processes are not relevant in the magnetization dynamics in the YIG layer or on the YIG/Ag interface (for our samples). Therefore, inhibition of direct interactions of the uniform mode with the lattice must be the cause of the observed damping reduction.

3.2.3 Dynamic coupling

In a seminal article [115] called *Dynamic Exchange Coupling in Magnetic Bilayers* (2003), B. Heinrich, Y. Tserkovnyak, G. Woltersdorf, A. Brataas, R. Urban and G. E. W. Bauer announced a new coupling mechanism between resonating magnetic layers, mediated by pure spin currents flowing from each magnetic layer to the other, through a nonmagnetic-metal spacer. One remarkable feature of this study is that the coupling between the magnetic layers occurs because the compensating spin currents synchronize, and the determinant condition for this synchronization is that the separately controlled magnetizations of the layers are oriented into alignment. The interest in dynamic coupling was carried over to spin-torque nano-oscillators (STNOs) and the investigations [116] [117] [118] [119] verified that, like many oscillating systems exhibiting nonlinear interactions, STNOs tend to frequency-lock when the difference between their resonance frequencies is small enough. The frequency locking for two coupled STNOs is characterized by a narrowing of the locked-frequency signal linewidth compared with the linewidths of the separately resonating STNOs. Frequency locking is usually accompanied by

phase-locking into a single resonance, whereby an increase in power is also verified. The coupling strength can bring together in frequency two resonances that would otherwise be resonating in different frequencies. Frequency jumps due to frequency locking in STNOs are reported by experimental and theoretical studies to range from about 10 to 100 MHz.

These findings imply that STTs can drive independent magnetizations into coupled dynamics [116]. Investigations of magnetization dynamics in STNOs closely relate to those in ferromagnetic resonance because STT is the Onsager reciprocal of spin pumping [120]. Thus, in our device, spin currents in the Ag layer and/or spin accumulation on the YIG/Ag interface could intermediate a self-synchronization of the uniform-mode magnons in YIG, as described in the next section. This coupling would strengthen the resonance mode at which it occurs. Magnon-phonon coupling, which is substantially responsible for the relaxation in ferromagnetic insulators, will now have to compete with the spin current-driven dynamic coupling. This strengthening of the uniform mode would thus inhibit the relaxation due to coupling with lattice vibrations (phonons) and result in a reduction of damping in the garnet.

3.2.4 Self-synchronization

Upon the YIG thin-film fabrication on the GGG substrate, all attempts are usually made to obtain a monocrystalline thin film. The division of the YIG thin film into separate crystalline phases is usually undesirable. When this is the case, FMR measurements exhibit double or multiple peaks with slightly different resonance fields, each corresponding to a different crystalline phase. This is explained by the fact that each of these phases has a slightly different saturation magnetization, which reflects on a slightly shifted FMR dispersion curve for each phase [96]. At 9.5 GHz, the presence of a small secondary peak in the FMR line shape of our bare YIG1 thin film contrasts with the line shape of the YIG1Ag(10)Ni(20) sample, which exhibits a perfect single Lorentzian peak (Figure 46). This is evidence of the strengthening of the uniform mode in the YIG layer. The precessing magnetizations of the YIG crystalline phases with slightly different natural resonance frequencies become frequency-locked due to a coupling spin torque [116]. Another evidence of this coupling is that the power absorbed by the metallized YIG thin film is at least twice as high as the bare YIG. It should be noted that self-synchronization of oscillating magnetizations has been extensively reported to occur via spin torques originating in spin waves, electric current, microwave field or dipole interaction (see Ref. [121] and references therein), whereas the coupling torque elicited in the theoretical treatment, as developed in Ref. [116], of the dynamic coupling driven by pure spin currents is much stronger, as compared to the coupling driven by electric currents [121].

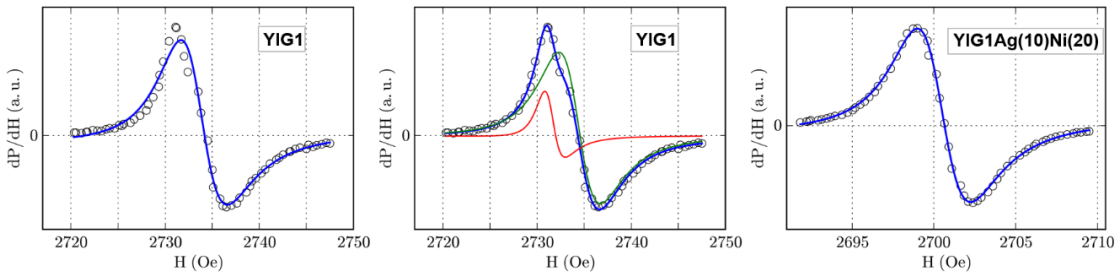

*Figure 46: **Lorentzian resonance lines**. Comparison of the FMR line shapes at 9.5 GHz of YIG without and with metallic coating. On the left and on the right, single-peak Lorentzian fits (blue line) to the measured data (black circles). In the center, a two-peak Lorentzian fit, where the blue line is the sum of the red and the green lines. Note that the FMR absorption-line graph of the metallized YIG (on the right) has a different horizontal scale for the applied field H from the graphs of the bare YIG thin film.*

3.2.5 The transport of nonzero spin densities

Although the exact regime of pure spin currents and non-equilibrium spin accumulation (nonzero spin density) throughout the YIG1Ag(10)Ni(20) sample at FMR remains unclear, the presence of spin current is evidenced via detection of spin current-induced voltage on the metallic Ni surface, using the spin-Hall geometry (Figure 47, Table 4). ISHE, ASHE and IREE can be involved in the spin-to-charge current conversion that generates the observed voltage [11] [12] [68] [69], even though the presence of ferromagnetism on the interfaces renders uncertain the participation of IRRE [11]. The spin current reaching the Ag/Ni interface will be partially reflected and partially transmitted into the Ni layer, where it will be converted into charge current via ISHE and ASHE. (See Section 1.5.3.) Part of the spin current might also be converted into charge current at the interface, via IREE. These effects observe similar spatial geometry and contribute to the spin-to-charge current conversion sensed as the V_{sc} voltage.

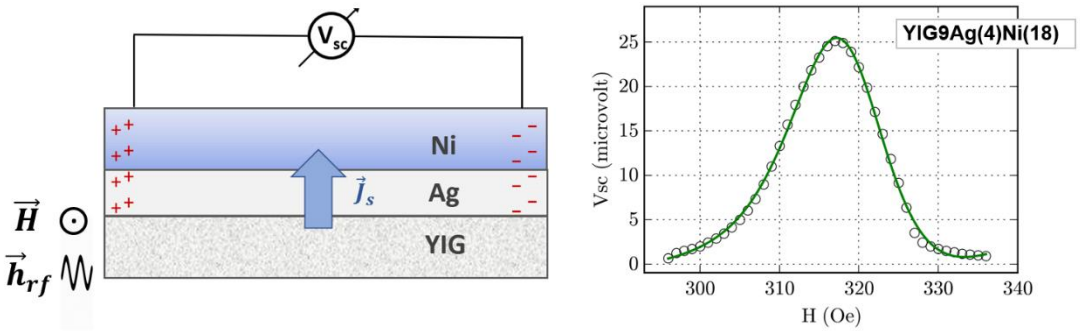

*Figure 47: **Spin-current detection**. Left: Detection of the spin-to-charge current conversion in our trilayer structure, where YIG is the spin injector, Ag is the spacer and Ni, the spin sink. Right: The measured voltage (V_{sc}) results from spin-to-charge current conversion at 2GHz. The green line is the Lorentzian fit to the measured data (black circles).*

	$\Delta\alpha$ (10^{-4})	$I_{sc} = V_{sc}/R$ (μA)
YIG1Ag(10)Ni(20)	-2.2	0.04
YIG1Cu(20)Ni(10)	4	0.42
YIG3Ag(4)Ni(18)	19.8	0.18
YIG3Ag(7)Ni(18)	8.9	0.09
YIG4Ag(10)Ni(13)	-1.4	0.01
YIG4Ag(10)Ni(16)	-2.8	0.06
YIG4Ag(10)Ni(18)	-3.5	0.02
YIG4Ag(10)Ni(23)	0.7	0.04
YIG5Cu(10)Ni(18)	4.8	0.28
YIG2Ag(10)CoFeB(5)	6.1	0.02
YIG2Cu(20)CoFeB(10)	9.1	0.05

Table 4: Spin-to-charge current conversion (I_{sc}), calculated from V_{sc} and the resistance (R) measured between two contact probes placed on the metallic surface of each sample, while driving the YIG layer into FMR at 2 GHz.

While a similar damping reduction (relative to the bare magnetic film at FMR, and without applied current) reported in Ref. [122] for a magnetic ultrathin-film structure was mainly attributed to Rashba spin-orbit torques generated at backflow of spin current, we propose that backflow of spin current on the Ag/Ni interface is essential for the establishment of the above-mentioned dynamic magnetic coupling in our sample. Thus, in the FMR condition, the precession magnetization of the YIG pumps spin angular momentum through the YIG/Ag interface, then polarized spins accumulate near the interface and diffuse across the Ag layer with virtually no spin-flip losses [82] until they reach the Ag/Ni interface, which (partially) reflects this spin current back to the Ag layer towards and through the YIG/Ag interface, into the YIG layer [13]. When we compare the intensity of I_{sc} with the amount of damping reduction obtained for the four samples (Table 4, in red), the relation between them remains unclear. But when we compare the intensities of I_{sc} for these samples with the intensities for corresponding copper-substituted samples, *i.e.*, YIG1Cu(20)Ni(10) and YIG5Cu(10)Ni(18), we note that the spin current converted into charge current in the latter case (Cu spacer) is one order of magnitude above, as compared to the former case (Ag spacer). This difference is in accordance with the assumption that backflow of spin current at the Ag/Ni interface is involved in the observed damping reduction, and consequently also supports the involvement of dynamic coupling. This picture is consolidated by the realization that backflow of spin current from the Ag/Ni interface and across the Ag spacer will at least partly traverse the YIG/Ag interface back into the YIG layer, and thus compensate the outflow of angular momentum caused by spin pumping. After all, in the frame of the uniform mode's energy balance (Figure 45), the inhibition of local damping in the YIG must overcome the non-local damping caused by the spin-pumping so that the damping-reduction effect can take place.

3.2.6 The role of the Ni layer

Being ferromagnetic, nickel can also be excited into FMR, and concurrent excitation of YIG and nickel is possible at low frequencies. However, as reasoned above, concurrent excitation of the Ni layer is not likely to play a relevant role in the observed damping reduction. Besides the linear frequency dependence of the linewidth, the results obtained for the YIG4Ag(10)Ni(x) verification samples also support this assumption. Three samples with different thicknesses of Ni layer exhibit damping reduction. While spin-pumping efficiency is expected to be inversely proportional to injector-layer thickness [8], the observed damping-reduction effect increases for thicker layers of Ni. In contrast to Ni-layer thickness, the reduction effect seems to be extremely sensitive to Ag-layer thickness. Among the unanswered questions that this study elicits is why the samples with Ag layer thickness different from 10 nm do not exhibit damping reduction.

3.2.7 Batch YIGTØ

We have chosen to postpone comments on this batch because it brings a difficulty. It corresponds to the first YIG thin-film fabrication after the replacement of the deteriorated targets. (See Section 3.1.3.) As compared with the other batches, it is more numerous (eight samples). As a rule, for the fabrication of each batch, we have observed that all the pieces must be subjected together to the deposition procedure and to the annealing, but YIGTØ was an exception. The deposition was performed in two turns, one for the first half of the substrate pieces and another for the second half. (The annealing, however, was subsequently performed in one single turn, with all eight pieces together.)

While it is possible that the two-turn execution of the deposition has inserted some degree of variation of quality between the two halves of samples, this possibility is reduced by the fact that the depositions were performed with a pre-calibrated valve-position control of the work pressure, instead of a sensor-controlled work pressure. The valve-position control gives a much more stable work pressure, which is faithfully reproduced in subsequent depositions. Another fact is that the two depositions were performed one immediately after the other, reducing the chance of other unwanted factors, like temperature and base-pressure variation.

In the sequence of YIG thin-film batches fabricated for this work, batch YIGTØ was produced after YIG2 and before YIG3. At that point, the only sample exhibiting damping reduction was YIG1Ag(10)Ni(20) and we were interested in reproducing the damping reduction and verifying the range of thicknesses of the Ag and Ni layers for which reduction took place. For the metallic coating of the eight YIGTØ pieces, the thickness of Ni was varied while maintaining

the 10-nm thickness of the Ag layer, and the thickness of the Ag was varied while maintaining the 20-nm thickness of the Ni layer. Figure 48 and Table 5 show the linear fits and the damping variations obtained. While damping reduction was not verified for the Ag(10)Ni(20) coating as expected, the sample YIGTØAg(10)Ni(16) exhibited a reduction of approximately 2×10^{-4} (with an effective damping of 4.8×10^{-4}, which would be the lowest of all samples in this study). This explains why we chose the Ni-layer thickness of 18 nm for the metallic coating of the subsequent set of samples (batch YIG3). We attributed the difference in thickness of the Ni layer of the samples for which damping reduction was observed to an inaccuracy in the calibration of the Ni deposition rate.

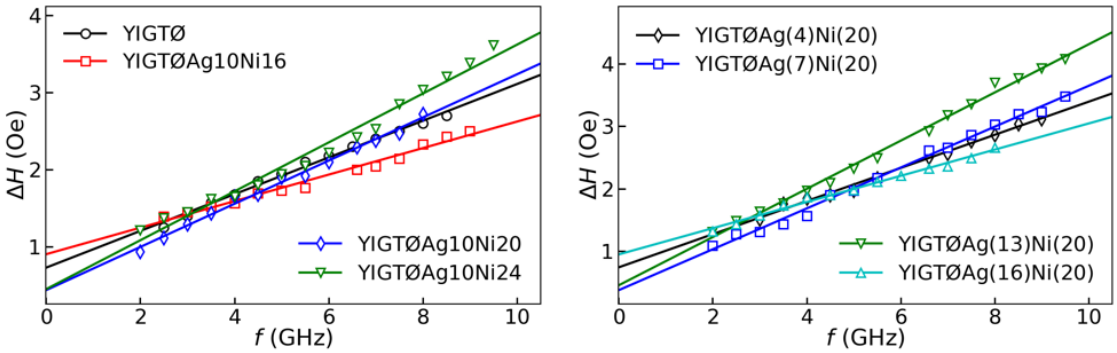

Figure 48: Frequency dependence of the HWHM linewidth for the samples belonging to batch YIGTØ. The linear fits for the eight samples were plotted in two separate graphs to improve clarity.

	α (10^{-4})	$\Delta\alpha$ (10^{-4})	%
YIGTØ	6.7 ± 0.2	-	-
YIGTØAg(10)Ni(16)	4.8 ± 0.2	-1.9 ± 0.4	-28 ± 5
YIGTØAg(10)Ni(20)	7.9 ± 0.2	1.2 ± 0.4	18 ± 7
YIGTØAg(10)Ni(24)	8.9 ± 0.3	2.2 ± 0.5	33 ± 8

	α (10^{-4})	$\Delta\alpha$ (10^{-4})	%
YIGTØAg(4)Ni(20)	7.4 ± 0.2	0.7 ± 0.4	10 ± 7
YIGTØAg(7)Ni(20)	9.2 ± 0.2	2.5 ± 0.4	38 ± 7
YIGTØAg(13)Ni(20)	10.8 ± 0.2	4.1 ± 0.4	61 ± 8
YIGTØAg(16)Ni(20)	5.9 ± 0.2	-0.8 ± 0.4	-12 ± 6

Table 5: Damping (α) and damping variation ($\Delta\alpha$, %) of the samples belonging to batch YIGTØ.

The sample YIGTØAg(16)Ni(20) also exhibited damping reduction. Although the reduction was small (approximately 0.8×10^{-4}), this result raised the question whether there is periodicity in the Ag-layer thickness for the verification of the observed effect. We expected to verify this possibility by measuring the effective damping of sample YIG3Ag(16)Ni(18), but this sample was unfortunately lost in the sputtering chamber even before its fabrication was completed. So, an extra sample with Ag(16)Ni(18) coating was produced from the YIG5 batch of thin films and the effective damping calculated from the linear fit of the frequency dependence of the linewidths (Figure 49). We obtained α = 5.9 ± 0.2, and thus $\Delta\alpha$ = -2.5 ± 0.4 (which corresponds to a reduction of 30 ± 4 percent), considering that the value of the damping for the YIG5 thin film was found to be 8.4 ± 0.2 (Table 3).

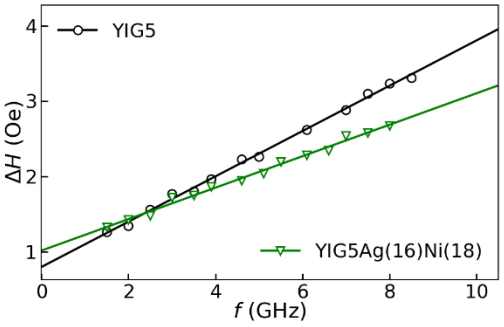

Figure 49: Damping reduction for YIG5Ag(16)Ni(18), as portrayed by the frequency dependence of the linewidth of the bare YIG thin film and the metallized sample.

3.3 Further considerations

1. In the preceding Section, the suggestion of periodic dependence on the Ag-layer thickness of the damping-reduction effect was reinforced by the damping reduction observed for sample YIG5Ag(16)Ni(18). However, this is a hypothesis that must be confirmed or refuted by further investigation.

2. The main assertion proposed by this Dissertation is the verification of effective damping reduction for YIG thin films coated with Ag/Ni layers, which was consolidated by reproducibility and by the discussion of its physical viability. Against the background conformed by the present state of the art in the field of spintronics, this damping reduction constitutes an anomalous effect. The referred finding is asserted in this Dissertation, and supported by a qualitative and comparative analysis of damping measurements. A physical viability is suggested in which dynamic coupling and self-synchronization play crucial roles, and this conjecture is, in turn, consolidated by a comparison of orders of magnitude between the effective damping behavior and the electrical detection of spin currents (Section 3.2). This testifies in favor of the robustness of the arguments assembled along the Discussion, and of the Conclusions summarized in the next Chapter.

3. Along the course of this work's development, a patent application was written in collaboration with the Technological Innovation Center of Rio de Janeiro (NITRio), and registered at the Brazilian Institute of Industrial Property (INPI). The application's register details are listed below:

Title: Method to reduce damping in YIG thin films, consisting in Ag/Ni coating.
Patent applicant: CBPF
Date: May 25th, 2021
Name of inventors: Eric Hermanny, Diego Ernesto González-Chávez, Rubem Luis Sommer
Application number: BR 10 2021 010142 3
Status of application: pending

4. A manuscript reporting the finding announced in this Dissertation and containing the arguments developed to physically explain the damping reduction is currently under consideration by the editorial team and reviewers of the periodical Scientific Reports, from Nature Portfolio. A preprint can be found online, under the DOI: 10.21203/rs.3.rs-722918/v1.

5. The investigation of a possible effective damping reduction in the polycrystalline YIG thin film successfully grown on Si substrate with a 5-mTorr work pressure was not possible in the timespan of this project. At the time this sample was deposited, our investigation on the fabrication of YIG thin films was still in an early phase, so the annealing of the sample was not performed in a controlled oxygen atmosphere, but in air (as reported in Section 3.1.1). As discussed in Section 3.1.2, the implementation of controlled oxygen atmosphere for the annealing process of YIG thin films is essential for the crystalline and magnetic quality of the film, especially the surface quality. Besides, the surface of the 5-mTorr thin-film sample was compromised by contamination with the grease used to adhere the sample to the waveguide during the FMR measurements, and the fabrication of new samples could not be done in a timely manner.

However, we performed a new, broadband FMR measurement of the original sample, using the extended range of magnetizing field intensities provided by the installed electromagnet (as described in Sections 2.1 and 3.1.2). The magnetic quality of the film was thus confirmed. The colormap (Figure 50) shows a sharp dispersion curve extending throughout the whole frequency range (500 MHz to 10 GHz). An effective saturation magnetization of 1070 Gauss was calculated by fitting the dispersion curve with the Kittel formula. This value is below reported results for similar polycrystalline YIG thin films in the literature (*e.g.* 1430 Gauss, in Ref. [92]), but not very far from the results obtained for YIG thin films grown on GGG substrates in this study (Table 2). While higher annealing temperatures are likely to produce YIG thin films with higher saturation magnetizations, they may also increase the incidence of parasitic phases (as reported in Section 3.1.1) or cause morphological defects (like excessive grain size and cracks), which would be extremely detrimental to the spin pumping efficiency of these films. For this reason, the value of the annealing plateau temperature was chosen so that the crystallization would be sufficient to

give a satisfying value of the saturation magnetization, without compromising the quality of the film, due to morphological defects.

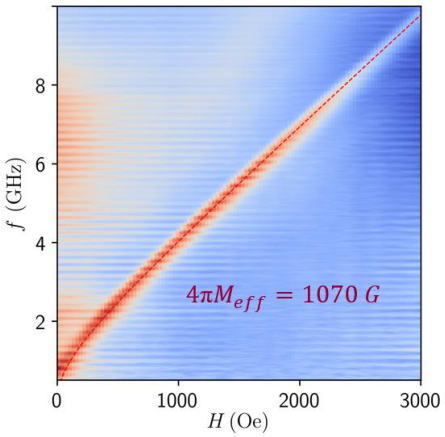

Figure 50: Extended-band VNA-FMR colormap showing the dispersion curve of the polycrystalline YIG thin film deposited on Si substrate via off-axis magnetron sputtering with a 5-mTorr work pressure. (Cf. Figure 31.) The dotted red line is the fit to the dispersion curve (using the Kittel formula), whereby the effective saturation magnetization is calculated.

4. Conclusions and outlook

In the preliminary part of this study, we demonstrated that YIG thin film crystallization on nonconventional substrates is drastically sensitive to the work pressure used for sputtering deposition. We obtained remarkable magnetic features for the film deposited via off-axis configuration on Si (100) substrate, under a 5-mTorr work pressure. This indicates better nucleation for atoms arriving at the substrate with lower energy (off-axis), and better stoichiometry when these atoms have gone through less collisions with the plasma (low work pressure).

Spintronic-compatible YIG thin films were obtained on GGG (111) substrates with on-axis sputtering deposition, and with post-annealing performed in a controlled oxygen atmosphere. These results exhibited much less sensitivity to the work-pressure deposition parameter. Even though the achievement of monocrystalline YIG thin films was desired, the appearance of a secondary peak on the resonance lines helped us to understand the physics behind the core finding brought by this work.

This Dissertation announces the achievement of major damping reduction, of at least 30%, in YIG thin films with the deposition of a metallic coating, without the need of applied current (Figure 51). The discovery is unprecedented, either for YIG or any other magnetic material, and is consolidated by reproducibility. Although the theory behind the observed effect of the Ag/Ni metallization on YIG remains unclear, this study exhibits strong evidence that spin current-driven self-synchronization of the FMR uniform mode in the YIG layer plays a decisive role. It strengthens the uniform mode, thus inhibiting magnon-phonon coupling, which implies a delay in this relaxation channel. Backflow of spin current at the Ag/Ni interface also seems to be essential for the damping reduction taking place. It influences the self-synchronization, which is mediated by the spin currents, and generates an inflow of angular momentum into the YIG that compensates the outflow caused by the spin pumping.

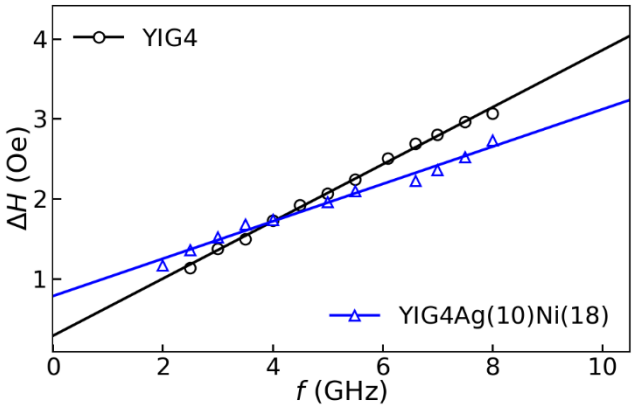

Figure 51: ***Major effective-damping reduction without applied current.*** *Among other samples, YIG4Ag(10)Ni(18) exhibited a damping reduction of 34±4%. (Cf. Figure 44 and Table 3.)*

Further investigation involving poly- and monocrystalline YIG, a greater range of layer thicknesses and applied charge current is necessary to determine the impact this finding may have on the development of new magnonic and spintronic devices. Does the range of Ni-layer thicknesses for which the reduction effect takes place depend on the YIG thin-film thickness? Can the suspected periodicity of the effect, with respect to the Ag-layer thickness (*e.g.*,10 nm, 16 nm), be confirmed by reproducibility? These questions should be answered by further experimentation with a greater variety of samples, fabricated with the same route for YIG thin films as in this work, but different combinations of layer thicknesses.

Polycrystalline YIG thin films are object of great interest in the investigation of new devices for the microwave industry, benefiting from the low damping parameter of YIG. Lower damping means higher power efficiency. The assumption that the damping reduction observed in the present study of YIG thin films bearing only a few crystalline phases is due to the dynamic coupling of these few phases prompts the investigation of the effective damping in polycrystalline YIG films coated with Ag/Ni layers.

In our argument about the physics behind the anomalous damping reduction, self-synchronization of the FMR uniform mode plays a crucial role (it causes the strengthening of the FMR uniform mode), and results from the dynamic coupling of different crystallographic phases of YIG. Should it be expected that capping a monocrystalline YIG thin film with Ag/Ni layers will therefore not result in a strengthening of the FMR uniform mode? Spin-pumping experiments with Ag/Ni-coated monocrystalline YIG thin films will provide an empirical verification of this assumption.

Through spin transfer torque, charge current applied on the metallic coating is bound to further reduce the effective damping. Depending on the charge current density that the Ag/Ni coating can bear, full compensation of the damping may be achieved. And depending on whether frequency and phase locking will persevere in high charge-current densities, this structure might also support the realization of the predicted SWASER devices. Therefore, another important development suggested by this Dissertation are FMR experiments with applied in-plane electric potential on the Ag/Ni layers of YIG/Ag/Ni structures.

A side investigation, which was a consequence of the deterioration of our YIG targets, revealed that the formation of islands on the surface of YIG thin films can be reverted by the adjustment of deposition parameters (work pressure and argon flow). The emergence of these islands is thus probably caused by stoichiometric imbalance. The control of the deposition parameters would compensate the intrinsic imbalance of the deteriorated target. This revelation has impact on the present knowledge about the fabrication of YIG thin films, because literature on the subject attributes the formation of islands solely to the adjustment of annealing parameters, like temperature and duration. The reduced magnetism verified in the samples fabricated with deteriorated targets, regardless of the deposition parameters used, indicate that the compensation provided by the adjustment of deposition parameters is only superficial: while the surface of the film responds to the adjustments, the crystallization of the bulk would remain compromised. For the development of the investigation on the influence of deposition parameters over the formation of islands on the surface of YIG thin films, we suggest that transmission electron microscopy characterization could complement the AFM surface characterization, revealing stoichiometric details of the samples at different depths of the YIG film.

Bibliography

[1] Z. Wang, Y. Sun, M. Wu, V. Tiberkevich and A. Slavin, "Control of spin waves in a thin film ferromagnetic Insulator through interfacial spin scattering," *Phys. Rev. Lett.,* vol. 107, p. 146602, 2011.

[2] M. Haidar, P. Dürrenfeld, M. Ranjbar, M. Balinsky, M. Fazlali, M. Dvornik, R. K. Dumas, S. Khartsev and J. Akerman, "Controlling Gilbert damping in a YIG film using nonlocal spin currents," *Phys. Rev. B,* vol. 94, p. 180409 (R), 2016.

[3] D. Tiwari, N. Behera, A. Kumar, P. Dürrenfeld, S. Chaudhary, D. K. Pandya, J. Akerman and P. K. Muduli, "Antidamping spin-orbit torques in epitaxial-Py(100)/β-Ta," *Appl. Phys. Lett.,* vol. 111, p. 232407, 2017.

[4] M. Evelt, V. E. Demidov, V. Bessonov, S. O. Demokritov, J. L. Prieto, M. Muñoz, J. B. Youssef, V. V. Naletov, G. d. Loubens, O. Klein, M. Collet, K. Garcia-Hernandez, P. Bortolotti, V. Cros and A. Anane, "High-efficiency control of spin-wave propagation in ultra-thin yttrium iron garnet by the spin-orbit torque," *Appl. Phys. Lett.,* vol. 108, p. 172406, 2016.

[5] L. Berger, "Emission of spin waves by a magnetic multilayer traversed by a current," *Phys. Rev. B,* vol. 54, pp. 9353-9358, 1996.

[6] L. Berger, "Multilayers as spin-wave emitting diodes," *J. Appl. Phys.,* vol. 81, pp. 4880-4882, 1997.

[7] L. Berger, "Spin-wave emitting diodes and spin diffusion in magnetic multilayers," *IEEE Trans. Magn.,* vol. 34, pp. 3837-3841, 1998.

[8] M. Collet, X. d. Milly, O. d. Kelly, V. V. Naletov, R. Bernard, P. Bortolotti, J. B. Youssef, V. E. Demidov, S. O. Demokritov, J. L. Prieto, M. Muñoz, V. Cros, A. Anane, G. d. Loubens and O. Klein, "Generation of coherent spin-wave modes in yttrium iron garnet microdiscs by spin–orbit torque," *Nat. Commun.,* vol. 7, no. 10377, 2016.

[9] Y. Tserkovnyak, A. Brataas and G. E. Bauer, "Enhanced Gilbert damping in thin ferromagnetic films," *Phys. Rev. Lett.,* vol. 88, p. 117601, 2002.

[10] E. Saitoh, M. Ueda, H. Miyajima and G. Tatara, "Conversion of spin current into charge current at room temperature: Inverse spin-Hall effect," *App. Phys. Lett.,* vol. 88, p. 182509, 2006.

[11] J. C. Rojas-Sánchez, L. Vila, G. Desfonds, S. Gambarelli, J. P. Attané, J. M. DeTeresa, C. Magén and A. Fert, "Spin-to-charge conversion using Rashba coupling at the interface between non-magnetic materials," *Nat. Commun.,* vol. 4, p. 2944, 2013.

[12] K. S. Das, W. Y. Schoemaker, B. J. vanWees and I. J. Vera-Marun, "Spin injection and detection via the anomalous spin Hall effect of a ferromagnetic metal," *Phys. Rev. B,* vol. 96, p. 220408, 2017.

[13] Y. Tserkovnyak, A. Brataas and G. E. W. Bauer, "Dynamic exchange coupling and Gilbert damping in magnetic multilayers," *J. Appl. Phys.,* vol. 93, pp. 7534-7538, 2003.

[14] D. A. Arena, E. Vescovo, C.-C. Kao, Y. Guan and W. E. Bailey, "Weakly coupled motion of individual layers in ferromagnetic resonance," *Phys. Rev. B,* vol. 74, p. 064409, 2006.

[15] H. Skarsvag, G. E. W. Bauer and A. Brataas, "Current-induced magnetization dynamics in two magnetic insulators separated by a normal metal," *Phys. Rev. B,* vol. 90, p. 054401, 2014.

[16] Ł. Gladczuk, L. Gladczuk, P. Dluzewski, K. Lasek, P. Aleshkevych, D. M. Burn, G. v. d. Laan and T. Hesjedal, "Spin-current mediated exchange coupling in MgO-based magnetic tunnel junctions," *Phys. Rev. B,* vol. 103, p. 064416, 2021.

[17] V. E. Demidov, S. Urazhdin, E. R. J. Edwards, M. D. Stiles, R. D. McMichael and S. O. Demokritov, "Control of magnetic fluctuations by spin current," *Phys. Rev. Lett.,* vol. 107, p. 107204, 2011.

[18] H. Skarsvag, A. Kapelrud and A. Brataas, "Spin waves in ferromagnetic insulators coupled via a normal metal," *Phys. Rev. B,* vol. 90, p. 094418, 2014.

[19] L. Bonneviot and D. Oliver, "Ferromagnetic Resonance," in *Catalyst Characterization – Physical Techniques for Solid Materials*, New York, Springer Science, 1994.

[20] J. M. D. Coey, Magnetism and Magnetic Materials, New York: Cambridge University Press, 2009.

[21] S. V. Vonsovskii, "Magnetic Resonance in Ferromagnetics," in *Ferromagnetic Resonance*, Pergamon Press, 1966.

[22] M. R. Freeman, W. K. Hiebert and A. Stankiewicz, "Time-resolved scanning Kerr microscopy of ferromagnetic structures," *Journal of Applied Physics,* vol. 83, 1998.

[23] D. E. González-Chávez, Propriedades magnéticas de filmes finos: um estudo por ressonância ferromagnética de banda larga (PhD Dissertation), Rio de Janeiro: CBPF, 2013.

[24] M. Bonfim, K. Mackay, M.-L. A. S. Pizzini and A. Fontaine, "Nanosecond resolved techniques for dynamical magnetization reversal measurements," *Journal of Applied Physics,* vol. 87, 2000.

[25] J. F. Cochran, "Light scattering from ultrathin layers and bilayers," in *Ultrathin magnetic structures II*, Springer Verlag, 2005.

[26] J. Goulon, A. Rogalev, G. Goujon, F. Wilhelm, J. B. Youssef, C. Gros, J.-M. Barbe and R. Guilard, "X-Ray Detected Magnetic Resonance: A Unique Probe of the Precession Dynamics of Orbital Magnetization Components," *Int. J. Mol. Sci,* vol. 12, pp. 8797-8835, 2011.

[27] J. A. Sidles, J. L. Garbini, K. J. Bruland, D. Rugar, O. Züger, S. Hoen and C. S. Yannoni, "Magnetic resonance force microscopy," *Rev. Mod. Phys.,* vol. 67, 1995.

[28] G. V. Skrotskii and L. V. Kurbatov, "Phenomenological Theory of Ferromagnetic Resonance," in *Ferromagnetic Resonance*, Pergamon Press, 1966.

[29] J. H. E. Griffiths, "Anomalous high-frequency resistance of FM metals," *Nature,* vol. 184, pp. 670-671, 1946.

[30] K. Lenz, H. Wende, W. Kuch, K. Baberschke, K. Nagy and A. Jánossy, "Two-magnon scattering and viscous Gilbert damping in ultrathin ferromagnets," *Physical Review B,* vol. 73, p. 144424(6), 2006.

[31] T. L. Gilbert, "A phenomenological theory of damping in ferromagnetic materials," *IEEE Transaction on Magnetics,* vol. 40, no. 6, pp. 3443-3449, 2004.

[32] C. K. Lo, W. C. Lai and J. C. Cheng, "Note: Vector network analyzer-ferromagnetic resonance spectometer using high-quality Q-factor quality," *Rev. Sci. Instrum.,* vol. 82, pp. 086114(1-3), 2011.

[33] M. Harder and C.-M. Hu, "Chapter Two: Cavity Spintronics: An Early Review of Recent Progress in the Study of Magnon–Photon Level Repulsion," in *Solid State Physics, Vol. 69*, Elsevier, 2018, pp. 47-121.

[34] C. Kittel, Introduction to Solid State Physics, Wiley, 2005.

[35] J. Lindner, K. Lenz, E. Kosubek, K. Baberschke, D. Spoddig, R. Meckenstock, J. Pelzl, Z. Frait and D. L. Mills, "Non-Gilbert-type damping of the magnetic relaxation in ultrathin ferromagnets: Importance of magnon-magnon scattering," *Physical Review B,* vol. 68, p. 060102(4), 2003.

[36] J. B. S. Mendes, L. H. Vilela-Leão, S. M. Rezende and A. Azevedo, "Possible Interplay Between Intrinsic and ExtrinsicFerromagnetic Damping Mechanisms," *IEEE Trans. Magn.,* vol. 46, pp. 2293-2296, 2010.

[37] H. Suhl, "Theory of the magnetic damping constant," *IEEE Transactions on Magnetics,* vol. 34, no. 4, pp. 1834-1838, 1998.

[38] K. Zakeri, J. Lindner, I. Barsukov, R. Meckenstock, M. Farle, U. v. Hörsten, H. Wende, W. Keune, J. Rocker, S. S. Kalarickal, K. Lenz, W. Kuch, K. Baberschke and Z. Frait, "Spin dynamics in ferromagnets: Gilbert damping and two-magnon scattering," *Physical Review B,* vol. 76, p. 104416(8), 2007.

[39] A. Y. Dobin and R. H. Victora, "Intrinsic nonlinear ferromagnetic relaxation," *Journal of Applied Physics,* vol. 95, pp. 7139-7144, 2004.

[40] D. L. Mills and R. Arias, "The damping of spin motions in ultrathin films: Is the Landau-Lifshitz-Gilbert phenomenology applicable?," *Physica B,* vol. 384, pp. 147-151, 2006.

[41] V. G. Bar'yakhtar and D. A. Ivanov, "The Landau-Lifshitz equation: 80 years of history, advances, and prospects," *Low Temp. Phys.,* vol. 41, pp. 663-669, 2015.

[42] V. N. Krivoruchko, "Spin waves damping in nanometer-scale magnetic materials," *Low Temp. Phys.,* vol. 41, no. 9, pp. 670-681, 2015.

[43] O. V. Sukhostavet and J. M. Gonzalez, "Effective magnetization damping for a dynamical spin texture in metallic ferrromagnet," *Low Temp. Phys.,* vol. 41, no. 10, pp. 772-777, 2015.

[44] B. Heinrich, "Spin relaxation in magnetic metallic layers and multilayers," in *Ultrathin Magnetic Structures III*, Springer-Verlag, 2005.

[45] M. J. Hurben and C. E. Patton, "Theory of two magnon scattering microwave relaxation and ferromagnetic resonance linewidth in magnetic thin films," *Journal of Applied Physics,* vol. 83, no. 8, pp. 4344-4365, 1998.

[46] R. Arias and D. L. Mills, "Extrinsic contributions to the ferromagnetic resonance response of ultrathin films," *Physical Review B,* vol. 60, no. 10, pp. 7395-7408, 1999.

[47] S. Mizukami, Y. Ando and T. Miyazaki, "The study on ferromagnetic resonance linewidth for NM/80NiFe/NM (NM = Cu, Ta, Pd and Pt) films," *Jpn. J. Appl. Phys.,* vol. 40, p. 580–585, 2001.

[48] Y. Tserkovnyak, A. Brataas and G. E. W. Bauer, "Spin pumping and magnetization dynamics in metallic multilayers," *Phys. Rev. B,* vol. 66, p. 224403, 2002.

[49] Y. K. Kato, R. C. Myers, A. C. Gossard and D. D. Awschalom, "Observation of the spin Hall effect in semiconductors," *Science,* vol. 306, pp. 1910-1913, 2004.

[50] J. Wunderlich, B. Kaestner, J. Sinova and T. Jungwirth, "Experimental observation of the spin-Hall effect in a two-dimensional spin-orbit coupled semiconductor system," *Physical Review B,* vol. 94, p. 047204, 2005.

[51] Y. Kajiwara, K. Harii, S. Takahashi, J. Ohe, K. Uchida, M. Mizuguchi, H. Umezawa, H. Kawai, K. Ando, K. Takanashi, S. Maekawa and E. Saitoh, "Transmission of electrical signals by spin-wave interconversion in a magnetic insulator," *Nat. Lett.,* vol. 464, pp. 262-267, 2010.

[52] L. J. Cornelissen, J. Liu, R. A. Duine, J. B. Youssef and B. J. vanWees, "Long-distance transport of magnon spin information in a magnetic insulator at room temperature," *Nat. Phys. Lett.,* 2015.

[53] V. E. Demidov, S. Urazhdin, H. Ulrichs, V. Tiberkevich, A. Slavin, D. Baither, G. Schmitz and S. O. Demokritov, "Magnetic nano-oscillator driven by pure spin current," *Nat. Mat. Lett.,* vol. 11, pp. 1028-1031, 2012.

[54] A. Hamadeh, O. d. Kelly, C. Hahn, H. Meley, R. Bernard, A. H. Molpeceres, V. V. Naletov, M. Viret, A. Anane, V. Cros, S. O. Demokritov, J. L. Prieto, M. Muñoz, G. deLoubens and O. Klein, "Full control of the spin-wave damping in a magnetic insulator using spin-orbit torque," *Phys. Rev. Lett.,* vol. 113, p. 197203, 2014.

[55] T. Wimmer, M. Althammer, L. Liensberger, N. Vlietstra, S. Geprägs, M. Weiler, R. Gross and H. Huebl, "Spin transport in a magnetic insulator with zero effective damping," *Phys. Rev. Lett.,* vol. 123, p. 257201, 2019.

[56] I. M. Miron, T. Moore, H. Szambolics, L. D. Buda-Prejbeanu, S. Auffret, B. Rodmacq, S. Pizzini, J. Vogel, M. Bonfim, A. Schuhl and G. Gaudin, "Fast current-induced domain-wall motion controlled by the Rashba effect," *Nat. Mat. Lett.,* vol. 10, pp. 419-423, 2011.

[57] I. M. Miron, K. Garello, G. Gaudin, P.-J. Zermatten, M. V. Costache, S. Auffret, S. Bandiera, B. Rodmacq, A. Schuhl and P. Gambardella, "Perpendicular switching of a single ferromagnetic layer induced by in-plane current injection," *Nature,* vol. 476, pp. 189-193, 2011.

[58] M. Althammer, "Pure spin currents in magnetically ordered insulator/normal metal heterostructures," *J. Phys. D,* vol. 51, p. 313001, 2018.

[59] B. F. Miao, S. Y. Huang, D. Qu and C. L. Chien, "Inverse Spin Hall Effect in a Ferromagnetic Metal," *Physical Review Letters,* vol. 111, 2013.

[60] J. Sinova, S. O. Valenzuela, J. Wunderlich, C. H. Bach and T. Jungwirth, "Spin Hall Effects," *Rev. Mod. Phys.,* vol. 87, pp. 1213-1259, 2015.

[61] T. Tanaka, H. Kontani, M. Naito, T. Naito, D. S. Hirashima, K. Yamada and J. Inoue, "Intrinsic spin Hall effect and orbital Hall effect in 4d and 5d transition metals," *Physical Review B,* vol. 77, 2008.

[62] M. I. Dyakonov and V. I. Perel, "Current-induced spin orientation of electrons in semiconductors," *Physics Letters A,* vol. 33, 1971.

[63] J. E. Hirsch, "Spin Hall effect," *Phys. Rev. Lett.,* vol. 83, p. 1834, 1999.

[64] A. Hoffmann, "Spin Hall Effects in Metals," *IEEE Transactions on Magnetics,* vol. 49, 2013.

[65] V. M. Edelstein, "Spin polarization of conduction electrons induced by electric current in two-dimensional asymmetric electron systems," *Solid State Commun.,* vol. 73, pp. 233-235, 1990.

[66] I. M. Miron, G. Gaudin, A. S, B. Rodmacq, A. Schuhl, S. Pizzini, J. Vogel and P. Gambardella, "Current-driven spin torque induced by the Rashba effect in a ferromagnetic metal layer," *Nat. Mat. Lett.,* vol. 9, 2010.

[67] K.-W. Kim, S.-M. Seo, J. Ryu, K.-J. Lee and H.-W. Lee, "Magnetization dynamics induced by in-plane currents in ultrathin magnetic nanostructures with Rashba spin-orbit coupling," *Phys. Rev. B,* vol. 85, p. 180404(R), 2012.

[68] G. Allen, S. Manipatruni, D. E. Nikonov, M. Doczy and I. A. Young, "Experimental demonstration of the coexistence of spin Hall and Rashba effects in β-tantalum/ferromagnet bilayers," *Phys. Rev. B,* vol. 91, p. 144412, 2011.

[69] X. Fan, H. Celik, J. Wu, C. Ni, K.-J. Lee, V. O. Lorenz and J. Q. Xia, "Quantifying interface and bulk contributions to spin–orbit torque in magnetic bilayers," *Nat. Commun.,* vol. 5, p. 3042, 2014.

[70] G. Seibold, S. Caprara, M. Grilli and R. Raimondi, "Theory of the spin galvanic effect at oxide interfaces," *Phys. Rev. Lett.,* vol. 119, p. 256801, 2017.

[71] H. Wang, C. Du, P. C. Hammel and F. Yang, "Spin current and inverse spin Hall effect in ferromagnetic metals probed by Y3Fe5O12-based spin pumping," *Applied Physics Letters,* vol. 104, 2014.

[72] A. Azevedo, O. A. Santos, R. O. Cunha, R. Rodríguez-Suárez and S. M. Rezende, "Addition and subtraction of spin pumping voltages in magnetic hybrid structures," *Applied Physics Letters,* vol. 104, 2014.

[73] A. Tsukahara, Y. Ando, Y. Kitamura, H. Emoto, E. Shikoh, M. P. Delmo, T. Shinjo and M. Shiraish, "Self-induced inverse spin Hall effect in permalloy at room temperature," *Physical Review B,* vol. 89, p. 235317, 2014.

[74] M. Weiler, J. M. Shaw, H. T. Nembach and T. J. Silva, "Detection of the DC Inverse Spin Hall Effect Due to Spin Pumpingin a Novel Meander-Stripline Geometry," *IEEE Magnetics Letters,* vol. 5, 2014.

[75] T. Taniguchi, J. Grollier and M. D. Stilles, "Spin-Transfer Torques Generated by the Anomalous Hall Effect," *Physical Review Applied,* vol. 3, 2015.

[76] O. Mosendz, V. Vlaminck, J. E. Pearson, F. Y. Fradin, G. E. W. Bauer, S. D. Bader and A. Hoffmann, "Detection and quantification of inverse spin Hall effect from spin pumping in permalloy/normal metal bilayers," *Physical Review B,* vol. 82, 2010.

[77] H. Wang, C. Du, Y. Pu, R. Adur, P. Hammel and F. Yang, "Scaling of Spin Hall Angle in 3d, 4d, and 5d Metals from Y3Fe5O12/Metal Spin Pumping," *Phys. Rev. Lett.,* vol. 112, p. 197201 , 2014.

[78] C. Du, H. Wang, P. C. Hammel and F. Yang, "Y3Fe5O12 spin pumping for quantitative understanding of pure spin transport and spin Hall effect in a broad range of materials," *Journal of Applied Physics,* vol. 117, 2015.

[79] T. Wimmer, B. Coester, S. Geprägs, R. Gross, S. T. B. Goennenwein, H. Huebl and M. Althammer, "Anomalous spin Hall angle of a metallic ferromagnet determined by a multiterminal spin injection/detection device," *Appl. Phys. Lett.,* vol. 115, p. 092404 , 2019.

[80] H. Wang, C. Du, P. C. Hammel and F. Yang, "Spin current and inverse spin Hall effect in ferromagnetic metals probed by Y3Fe5O12-based spin pumping," *Appl. Phys. Lett.,* vol. 104, p. 202405, 2014.

[81] F. Yang and P. C. Hammel, "FMR-driven spin pumping in Y3Fe5O12-based structures," *J. Phys. D,* vol. 51, p. 253001, 2018.

[82] B. Kardasz, O. M. B. Heinrich, Z. Liu and M. Freeman, "Spin current studies in Fe/Ag, Au/Fe by ferromagnetic resonance and time-resolved magneto-optics," *J. Appl. Phys.,* vol. 103, p. 07C509, 2008.

[83] S. Geller and M. A. Gilleo, "The crystal structure and ferrimagnetism of yttrium iron garnet," *J. Phys. Chem. Solids,* vol. 3, pp. 30-36, 1957.

[84] O. d'A. Kelly, A. Anane, R. Bernard, J. Ben-Youssef, C. Hahn, A. H. Molpeceres, C. Carrétéro, E. Jacquet, C. Deranlot, P. Bortolotti, R. Lebourgeois, J.-C. Mage, G. deLoubens, O. Klein, V. Cros and A. Fert, "Inverse spin Hall effect in nanometer-thick yttrium iron garnet/Pt system," *Appl. Phys. Lett.,* vol. 103, p. 082408, 2013.

[85] J. Ding, T. Liu, H. Chang and M. Wu, "Sputtering growth of low-damping yttrium-iron-garnet thin films," *IEEE Mag. Lett.,* vol. 11, p. 5502305, 2020.

[86] Y. Sun, Y.-Y. Song, H. Chang, M. Kabatek, M. Jantz, W. Schneider, M. Wu, H. Schultheiss and A. Hoffmann, "Growth and ferromagnetic resonance properties of nanometer-thick yttrium iron garnet films," *Appl. Phys. Lett.,* vol. 101, p. 152405, 2012.

[87] M. Wu, "Nonlinear Spin Waves in Magnetic Film Feedback Rings," in *Solid State Physics, vol. 62*, Elsevier, 2010, pp. 163-224.

[88] A. H. Morrison, "Morphology and physical properties of gamma iron oxide," in *Crystals for magnetic applications*, Berlin, Springer-Verlag, 1978.

[89] E. J. J. Mallmann, A. S. B. Sombra, J. C. Goes and P. B. A.Fechine, "Yttrium iron garnet: properties and applications review," *Solid State Phenomena,* vol. 202, pp. 65-96, 2013.

[90] A. Lehmann-Szweykowska, R. Wojciechowski, L. Pust, P. E. Wigen and S. Batra, "Magnetic superexchange in YIG and Ca2+:YIG," *J. Appl. Phys.,* vol. 69, p. 4648, 1991.

[91] P. B. A. Fechine, Estudo das propriedades estruturais e elétricas das granadas ferrimagnéticas GdIG(x)YIG(1-x) e suas aplicações em componentes de microondas (PhD Dissertation), Fortaleza: UFC, 2008.

[92] Y.-M. Kang, S.-H. Wee, S.-I. Baik, S.-G. Min, S. Yu, S.-H. Moon, Y.-W. Kim and S.-I. Yoo, "Magnetic properties of YIG thin films prepared by the post annealing of amorphous films deposited by rf-magnetron sputtering," *J. Appl. Phys.,* vol. 97, p. 10A319, 2005.

[93] J. Liana, Y. Chena, Z. Liua, M. Zhua, G. Wanga, W. Zhanga and X. Donga, "Annealing effects on the microstructure and magnetic properties of Y3Fe5O12 films deposited on Si/SiO2 substrates by RF magnetron sputtering," *Ceramics Intl.,* vol. 43, p. 7477–7481, 2017.

[94] H. Chang, P. Li, W. Zhang, T. Liu, A. Hoffmann, L. Deng and M. Wu, "Nanometer-Thick Yttrium Iron Garnet Films With Extremely Low Damping," *IEEE Mag. Lett.,* vol. 5, p. 6700104, 2014.

[95] G. Woltersdorf, Spin-pumping and two-magnon scattering in magnetic multilayers (PhD Dissertation), Vancouver: Simon Fraser University, 2004.

[96] B. Heinrich, C. Burrowes, E. Montoya, B. Kardasz, E. Girt, Y.-Y. Song, Y. Sun and M. Wu, "Spin pumping at the magnetic insulator (YIG)/normal metal (Au) interfaces," *Phys. Rev. Lett.,* vol. 107, p. 066604, 2011.

[97] I. Neudecker, Magnetization Dynamics of Confined Ferromagnetic Systems (PhD Dissertation), Regensburg: Universität Regensburg, 2006.

[98] A. M. Gonçalves, Dinâmica da magnetização em sistemas spintrônicos (PhD Dissertation), Rio de Janeiro: CBPF, 2015.

[99] G. L. d. S. Vilela, Geração e detecção de correntes puras de spin pelos efeitos de spin pumping e Seebeck de spin (PhD Dissertation), Recife: Universidade Federal de Pernambuco, 2013.

[100] B. Heinrich, "Ferromagnetic Resonance in Ultrathin Film Structures," in *Ultrathin Magnetic Structures II*, Springer-Verlag, 2005.

[101] I. Neudecker, G. Woltersdorf, B. Heinrich, T. Okuno, G. Gubbiotti and C. H. Back, "Comparison of frequency, field, and time domain ferromagnetic resonance methods," *Journal of Magnetism and Magnetic Materials,* vol. 307, pp. 148-156, 2006.

[102] H. K. Lee, Nonlinear Magnetic Damping and Parametric Excitation of Magnetization in Nanomagnets (PhD Dissertation), Irvine: University of California, 2017.

[103] M. V. Zaezjev, M. C. Sekhar, M. Ferrera, L. Razzari, B. M. Holmes, M. Sorel, D. C. Hutchings, A. Pignolet and R. Morandotti, "Crystallization of yttrium-iron garnet (YIG) in thin films: Nucleation and growth aspects," *Mater. Res. Soc. Symp. Proc.,* vol. 1036, 2008.

[104] J. Lian, Y. Chen, Z. Liu, M. Zhu, G. Wang, W. Zhanga and X. Dong, "Annealing effects on the microstructure and magnetic properties of Y3Fe5O12 films deposited on Si/SiO2 substrates by RF magnetron sputtering," *Ceramics International,* vol. 43, p. 7477–7481, 2017.

[105] S.-Y. Sung, X. Qi and B. J. H. Stadler, "Integrating yttrium iron garnet onto nongarnet substrates with faster deposition rates and high reliability," *Appl. Phys. Lett.,* vol. 87, 2005.

[106] B. M. Howe, S. Emori, H.-M. Jeon, T. M. Oxholm, J. G. Jones, K. Mahalingam, Y. Zhuang, N. X. Sun and G. J. Brown, "Pseudomorphic yttrium iron garnet thin films with low damping and inhomogeneous linewidth broadening," *IEEE Mag. Lett.,* vol. 6, p. 3500504, 2015.

[107] P. C. Van, S. Surabhi, V. Dongquoc, R. Kuchi, S.-G. Yoon and J.-R. Jeong, "Effect of annealing temperature on surface morphology and ultralow ferromagnetic resonance linewidth of yttrium iron garnet thin film grown by rf sputtering," *Appl. Surf. Sci.,* vol. 435, pp. 377-383, 2018.

[108] R. T. Victor, Estudo da dinâmica de magnetização em sistemas FM/NM para aplicações em spintrônica (MsC Thesis), Rio de Janeiro: CBPF, 2019.

[109] J. F. K. Cooper, C. J. Kinane, S. Langridge, M. Ali, B. J. Hickey, T. Niizeki, K. Uchida, E. Saitoh, H. Ambaye and A. Glavic, "Unexpected structural and magnetic depth dependence of YIG thin films," *Phys. Rev. B,* vol. 96, p. 104404, 2017.

[110] L. Jin, K. Jia, Y. He, G. Wang, Z. Zhong and H. Zhang, "Pulsed laser deposition grown yttrium-iron-garnet thin films: Effect of composition and iron ion valences on microstructure and magnetic properties," *Appl. Surf. Sci.,* vol. 483, pp. 947-952, 2019.

[111] H. Chang, T. Liu, D. R. Hickey, P. A. P. Janantha, K. A. Mkhoyan and M. Wu, "Sputtering growth of Y3Fe5O12/Pt bilayers and spin transfer at Y3Fe5O12/Pt interfaces," *Apl. Materials,* vol. 5, p. 126104, 2017.

[112] M. Li, H. Zhang, Y. H. Rao, C. Hong, Z. Zhong, Q. Yang, X. Tang and L. Jin, "Giant damping enhancement induced by exchange coupling in Y3Fe5O12/Co2FeAl0.5Si0.5 bilayers," *J. All. Com.,* vol. 767, pp. 398-402, 2018.

[113] S. Azzawi, A. T. Hindmarch and D. Atkinson, "Magnetic damping phenomena in ferromagnetic thin-films and multilayers," *J. Phys. D,* vol. 50, p. 473001, 2017.

[114] R. C. Fletcher, R. C. LeCraw and E. G. Spencer, "Electron spin relaxation in ferromagnetic insulators," *Phys. Rev.,* vol. 117, pp. 995-963, 1960.

[115] B. Heinrich, Y. Tserkovnyak, G. Woltersdorf, A. Brataas, R. Urban and G. E. W. Bauer, "Dynamic Exchange Coupling in Magnetic Bilayers," *Phys. Rev. Lett.,* vol. 90, p. 187601, 2003.

[116] T. Taniguchi, "Spin-current driven spontaneous coupling of ferromagnets," *Phys. Rev. B,* vol. 98, p. 104417, 2018.

[117] F. B. Mancoff, N. D. Rizzo, B. N. Engel and S. Tehrani, "Phase-locking in double-point-contact spin-transfer devices," *Nat. Lett.,* vol. 437, p. 04036, 2005.

[118] S. Kaka, M. R. Pufall, W. H. Rippard, T. J. Silva, S. E. Russek and J. A. Katine, "Mutual phase-locking of microwave spin torque nano-oscillators," *Nat. Lett.,* vol. 437, p. 04035, 2005.

[119] W. H. Rippard, M. R. Pufall, S. Kaka, T. J. Silva and S. E. Russek, "Injection locking and phase control of spin transfer nano-oscillators," *Phys. Rev. Lett.,* vol. 95, p. 067203, 2005.

[120] A. Brataas, Y. Tserkovnyak, G. E. W. Bauer and P. J. Kelly, "Spin pumping and spin transfer," in *Spin Current*, Oxford, Oxford University Press, 2012, pp. 87-135.

[121] T. Taniguchi, "Dynamic coupling of ferromagnets via spin Hall magnetoresistance," *Phys. Rev. B,* vol. 95, p. 104426, 2017.

[122] N. Behera, S. Chaudhary and D. K. Pandya, "Anomalous anti-damping in sputtered β-Ta/Py bilayer system," *Sci. Rep.,* vol. 6, p. 19488, 2016.